ANALYTICAL STUDY OF POROSITY, DISPERSION ENERGY AND DIELECTRIC ENERGY LOSSES ON PERFORMANCE OF ANNEALED TiO_2 – GRAPHENE DYE SENSITIZED SOLAR CELL

NELSON MUGAMBI

DOCTOR OF PHILOSOPHY

(Physics)

JOMO KENYATTA UNIVERSITY

OF

AGRICULTURE AND TECHNOLOGY

2025

Analytical Study of Porosity, Dispersion Energy and Dielectric Energy Losses on Performance of Annealed TiO_2 - Graphene Dye Sensitized Solar Cell

Nelson Mugambi

A Thesis Submitted in Partial Fulfillment of the Requirements for the Degree of Doctor of Philosophy in Physics of the Jomo Kenyatta University of Agriculture and Technology

2025

DECLARATION

This thesis is my original work and has not been presented for a degree in any other University

Signature: …… Date: ……

Nelson Mugambi

This thesis has been submitted for examination with our approval as the University Supervisors

Signature: …… Date: ……

Prof. James M. Ngaruiya, PhD
JKUAT, Kenya

Signature: …….. Date: ……

Dr. Simon W. Mugo, PhD
JKUAT, Kenya

DEDICATION

Dedicated to my parents for their unmatched love, my cherished sisters Doreen, Queensbeth and Josyline, my gorgeous wife Peninnah, my lovely son Ryan, and my adorable daughter Merlyne.

ACKNOWLEDGMENT

First, I want to express my gratitude to the Almighty for his direction, favor, and providence throughout this study. I'd also like to thank Dr. J. M. Ngaruiya and Dr. S. W. Mugo, both of whom I consider myself fortunate to have known, worked with, and had as advisors. They taught me to believe in myself, to be aware of my strengths while working hard to improve my weaknesses, to be an independent researcher, and, most importantly, to be driven by their own daily example of incredible hard work. This work would not have been feasible without the facilities provided by the Jomo Kenyatta University of Agriculture and Technology (JKUAT), the Physics Departments Kenyatta University (KU), Chuka University, University of Nairobi (UON), and Charm Graphene, Gwonseon-gu, Suwon, Republic of Korea. I would also like to thank the entire JKUAT Physics technical team for their devotion and assistance in making this effort a success. Working in the JKUAT Physics, Chemistry, Engineering, and Food Science labs was one of the best learning experiences of my life. I would want to thank Mr. Fred, chief technician of the physics department at Kenyatta University, Mr. Mutunga at Chuka University, Mr. David food science JKUAT and Mr. Boniface Muthoka of UON for their invaluable time and assistance throughout my project at JKUAT. Many of the tests and hypotheses presented in this book would not have been conceivable without the assistance of my close friends and collaborators Dr. Paul Ngumbi, Dr. Mbaluka B. John, Mr. John G. Mbae, Mr. Geoffrey G. Riungu, and Miss Kipkorir J. Sheilla. My parents, Lewis and Cathrene, are still my primary social, emotional, and psychological supports. I'd also like to thank my lovely sisters Doreen, Queensbeth, and Josyline, my adored children Ryan and Merlyne, and my loving wife Penninah. They gave me a place to vent. They were available when I needed to think about something other than TiO_2.

TABLE OF CONTENTS

LIST OF TABLES

LIST OF FIGURES

LIST OF APPENDICES

ABBREVIATIONS AND ACRONYMS

Al_2O_3	Aluminum Oxide
AM	Air Mass
CB	Conduction Band
CdTe	Cadmium telluride
CE	Counter Electrode
CIGS	Copper Indium gallium Selenide
CN	Coordination number
CO_2	Carbon dioxide
CPD	Contact Potential Difference
CPV	Concentrator Photovoltaic
c-Si	Crystalline Silicon
D	Electron diffusion coefficient
DNI	Direct normal irradiance
DSSCs	Dye-sensitized Solar Cells
E_g	Band gap
EM	Electromagnetic
eV	Electron volt
FF	Fill Factor
FTIR	Fourier Transform Infra-Red
FTO	Fluorine-doped Tin Oxide

GO	Graphene Oxide
GTiO$_2$Ns	Graphene Titanium dioxide nanoparticles
GW	Giga watts
HOMO	Highest Occupied Molecular Orbitals
In$_2$O$_3$	Indium (III) oxide
I$_{SC}$	Short Circuit Current
ITO	Indium Tin Oxide
J$_{SC}$	Short-Circuit Current Density
J-V	Current density – Voltage
LUMO	Lowest Unoccupied Molecular Orbitals
MgO	Magnesium oxide
Mvp	Maximum voltage power
Nb$_2$O$_5$	Niobium pentoxide
NiO	Nickel oxide
^{O}C/min	Degrees Celsius per minute
OPV	Organic photovoltaic
PCE	Power Conversion Efficiency
PV	Photovoltaic
R. D	Relative density
SC	Semiconductor
SELF	Surface energy loss function

SKPM	Scanning Kelvin Probe Microscope
TCOs	Transparent Conducting Oxides
TiO_2	Titanium dioxide
UV VIS NIR	Ultra Violet, Visible, Near-Infrared
VB	Valence Band
VELF	Volume energy loss function
V_{OC}	Open circuit voltage
WDD	Wemple DiDomenico
WE	Working electrode
ZnO	Zinc Oxide

LIST OF SYMBOLS

$\mathbf{A_b}$	Absorbance
C	Speed of electromagnetic radiation
e	Electron charge
$\mathbf{E_d}$	Dispersion Energy
$\mathbf{E_F}$	Fermi energy
$\mathbf{E_H}$	Hall electric field
$\mathbf{F_B}$	Magnetic force
$\mathbf{F_E}$	Electric force
$\boldsymbol{h}$	Plank's constant
hkl	Miller indices
$\mathbf{J_{cv1}}$	Real part interband transition
$\mathbf{J_{cv2}}$	Imaginary part interband transition
$\mathbf{J_{dark}}$	Dark current density
$\boldsymbol{K_B}$	Boltzmann constant
$\mathbf{K_{ex}}$	Extinction coefficient
N	Refractive index
$\mathbf{n_o}$	Refractive index of pore free anatase TiO_2 film
$\mathbf{n_s}$	Charge concentration
P	Porosity
ϕ	Work function
$\mathbf{P_{in}}$	Power input

$\mathbf{P_{out}}$	Power output
$\mathbf{R_f}$	Reflectance
$\mathbf{T_{emp}}$	Temperature
$\mathbf{T_r}$	Transmittance
S	Absorbed dye
S*	Excited state dye
$\mathbf{V_H}$	Hall voltage
A	Light absorption coefficient
$\boldsymbol{\alpha_p}$	Electronic polarizability
B	Band tailing parameter
$\boldsymbol{\Delta}$	Power Loss
$\boldsymbol{\varepsilon}$	Complex dielectric constant
$\boldsymbol{\varepsilon_1}$	Real part dielectric constant
$\boldsymbol{\varepsilon_2}$	Imaginary part dielectric constant
$\boldsymbol{\eta}$	Power conversion efficiency
$\boldsymbol{\lambda}$	Wavelength
$\boldsymbol{\lambda_o}$	Average oscillator wavelength
$\boldsymbol{\mu_s}$	Charge mobility
$\boldsymbol{\nu}$	Frequency
$\boldsymbol{\sigma}$	Conductivity
$\boldsymbol{\sigma_e}$	Electrical conductivity

σ_{opt}	Optical conductivity
T	Relaxation time
χ^{1}	Linear optical susceptibility
χ^{3}	Nonlinear optical susceptibility

ABSTRACT

Recent advances in technology have sparked interest in improving the efficiency of dye-sensitive solar cells (DSSC) with great progress, to mitigate challenges such as high recombination rates and low quantum yield. The present study demonstrates a facile synthesis of modified Titanium dioxide (TiO_2) compact layers on fluorine tin oxide (FTO) and graphene using the Sol gel Doctor Blade deposition method for solar applications. As deposited films and films subjected to one-step annealing, annealing rates of 1 °C/min and 2 °C/min were studied utilizing a range of techniques, including a Varian 7000e FTIR, UV-VIS spectrophotometer, a Scanning Kelvin Probe Microscope (SKPM), and a Hall Effect setup. FTIR demonstrated considerable absorption at low frequencies (less than 798 cm^{-1}) in TiO_2 on graphene heterojunctions, confirming the production of Ti-O and C-O-Ti bonds. The major anatase TiO_2 characteristic was detected at 438 cm^{-1}. All films had reflectance between 25 - 30 % in the visible spectrum (550 nm), in accordance to the TiO_2 on FTO examination, and average refractive indices ranged from 1.95 to 1.56. The lowest porosity (53%) and maximum dispersion energy (11.30 eV) were found in the film annealed at 1 °C/min. The surface-to-volume energy loss ratio was least for 1°C annealing rate. TiO_2 on graphene annealed at a rate of 1 °C/min exhibited a lower VELF/SELF than TiO_2 on FTO, implying that an electron dissipates less energy when passing through the TiO_2 on graphene film than it does in TiO_2 on FTO. The light absorption coefficient (α) and electron diffusion coefficient (D) of TiO_2 on graphene rose to 4.637×10^3 and 1.485×10^{-4} (1 °C/min), respectively, whereas TiO_2 on FTO values increased to 4.221×10^3 and 1.251×10^{-4} (1 °C/min), in that order. Higher α and D values of TiO_2 on graphene indicate enhanced electron transition in the films. Hall Effect measurements on as-deposited and annealed TiO_2 on graphene films demonstrated enhanced conductivity at 1 °C/min annealing rate, which was attributed to recrystallization of films due to calcination. Work functions (φ) measurements were -730.8 mV, - 436.3 mV, and -189.2 mV, which reveal an increasing trend towards 1 °C/min annealing rate. This spatial variation and distribution are explained by ensemble modifications to granular tilts and surface slopes using a Smoluchowski smoothing model. The spatially varying levels of electric dipole moments, which are essential to atomic steps, alter φ and induce local fluctuations. The incorporation of TiO_2 on graphene photoanode improved h^+/e^- separation, electron transport, and light absorption due to the high specific surface area of the porous structure and the continuous conduction network on compact TiO_2 nanoparticles on graphene acting as an electron leakage barrier. C1 (FTO/TiO_2-Pt/FTO), C2 (Gr/TiO_2-Pt/FTO), C3 (FTO/TiO_2-Pt/Gr), and C4 (Gr/TiO_2-Pt/Gr) DSSCs were fabricated (at 1 °C/min) and labeled. I_{sc} and V_{oc} average values were found to be 8.1925 mA and 0.6375 V, respectively. C4 had the highest *PCE* (%) = 2.973 (3.4 % enhancement on C1). Lower efficiencies noted on C1, C2 and C3 DSSCs could be due to the relatively poor adhesion of TiO_2 on FTO resulting to faster back reaction and electron recombination over transport. Tuning annealing rates and coupling TiO_2 to graphene improves both dye active sites and crystallinity. Flexible TiO_2-graphene nanosheets lower internal resistance and prevent carrier recombination rates. TiO_2 on graphene electrode matrix promote C4's power conversion efficiency (PCE) by boosting dye adsorption, electron ejection improving transport.

CHAPTER ONE

INTRODUCTION

1.1 Background

Research into alternative, renewable, and clean energy generation is driven by concerns about global warming caused by fossil fuel combustion and the increasing global energy demand. The US Energy Information Administration (2011) reports that global energy consumption is expected to double by 2035, and fossil fuels will soon be unable to meet this demand. Renewable and sustainable sources of energy, such as solar energy, geothermal energy, hydroelectricity, and biofuels, have gained attention. Solar energy is particularly promising due to its numerous benefits and potential for power generation for millions of years. An estimated solar flux of 3.8×10^{24} Joules (Hasan & Sumathy, 2010) suggests that solar energy has the potential to fulfill all global energy requirements, entirely replacing fossil fuels.

Photovoltaic devices, which have undergone three generations of development, are essential to the conversion of solar energy into electrical power: first-generation using crystalline silicon (Zhang & Cao, 2011), second-generation using thin-film cells (Chopra *et al*., 2004), and third-generation using dye-sensitized solar cells (DSSCs) and organic photovoltaics (OPV) (Wohrle & Meissner, 1991). The discovery of nanocrystalline TiO_2-based mesoporous film sensitized by N719 dye, which provides a significant PCE of 7-8%, has sparked commercial excitement for DSSCs (O'regan & Grätzel, 1991).

The structural features of mesoporous TiO_2 films, such as particle size and porosity, have signifying influence on DSSC performance (Yasuteru *et al*., 2004). TiO_2 sheets with high porosity enhance increased light absorption and current density. Effectiveness of TiO_2 dispersion (Folli *et al*., 2010), and its pore structure are important factors for accessing active surface area advantageous for enhancing photocatalytic performance (Ramirez *et al*., 2010). Enhancing TiO_2 films' surface area and porosity in dye-sensitized solar cells (DSSCs) promotes performance by providing more dye-attaching sites and facilitating faster electron movement, improving

efficiency (Choudhury *et al.,* 2021). TiO_2 photocatalysts have a wide band gap, limiting their use to UV light. However, mesoporous TiO_2 is a popular choice for DSSCs due to its high oxidizing electron-hole pair generation capacity, chemical stability, low cost, non-toxicity, and long-term photo stability. Nevertheless, the application of TiO_2 photocatalysis is still in the laboratory stage due to its limitations, such as low quantum yield and poor light harvesting capabilities due to quick electron-hole pair recombination, limited adsorption ability to hydrophobic pollutants, high aggregation propensity, and difficulty in separating TiO_2 after treatment. It is expensive and complex to dope TiO_2 with plasmonic metals and other semiconductors (Cui *et al*., 2008), metals, and non-metals (Dozzi & Selli, 2013) to boost its photocatalytic activity.

Due to its peculiar structural and electrical properties, carbonaceous nanomaterials including fullerenes, carbon nanotubes, and graphene have recently attracted more interest when coupled with a TiO_2 photocatalyst (Leary & Westwood 2011; Geim & Novoselov 2007). Thermal exfoliation, CVD or epitaxial growth reduces graphene oxide to graphene. Graphene offers a two-dimensional sp^2 carbon network. In addition to its rich surface properties, it has strong charge carrier mobility (200000 $cm^2V^{-1}s^{-1}$), offers a sizable specific surface area, and exhibits outstanding thermal and electrical conductivity (Xiang *et al*., 2012). This inhibits the recombination of excited charge carriers.

To achieve reliable PCE using TiO_2 as a working electrode, it is necessary to thoroughly understand interfacial charge relationship in TiO_2 films by evaluating and optimizing its porosity, bandgap, dispersion energy, work function, and energy losses, as the interrelationship between these properties is not well documented. According to Ngei (2016), Cui *et al.,* (2021), and Muthee & Dejene (2021), annealing TiO_2 is a simple, less costly, and less complex method of altering its properties.

This research aims to investigate effects of porosity, dispersion energy, dielectric energy losses and their correlation to electron transport in TiO_2 for improved DSSC photoanodes using graphene materials.

1.2 Statement of the Problem

Green energy sources are becoming necessary due to the expanding worldwide environmental and energy challenges. Solar energy is emerging in this context as a viable renewable, affordable, and clean energy source. The performance of the DSSC has improved thanks to the use of a support matrix made of nanocrystalline semiconductor, which considerably boost the photoanode films' specific surface area for greater dye adsorption for light harvesting efficiency enhancement. TiO_2 has received a lot of attention as a semiconductor in solar energy conversion applications. This is due to the simple morphological and structural control, strong chemical and thermal stability, and favorable band gap position for photocatalysis. The electron diffusion coefficient of the nanocrystalline TiO_2 film is significantly lower than that of the bulk material due to the grain boundaries. Electron transport is a limiting step in charge transfer processes in DSSCs (He *et al*., 2011), occurring slowly enhance recombination of injected electrons due to the long transit time and closeness of electrons to oxidized redox species. Contacting TiO_2 on graphene and annealing at varied rates are at the cutting edge of research to overcome this drawback. Although work involving TiO_2 modification by tuning its porosity, dispersion energy, bandgap, work function, and energy losses to improve PCE of a DSSC due to enhanced charge mobility and inhibiting charge trapping and recombination has been widely studied, little is reported about the interdependence of these properties for photovoltaic applications. This study is intended to synthesize a TiO_2 as an interface for graphene, optimize its properties, and assess its contribution to increased photoanode crystallinity, resulting in composite nanostructures with improved solar energy harvesting properties. Changes to its structure and design may result in enhanced electron transport, boosting the overall efficiency of DSSC.

1.3 Justification of the Study

DSSCs' efficiency is influenced by charge injection and transportation mechanisms. Despite being affordable and easily scaled up, DSSCs face low efficiency challenges (O'regan & Grätzel, 1991). Research on TiO_2 on graphene aims to create composite nanostructures with improved solar energy harvesting properties, potentially leading to increased efficiencies through structural and design modifications.

Graphene's excellent conductivity within the photo anode increases catalytic activity of the cell, enhancing charge transport and reducing electron-hole recombination within the DSSC. In order to modify surface morphology, optical bandgap, surface potential, dispersion energy, and energy losses, researchers have employed deposition processes, annealing, changing chemical concentrations, and solvent PH. In this work, TiO_2 films on graphene and FTO were synthesized using the Doctor Blade process and annealed at various annealing rates. These films' porosity, dispersion energy, dielectric energy losses, and sheet conductivity investigated, correlated and optimized. The optimized films were subsequently used to fabricate and examine DSSCs performance.

1.4 Objectives

1.4.1 General Objective

To characterize TiO_2 on FTO and TiO_2 on Graphene composite electrodes by optimizing Porosity, Dispersion energy and energy losses for dye sensitized solar cells application.

1.4.2 Specific Objectives

1. To determine the optical reflectance, refractive indices and porosity of annealed TiO_2 on FTO films deposited by Doctor Blade technique using UV-VIS-NIR spectroscopy.
2. To evaluate the dielectric energy losses and dispersion responses using refractive indices of annealed TiO_2 on FTO films.
3. To investigate the effect of graphene on porosity, dispersion energy and dielectric energy losses on annealed TiO_2 on graphene films and use FTIR to confirm functional groups.
4. To evaluate the contact potential difference using SKPM and electrical sheet conductivity of annealed TiO_2 on epitaxial graphene using Hall Effect.
5. To analyze the effect of porosity, dispersion energy and dielectric energy loss on TiO_2/FTO and TiO_2/graphene DSSC.

CHAPTER TWO

LITERATURE REVIEW

2.1 Solar Energy Overview

Solar energy, despite its rapid adoption and support from the scientific establishment and energy capitalists, is a small part of total energy usage. Despite its potential, the high cost of extraction, processing, and storage hinders its widespread use. Solar radiation can be converted into electrical or thermal energy, with the former being easier. Solar energy is the cleanest and most prolific renewable source available, and can be used to generate electricity (highlighted in the following section), provide light, and heat water for domestic, commercial, or industrial use.

2.2 Principles of Solar Cell

Semiconductor materials, particularly silicon, have been the focus of much research during the last century due to their usage in the electronic industry. Because of its conductivity, which is sensitive to temperature and trace quantities of impurity atoms, silicon is utilized in making photovoltaics (*PV*) cell. Solar cells capture solar energy and convert it into electrical power for everyday use. Solar light is at a higher level before entering the atmosphere, with heat affecting the solar surface in the UV light range (175 nm to 400 nm), visible spectrum (400 nm to 700 nm), and near-infrared (700 nm to 3000 nm) spectrum. Most solar cells are tuned for the visible spectrum, which has the highest solar intensity. The extraterrestrial spectrum reference is *AM* 0, while *AM* 1.5 is defined by the atmospheric state of the sun zenith angle 48.19 ^{o}S, water vapor, and ozone. The photovoltaic effect is the process by which electrons are converted into electricity by absorbing photons. This process involves three key steps: photon absorption in a p-n junction semiconductor, producing electron-hole pairs, and the separation of light-generated charge carriers (Sharma *et al.*, 2021). This concept is the foundation for harnessing solar energy and converting it to electricity, powering all solar cells. When a photon with energy higher than the doped semiconductor material's gap energy is absorbed, the electron is excited from the valence band to the conduction band. The surplus photon energy provides additional kinetic energy to the

electron or hole. The semiconductor's minimal energy or work function is denoted by the symbol "$h\upsilon_0$", and heat is released from the surplus energy. In an external solar circuit, electrons can flow out over the n-region and through the circuit, while holes can flow away from the junction through the p-region before recombining with the electrons. Separated electrons power the electric circuit.

2.3 Advances in Dye Sensitized Solar Cell Technology

To preserve global environment and achieve long-term economic prosperity, alternatives to fossil fuel-based power generation systems must be developed. Photovoltaic systems, which convert solar energy into electricity, are a potential solution (Snaith & Schmidt-Mende, 2007). However, Silicon based manufacturing process prevent their widespread use due to high material costs. Due to its low cost, high efficiency, and simple manufacturing process, dye-sensitized solar cells (DSSC) are rapidly gaining popularity as an alternate option for silicon-based photovoltaics (Goncalves *et al.,* 2008).

2.3.1 Photo Electrode Fabrication of Dye-Sensitized Nano Solar Cells

The photo electrode is a key component of a DSSC that transmits light and then transports injected electron to an external circuit. As a result, photo electrodes should have excellent optical transparency as well as strong electrical conductivity (Gratzel, 2005). To increase the effectiveness of DSSCs, researchers must consider the materials employed as well as the film deposition procedures. In chemical deposition methods, a fluid precursor is often used to create a solid layer by undergoing a chemical change at the solid's surface (Choy, 2003). Spray pyrolysis, Chemical Vapor Deposition (CVD), successive ionic layer adsorption and reaction (SILAR), Sol-gel, and hydrolysis-limited sol-gel coatings are some of the methods that have been developed for the production of DSSCs. Each method has its advantages and limitations, but they all contribute to the development of efficient and cost-effective solar cells. Physical deposition methods involve mechanical or thermodynamic processes to prepare and deposit materials. Some techniques include spin coating, sputtering, DC magnetron sputtering and Doctor Blade technique.

The Doctor Blade technique, also known as tape casting or knife coating involves applying a paste to a substrate using a slanted blade in order to produce a film. The three steps of the doctor blade approach are pasting deposition on glass substrate, paste spreading, and drying film. Spacers guide a glass rod as it is rolled over a predetermined amount of paste on a substrate to determine the film's thickness (Padinger *et al*., 2000). The Doctor Blade method is a relatively low-cost method for applying metal oxide paste coatings (Ahmadi *et al*., 2014). According to Padinger *et al*., (2000), there are a number of disadvantages to the technique, including spread paste waste and a lengthy learning curve for the optimal coating parameters. The ability of concurrently depositing nanoparticles in the required layers, resulting to the production of composite films, is one element of Doctor Blade investigated in the present study.

2.3.2 Major Factors Affecting Solar Cell Performance

The efficiency and mineralization kinetics of solar cell systems are greatly altered by various operating factors such as photocatalytic pH, counter electrode types, electrolytes, dyes, and photoelectrode, which are crucial for optimal system optimization.

2.3.2.1 Photocatalytic pH and Dosage

Photocatalytic efficiency is influenced by pH, which affects nanoparticle size, surface charge, and ionization of pollutants. The point of zero charge (*PZC*) ranges from 4.5 to 7.0. Lower pH levels increase nanoparticles' (becomes positively charged) electrostatic pull, while higher pH levels draw cationic molecules from water. The size of nanoparticles is also affected by pH. The ideal TiO2 dosage depends on factors like photon fluxes, UV intensity, and photo reactor size (Chong *et al*., 2010).

2.3.2.2 Chemical Structure of Dye

Photosensitizers absorb photons and transfer electrons to TiO_2 materials, performing charge transfer and returning electrons to iodide. The dye industry offers various dyes, with Ruthenium polypyridyl dyes being the most efficient for photosensitization of

TiO_2-based DSSCs due to their wide absorption spectra, good photo-electrochemical characteristics, and high oxidation stability. The most widely used ruthenium complex dyes in DSSCs are N719 or Ruthenium 535-bisTBA. The conversion efficiency of ruthenium dye-based DSSCs is higher than cells sensitized with other dye compounds like chlorophyll derivatives (Boschloo & Hagfeldt, 2009). Ruthenium metal dyes have a low molar absorption coefficient in short wavelength ranges, so attempts have been made to synthesize dyes with high molar absorption coefficients to boost DSSC efficiency (Qin & Peng, 2011).

2.3.2.3 Liquid Electrolyte Selection

The DSSC process uses iodide $(I^-)/(I^{3-})$ triiodide, a redox ion, to facilitate electron transfer. Chloroplatinic acid is used as a catalyst to restore electrons to the iodide. However, temperature changes can damage electrolytes, cause freezes and stopping electricity production. The hazardous solvents used in the process also pose a risk to humans. Researchers are working on a solid-state version of this method, allowing electrolytes to be replaced with other materials to address these drawbacks (Nuraje *et al.*, 2012).

2.3.2.4 Types of Auxiliary Electrode

The auxiliary electrode, also known as the counter electrode, is a crucial component in a three-electrode electrochemical cell for voltammetric measurement or other procedures involving electric current flow. The counter electrode (*CE*) is formed by depositing a catalyst on a transparent conductive oxide (TCO), which allows excited dye reduction. Platinum (*Pt*) is the preferred catalyst due to its high catalysis, exchange current density, and transparency (Boschloo & Hagfeldt, 2009). The *CE* performance is determined by the deposition technique used, which affects the stability and charge-transfer resistances of the counter electrode. However, Pt electrocatalytic properties can decrease over time when the iodide/triiodide red-ox pair is present. Platinum is expensive but has excellent catalytic activity, but high temperatures are required for annealing the film. Graphene, carbon, and conductive polymers have been developed as substitutes for platinum due to their reactivity and high electrical conductivity (Li

et al., 2012). However, DSSCs based on these materials have been low due to poorer catalytic activity for triiodide reduction compared to Platinum.

2.3.2.5 Critical Design of TiO_2 and Other Metal Oxides Based Photoanodes

Higher electronic mobility is exhibited by zinc oxide (ZnO), which is favorable for electron transport. ZnO nanocrystalline films created by the sol-gel method and subsequently sensitized with *N3* dye, which produced promising findings. Nobium (V) oxide (Nb_2O_5) with a band gap of 3.49 eV delivered the second highest IPCE of ≈ 18 % after TiO_2 whose IPCE was found to be ≈ 45 % (Saito & Fujihara, 2008). MgO – coated SnO_2 DSSC achieved a maximum *PCE* of 7 % (Kuang *et al.*, 2006). O'Regan & Gratzel in 1991 developed the first dye-sensitized solar cell using porous titanium dioxide (TiO_2) electrodes. Nevertheless, TiO_2 deployment in DSSCs is inhibited by recombination of photogenerated electrons with the red-ox pair in the electrolyte. The goal of the current work is to overcome the limitations by developing TiO_2 on FTO and on graphene.

2.3.3 Electron Transport and Recombination Mechanism in a DSSC

The fundamental concept underlying the notion of dye-sensitized solar cells is an understanding of electron motion. Solar cells collect photons from sunshine, which excites the dye and causes electrons to shift from the valence band to the conduction band. An explanation of the DSSCs' operation on figure 2.1a, illustrates the energy level diagram of a TiO_2-based DSSC with an iodide/triiodide pair as the redox system and N719 dye as the sensitizer. Dye molecules absorb photons and move electrons from the HOMO to the LUMO state when exposed to light. These electrons are introduced into the conduction band of TiO_2, moved to a TCO film, and then transmitted to an external circuit for generating electricity. Figure 2.1b shows a schematic illustration of the operation principle and electron transfer process in DSSCs.

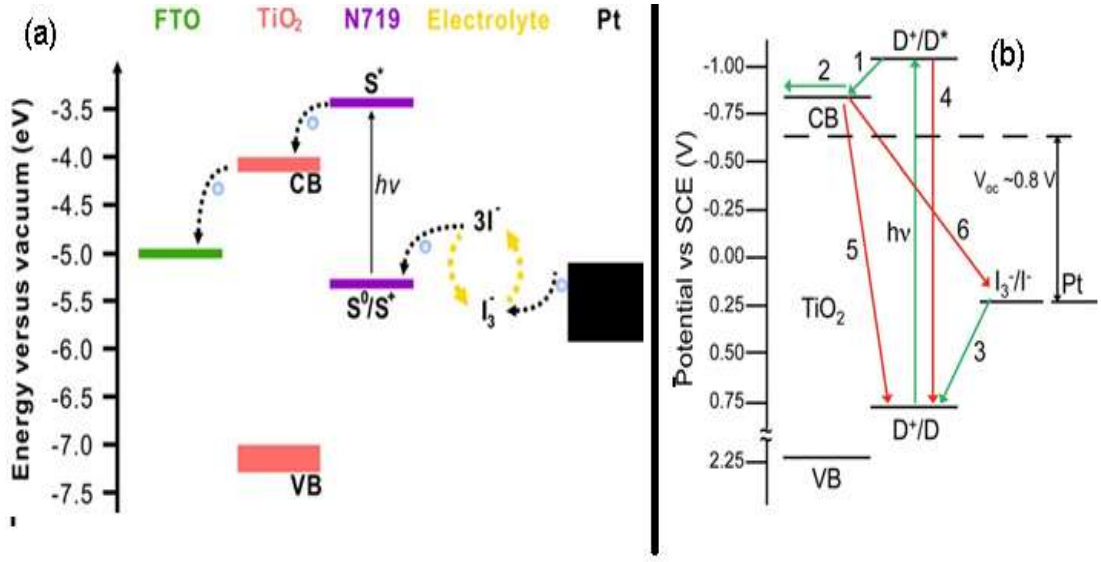

Figure 2.1: (a) Schematic Illustration of DSSC Structure with Respect to Energy of Respective Components. (b) Various Pathways for Charge Transfer and Recombination Processes in a DSSC (Baxter, 2012)

When light is shone on adsorbed dye (*S*), the dye is transformed into excited state dye (S*) by absorbing light. The Ru-complex photo synthesizer (*S*) stimulates the dye's electrons from their ground state (S/S+) to a higher energy state (S*/S+) when it absorbs a photon with enough energy (hv). **STEP 1,** illustrated as **(hυ)** in figure 2.1 (b) represents photoexcitation:

$$S + h\upsilon \rightarrow S^* \quad \text{..... (2.1)}$$

When the dye molecule is activated, it has two options. Either, to decay back to the ground state **(4)** or undergoing oxidative quenching. The latter introduces electrons into the TiO_2 films' conduction band **(1)**. This injection mechanism represented by equation (2.2), results in oxidation of the photo synthesizer (S+) (Katoh, 2012) **STEP 2**:

$$S^* \rightarrow S + h\upsilon' \quad \text{..... (2.2)}$$

An effective dye must have a LUMO level greater than the TiO_2 *CB* to allow electron injection into the TiO_2 *CB* and subsequent transfer into the external circuit via the TiO_2 **(2)** (Thavasi *et al.,* 2009) **STEP 3** presented in equation 2.3. Alternatively, those

electrons would recombine with the holes in the dye's HOMO (Hagfeldt *et al*., 2010). Due to the rapid injection operations of Ru-complexes, the device's performance time scales compare well to the decay behavior of the excited dye state returning to the ground state (Shalini *et al*., 2016; Thavasi *et al*., 2009). The excited state lifetime of the Ru-complexes dye spans from 20 to 60 ns.

$$S^* \rightarrow S^+ + e^- \quad \text{(2.3)}$$

The injected electrons diffuse throughout the TiO_2/TCO and TiO_2/graphene interfaces' mesoporous particle network, where they transmit to an external load. I^- instantly reduce the resultant oxidized dye to the ground state I^{3-} in the electrolyte **STEP 4** displayed in equation 2.4:

$$2S^+ + 3I^- \rightarrow 2S + I^{3-} \quad \text{(2.4)}$$

Recombination with electrons created in TiO_2 films occurs in the absence of a redox couple (I^-/I^{3-}) to decrease the oxidized dye (S^+) **STEP 5** (processes 4, 5 and 6 on figure 2.1b) illustrated in equation 2.5. It is commonly considered that charge recombination occurs primarily between photo generated electrons and the I^{3-} in electrolyte at the semiconductor/electrolyte and TCO/electrolyte interfaces. Many factors influence charge recombination, including semiconductor surface states (Bisquert *et al*., 2002), I^3 concentration (Nakade *et al*., 2005), charge trapping detrapping in semiconductor nanoparticles (Peter, 2007), and the molecular structure of the adsorbed dye (O'Regan *et al*., 2009; Miyashita *et al*., 2008).

$$S^+ + e^-(TiO_2) \rightarrow S \quad \text{(2.5)}$$

The generated I^{3-} is reduced back to I^- by the electrons that travel through the external load to the Pt counter electrode. Consequently, the electron transfer process in DSSCs is cyclic **STEP 6** shown in equation 2.6. The regeneration process is kinetically favored since process 5 typically occurs in the ~0.1 millisecond, Haque *et al*., (2000), which is substantially slower than the dye regeneration process (process 3).

$$I^{3-} + 2e^- \rightarrow 3I^- \quad \text{(2.6)}$$

2.4 Titanium Dioxide (TiO_2)

Titanium dioxide, referred to as titanium (IV) oxide or titania, is an inorganic compound having the chemical formula TiO_2. It is commonly used as a pigment, known as titanium white, Pigment White 6 (PW6), or CI 77891. Its octahedral geometry in all three major dioxides is linked to six oxide anions. The crystal structures of rutile and anatase are tetragonal, with oxide anions grouped in deformed hexagonal close packing in rutile, near to cubic close packing in anatase, and double hexagonal close-packing in brookite. Titanium dioxide's remarkable brightness and high refractive index make it the most commonly used white pigment. To maximize the reflection of visible light, its crystal size needs to be established. Due to its color and refractive index, it is a perfect reflecting optical coating for dielectric mirrors and for making exquisite thin films like mystic fire topaz. Titanium dioxide is also used in cosmetic and skin care products as a pigment, thickener, and sunscreen. Anatase TiO_2 has a bandgap of 3.26 eV, which corresponds to UV adsorption at 385 nm. However, its wide energy bandgap may limit its potential applications as a photocatalyst.

2.4.1 Dispersion of Titanium Dioxide

The stability of TiO_2 dispersion significantly affects the products' photocatalytic activity. TiO_2 particles and cementitious materials were previously blended as dry powders and diluted with water. According to Folli *et al*., (2010), this mixing method caused significant agglomeration of TiO_2 particles in the cement matrix, which decreased the amount of accessible active surface area in the cured cement. It was discovered that the hydrodynamic size of TiO_2 nanoparticles dispersed in an aqueous solution was greater than that of the parent particle. Probe-sonication has been shown by Jiang *et al*., (2009) to significantly reduce hydrodynamic size. Mixing TiO_2 particles with other materials may reduce active surface area due to photocatalyst particle encapsulation by hydration products. As a result, photocatalytic activity is severely constrained and vulnerable to aging (Lackhoff *et al*., 2003). TiO_2 dispersion in coatings was discovered to be an intriguing alternative since the coatings are in direct contact with pollution and photons and are less influenced by cement hydration (Krishnan *et al*., 2013). However, the coating method may be subject to harsh

weathering processes. As a result, to maximize the active surface area, the suitable dispersion method should be selected based on the intended use.

2.4.2 Porous Structure of Titanium Dioxide

The practical applicability of TiO_2 is significantly enhanced by immobilization on a solid conductive base. However, photocatalytic effectiveness may be lowered due to the mass-transfer limit and constrained active surface. The available active surface area significantly affects how well photocatalytic activity works in TiO_2-immobilized systems. The accessible active surface area is influenced by the pore structure of TiO_2. Before constructing an efficient photocatalytic process, the factors governing the available active-surface-area should be thoroughly studied. A dye-sensitized solar cell's (DSSC) porosity can influence electron transport and light absorption, both of which affect the total electrical current-voltage (I-V) characteristics. To investigate the relationship between dye-sensitized TiO_2 particles at high and low porosity levels, constant overlap and varied overlap are employed. The light absorption coefficient (α) and electron diffusion coefficient (D) are then calculated analytically based on porosity (P). Saito *et al*., (2004) examined the impact of porosity on cell performance and concluded that DSSC efficiency may be increased by modifying electrode porosity. The electron production, transport, and recombination of an irradiated DSSC under steady-state conditions can be expressed using the diffusion differential equation 2.7 (Sodergren *et al*., 1994):

$$D\frac{\partial^2 n(x)}{\partial x^2} - \frac{n(x)-n_o}{\tau} + \Phi_o \alpha e^{-\alpha x} = 0 \quad \text{.....(2.7)}$$

Where n(x) is the electrode thin film's excess electron concentration at point x. The electron concentration n_o in the dark ($n_o = 10^{16}$ cm^{-3}) (Ferber & Luther, 2001). The lifetime of free electrons in the conduction band is denoted by τ. The incident irradiation intensity is represented by ϕ_o. The nanoporous electrode's light absorption coefficient is denoted by α, and electron diffusion coefficient by D. One overlap in a high porosity electrode is often reported to generate a 2.5% reduction in internal surface area, equivalent to ΔS of 31 nm^2 (Van de Lagemaat *et al*., 2001). P is related to the total number of particles N and the coordination number CN (Benkstein *et al*.,

2003). P drops as *C*N increases. The porosity *P* is 0.41 for densely packed particles with a maximum *CN* 6 (Saito *et al.,* 2004). This *P* value serves as both the transitional point and the bottom bound ($P \geq 0.41$) for using this constant overlap approach. The relationship between α and *P* can be determined by examining the dye-sensitized TiO_2 porous thin film's total internal surface area. A series of equations need to be symbolically solved in order to determine α - *P* relationship:

(i) Dye-sensitized solar cell total internal surface area *S*

$$S = N(4pr^2 - CN\,\Delta S) \quad \text{(2.8)}$$

(ii) The ratio of TiO_2-free volume to total volume gives porosity, *P*

$$P = \frac{Vol - N\left(\frac{4}{3}\right)\pi r^3}{Vol} \quad \text{(2.9)}$$

(iii) Van de Lagemaat *et al*., (2001) showed a linear relationship between *CN* and *P*, with *CN* = 6 for *P* = 0.41 and *CN* = 2.5 for *P* = 0.75 (Van de Lagemaat *et al*., 2001; Benkstein *et al*., 2003).

$$CN = -10.29P + 10.22 \quad \text{(2.10)}$$

Using equations 2.9 –2.10 in conjunction with the fact that α is linearly proportional to *S* (Saito *et al.*, 2004), one may demonstrate

$$\alpha \propto (1 - P)(P + 2.89) \quad \text{(2.11)}$$

The unknown component can be estimated using a reference light absorption α = 5 x 10^3 cm^{-1} for *P* = 0.41 (Lee *et al*., 2004), and equation 2.11 generates equations 2.12 and 2.13

$$5 \times 10^3 \propto (1 - P)(P + 2.89) \quad \text{(2.12)}$$

$$a = 2568(1 - P)(P + 2.89) \quad \text{(2.13)}$$

Furthermore, the electrode porosity can influence electron transport, which is dependent on particle connection. The influence of *P* on the diffusion coefficient *D* can be expressed as equation 2.14 based on experimental results (Benkstein *et al*., 2003).

$$D = a|P - Pc|^m \quad \text{(2.14)}$$

where α, m, and Pc are constants whose values are 4 x $10^{-4}cm^2s^{-1}$, 0.82, and 0.76, respectively.

2.5 Graphene

For carbon compounds with all other dimensions, the fundamental building block is the two-dimensional carbonaceous substance known as graphene (figure 2.2). Its exceptional qualities have drawn a lot of attention.

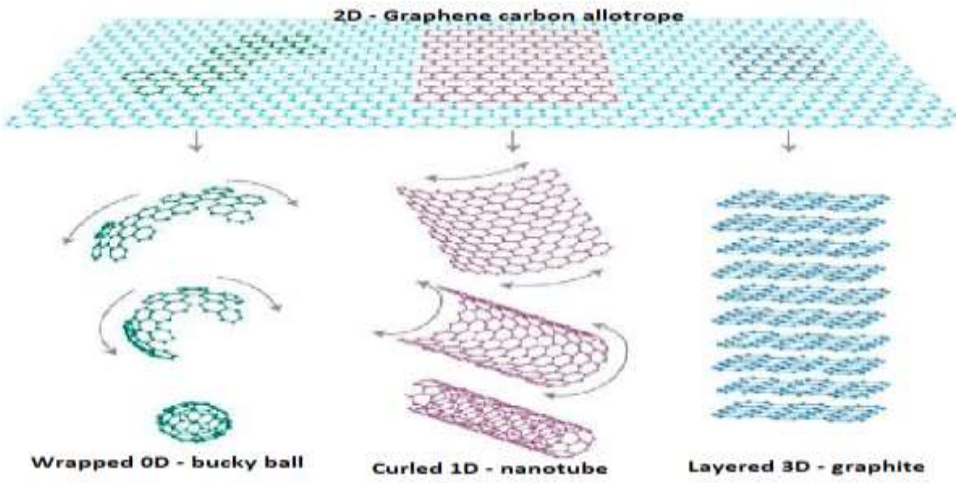

Figure 2.2: Graphitic formations: 2D Graphene, 0D Bucky Balls, 1D Nanotubes and 3D Graphite. Copyright Nature Publishing Group, (2007)

These characteristics include excellent carrier mobility (200 000 $cm^2\ V^{-1}\ s^{-1}$) (Bolotin *et al*., 2008), potent mechanical stability (Lee *et al*., 2008), significant thermal conductivity (5000 $W\ m^{-1}\ K^{-1}$) (Balandin *et al.*, 2008), and a large specific surface area (estimated value: 2630 $m^2\ g^{-1}$) (Stoller *et al*., 2008). Through chemical processes (Li *et al*., 2008), thermal exfoliation and micromechanical cleavage (Novoselov *et al*., 2005), graphene can also be made from bulk graphite. Graphene has a wide range of uses in the optical, electrical, and catalytic industries due to these properties.

2.5.1 Graphene Incorporation on TiO_2 as a Charge Transport Enhancer

Recent research has focused on graphene-based composite nanomaterials due to their synergistic effects. Graphene (*G*), with its large specific surface area and high electron mobility, can be added to TiO_2-based DSSC photoanodes to increase photocatalytic efficiency (*PCE*) by 40-58 % (Zhu *et al.*, 2010). The benefits of incorporating graphene include improved dye adsorption, as the anode films become more porous, increasing the surface area for additional dye sites and boosting light harvesting efficiency. Additionally, graphene dispersed in a TiO_2 matrix as seen in figure 2.3 forms a continuous *2D* conduction network, allowing effective transfer of photogenerated electrons across the matrix, inhibiting charge recombination and prolonging electron lifespan (Sun *et al*., 2010).

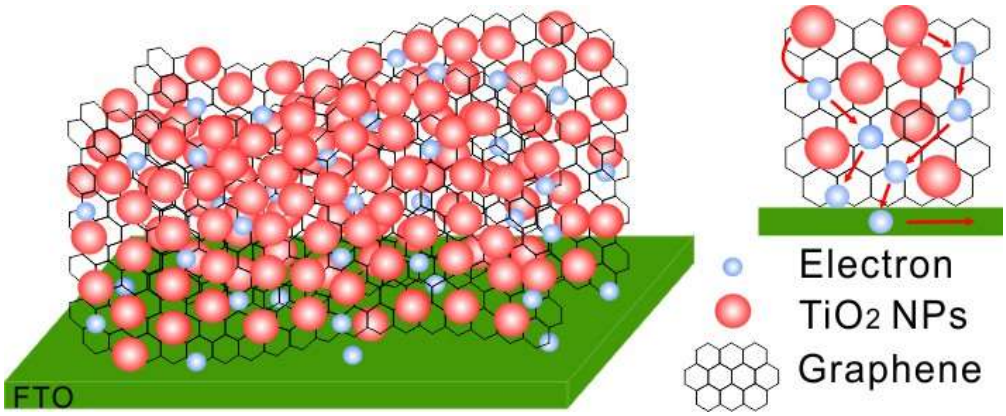

Figure 2.3: Schematic Representation of a TiO_2-Based Photo Anode Using 2D Graphene as an Electron Bridge

2.5.2 TiO_2 on Graphene Photo Catalysis and Band Configurations under Varying Conditions

When electron-hole pairs are photogenerated by UV light stimulation of $GTiO_2Ns$, a more positive Fermi level in graphene enables them to be injected into graphene (Hu & Tang, 2013). The TiO_2 conduction band 4.20 eV and graphene's work function of 4.42 eV, Cruz *et al*., (2017) facilitate this process, which leads to the injection of the electron from TiO_2 CB into *G*. Because of its great carrier mobility, graphene accelerates electron transport, enhancing photocatalytic efficiency. It also improves hole-electron separation, reducing recombination (Wang *et al*., 2014). The visible light

activation mechanism promotes the photogenerated electron from the *G* photo excited state and delocalizes it to the TiO_2 surface. It is crucial to understand that *G* in $GTiO_2Ns$ photocatalyst causes a red shift in absorption, which narrows the band gap and enhances the photo response's wavelength (Liu *et al*., 2013). In this instance, photoexcited electrons in high-energy *G* states are delocalized into the TiO_2 surface with the dissipation of excess energy due to electron vibrational interaction (Long *et al*., 2012). The electrons then react with oxygen to form superoxide radicals when visible light excites $GTiO_2Ns$. When a dye (*D*) is efficiently adsorbed onto the photocatalyst surface, it acts as a sensitizer for visible activation as well as a pollutant during the photocatalytic process, promoting electron transfer from the excited dye molecules state to the TiO_2 *CB* while *G* acts as an electron scavenger, as in the *UV* mechanism (Pastrana – Martinez *et al*., 2012). Figure 2.4d summarizes the schematic mechanism illustration of the photo degradation process of $GTiO_2Ns$. The oxygen vacancy and Ti^{3+} exist in the TiO_2 bandgap as OV^+, $[OV: Ti^{3+}]^+$ and $[OV: 2Ti^{3+}]^0$ with annealing (Ricci *et al.,* 2010). The neutral $[OV: 2Ti^{3+}]^0$ has a tendency to change to $[OV: Ti^{3+}]^+$ when exposed to light and oxygen. Visible-light activity may decrease as a result of this shift if the oxygen vacancy color center migrates upward.

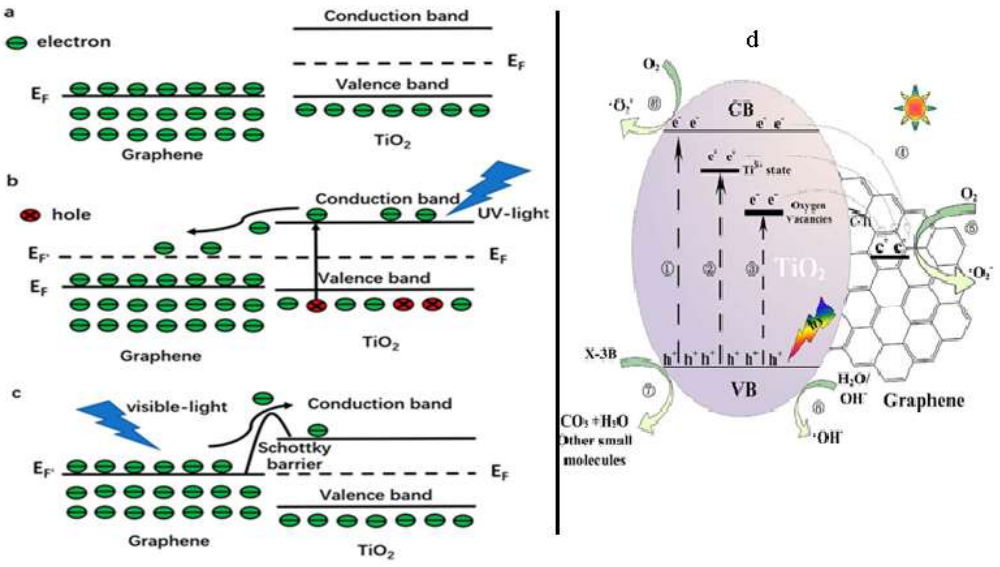

Figure 2.4: Band Structures and Interface Interactions of Graphene-TiO_2 (a) before Combination (b) under UV-Light Irradiation and (c) under Visible Light Irradiation (d) Mechanism Illustrations of Photo Catalysis for GTiO_2Ns Composite under Visible Light Irradiation (Tang *et al.*, 2018)

Moreover, the creation of a C-Ti bond may enhance the efficiency of an electron's transfer from TiO_2 to graphene, combating recombination and prolonging the lifetime of separated carriers, in addition to further lowering the bandgap of TiO_2, enabling a photocatalytic response of GTiO_2Ns in the visible light region.

Pristine graphene TiO_2 junction (before contact), with Fermi values of 0V and 0.5V respectively, is shown in figure 2.4 (a). The composite as a whole undergoes thermal equilibrium, resulting in a constant Fermi level, and a metal-semiconductor contact, or junction, occurs at the interface (graphene is a semimetal with a zero band-gap structure) (Hu & Tang, 2013). Consequently, in the absence of illumination or when exposed to UV radiation, electrons will spontaneously move from the TiO_2 conduction band into the Fermi level of graphene as displayed in figure 2.4(b) (Zhang *et al.*, 2008). On the graphene side, a Schottky barrier then forms, and on the TiO_2 side, an intrinsic potential barrier. When graphene is exposed to visible light, a large number of electrons are excited on the Fermi level. The Schottky barrier must be overcome (quantum tunneling) before these electrons may inject into the TiO_2 conduction band (Figure 2.4(c)). A sufficiently substantial depletion layer that obstructs electron transit

is created when a metal-semiconductor junction is composited with bulk materials. However, because their diameters are much smaller than the space-charge area (the barrier width is limited), there is no discernible band bending in the graphene-TiO_2 composite (Tang *et al.,* 2010). Through thermionic emission and quantum tunneling, photogenerated electrons excited in graphene can be injected into TiO_2 to go beyond the narrow Schottky barrier. Due to the greater barrier (Schottky barrier height equals the difference between graphene's work function and TiO_2's electron affinity, ≈ 2 eV), the thermionic emission (thermal voltage ≈ 26 meV) is insufficient at ambient temperature to accomplish the transfer (Fuentes *et al*., 2002). Consequently, quantum tunneling is the only way to achieve electron transport. The width of the Schottky barrier, which is typically less than three layers at ≈1 nm, is much shorter than the mean free path of electrons in graphene and TiO_2, but this shows that no significant additional collisions, such as electron-electron or electron-phonon collisions, occur. The energy of photo-induced electrons in graphene is higher than the inherent Fermi level of graphene due to the Pauli Exclusion Principle (the actual Schottky barrier is less than 2 eV) (Hu & Tang, 2013). The tunneling probability of photo-generated electrons is 5.21×10^7 when the graphene used is 1 nm thick (with an input light intensity of 100 $mWcm^{-2}$, over 10^{11} electrons can inject into TiO_2 from graphene each minute) (Hu & Tang, 2013).

2.6 UV VIS Spectroscopy

Optical properties are those attributes that relate to the way light interacts with semiconductors. These include absorption, transmission, extinction, band gap energy, refractive index, and reflectance. The theoretical considerations for these optical properties are presented in subsequent sections.

2.6.1 Optical Properties of a Heterojunction

When light strikes a semiconductor material, it can be absorbed, transmitted through, or reflected off its surface. The absorption coefficient of a substance indicates how strongly a particular photon is absorbed by it. Since it is a material attribute, its value varies depending on the substance. The absorption value, which is a critical component in determining the required film thickness to absorb the bulk of the solar energy that

strikes the material, is determined by the wavelength of the monochromatic radiation. Equation 2.15 illustrates the absorption coefficient as a function of transmittance (T %) Tepantlan *et al.*, (2008).

$$\alpha(\lambda) = \frac{1}{z}\left(\frac{100}{\%T}\right) \quad \text{..... (2.15)}$$

where z is the sample thickness. The absorbance of TiO_2 represents the number of photons absorbed by the thin films and may be calculated using Equation 2.16 (Shinen *et al*., 2018).

$$A_b = 1 - \left(T_r + T_f\right) \quad \text{..... (2.16)}$$

where T_r stands for transmittance, R_f for reflectance, and A_b for absorbance of the thin films. According to Voss *et al*. (1998), the absorption coefficient can be described as the reciprocal of the depth to which electromagnetic (*EM*) radiation penetrates the thin layer. Conversely, the extinction coefficient (equation 2.17) is associated with the damping factor or *EM* field amplitude decline.

$$K_{ex} = \frac{\alpha\lambda}{4\pi} \quad \text{..... (2.17)}$$

Another way to think about the extinction coefficient is as an indicator of *EM* radiation that has been absorbed. In that instance, $K_{ex} > 0$ denotes absorption while $K_{ex} = 0$ denotes no *EM* radiation absorption by the films (Voss *et al.*, 1998). The refractive index (n) measures how a light beam bends as it travels from one medium to another. Equations 2.18 can be used to compute the refractive index of TiO_2 thin films using their reflectance and extinction coefficients.

$$\mathrm{n} = \left[\frac{1+\mathrm{R}}{1-\mathrm{R}}\right] + \sqrt{\frac{4\mathrm{R}}{(1-\mathrm{R})^2} - \mathrm{k}^2} \quad \text{..... (2.18)}$$

where *R* is the reflectance and *k* is the extinction coefficient. The porosity and relative density of the film were calculated using equation 2.19 (Liu *et al*., 2005) and 2.20 (Ohyama *et al*., 1997);

$$Porosity = \left(1 - \frac{n^2-1}{n_0^2-1}\right) \times 100\% \quad \text{..... (2.19)}$$

$$Relative\ density\ = \frac{n^2-1}{n_0^2-1} \times 100\% \quad \text{..... (2.20)}$$

where n is the refractive index of the films and $n_0 = 2.52$ the refractive index of anatase TiO_2 (Mathews *et al.*, 2009). The region between the bottom of the conduction band (CB), which is electron-free, and the top of the valence band (VB), which is completely packed with electrons, is known as the optical band gap in an intrinsic semiconductor. The energy range where the density of states is zero is ideal. In insulators, the optical band gap is huge, while in metals, it is nonexistent. The band gap in semiconductors is frequently midway between these two. A semiconductor's capacity to absorb solar spectrum light is determined by the size of its band gap. The band gap of a semiconductor is explored using light with different photon energies close to the band gap. Details about the valence band and conduction band energy state transitions are explained by the gradual change from absorption to transmission. Absorption edge refers to the area of this transition. It is challenging to determine the absorption edge experimentally because a tail appears in the absorption spectra. The Tauc model was designed to empirically estimate the optical band gap (Sanchez, 2014). Equation 2.21 (Tauc, 1966; Shinen *et al*., 2018; Zhao *et al.*, 2011), representing the Tauc model, is used to investigate the optical absorption edge in semiconductors.

$$\alpha h\upsilon = B\left(h\upsilon - E_g\right)^m \;\ldots\ldots\ldots\ldots\ldots\ldots\ldots\ldots\ldots\ldots\ldots\ldots\ldots \;(2.21)$$

where h is Planck's constant, m is a constant that takes the values m = 2 for an indirect band gap and m = 1/2 for a direct band gap (Gould & Lamont, 2010), and E_g is the optical band gap energy. The absorption coefficient is denoted by α. The band tailing parameter, or proportionality constant, B, has a range of values from 10^7 to 10^8 m^{-1} (Illican, 2008).

2.6.2 Refractive Index of Thin Films

Semiconducting materials' major characteristic is their refractive index, which is determined by transmission, local field strength, and electronic polarization. The energy band gap, absorption coefficient, refractive index, wavelength of incident photons, and extinction all have a significant impact on a semiconductor thin film's optical conductivity (σ_{opt}) and electrical conductivity (σ_e). The optical conductivity (σ_{opt}), electrical conductivity (σ_e) and absorption coefficient are related by equation 2.22 and 2.23 in that order (Astinchap *et al*., 2017).

$$\sigma_{opt} = \frac{\alpha nc}{4\pi} \quad \text{..... (2.22)}$$

$$\sigma_e = \frac{2\lambda\sigma_{opt}}{4\pi} \quad \text{..... (2.23)}$$

where c is the radiation's velocity, n is its refractive index, α absorbance, and λ wavelength.

2.6.3 Single Oscillator Model Parameters

Since dispersion plays a major role in optical communication and the development of devices for spectrum dispersion, it is an important field in optical material research. The refractive index dispersion below the absorption edge can be studied using the Wemple-DiDomenico (W-D) single-oscillator model represented by equation 2.24 (DiDomenico and Wemple, 1969).

$$n^2 = 1 + \frac{E_d E_o}{E^2 - (h\nu)^2} \quad \text{..... (2.24)}$$

where the dispersion energy E_d, the effective dispersion oscillator energy E_0, the refractive index n, the Planck's constant h, the frequency ν, and the photon energy hν are used to quantify the average strength of interband optical transitions. Plotting $(n^2-1)^{-1}$ against $(h\nu)^2$ yields a straight line with a slope of $(E_d E_0)^{-1}$ and an intercept on the vertical axis equal to E_o/E_d. The values of the parameters E_d and E_0 are therefore evaluated. Single oscillator model defines oscillator strength by equation 2.25 (DiDomenico and Wemple, 1969).

$$f = E_o E_d \quad \text{..... (2.25)}$$

E_o and E_d oscillator parameters are dependent in the moments of the optical transitions M-1 and M-3 defined by model given by equation 2.26 (Wemple & DiDomenico, 1971).

$$E_o{}^2 = \frac{E_{-1}}{E_{-3}} \;\; and \;\; E_d{}^2 = \frac{E_{-1}{}^3}{E_{-3}} \quad \text{..... (2.26)}$$

The W-D dispersion parameter, E_0, determines the optical band gap values, E_g, using equation 2.27 (Marquez *et al.,* 1999).

$$E_g{}^{W-D} \approx \frac{E_0}{2} \quad \text{(2.27)}$$

Dispersion energy, E_d can be related by equation 2.28 to determine the coordination number (N_c) (Tan *et al*., 2006; Marquez *et al*., 1995).

$$E_d = \beta N_c Z_a N_e \quad \text{(2.28)}$$

where β is a covalent or ionic value = 0.37eV (Wemple & DiDomenico, 1971) for covalent materials.

According to Wagner *et al*., (2007) nonlinear polarizability parameter also known as nonlinear optical susceptibility χ^3 and the linear optical susceptibility χ^1 can be determined using Miller equation 2.29 which is very convenient for visible and near infra-red frequencies.

$$\chi(3) = C\left(\chi^{(1)}\right)^4 = C\left[\frac{E_o E_d}{4\pi E_o^2 - (h\nu)^2}\right]^4 = \frac{C}{(4\pi)^4\left(n^2-1\right)^4} \quad \text{(2.29)}$$

where C is a constant, C = 10^{-10} esu.

2.6.4 Dielectric Properties of Composites Materials

The expression for the complex dielectric constant is given by equation 2.30

$$\mathcal{E} = \mathcal{E}_1 + i\mathcal{E}_2 = n^2 = (n \pm ik)^2 = (n^2 - k^2) + i2nk \quad \text{(2.30)}$$

The real and imaginary parts are denoted by $\mathcal{E}_1$ and $\mathcal{E}_2$, respectively. Equations 2.31 and 2.32 represent the real and imaginary components of the dielectric constant (Makhlouf *et al.,* 2014):

$$\varepsilon_1 = n^2 - k^2 \quad \text{(2.31)}$$

$$\varepsilon_2 = 2nk \quad \text{(2.32)}$$

where $k = \alpha\lambda/4\pi$. The power loss factor (tan δ) associated with the electric behavior of the film is described by equation 2.33;

$$\tan \delta = \frac{\varepsilon_2}{\epsilon_1} \quad \text{..... (2.33)}$$

Equation 2.34 can be used to generate the complex interband from the real and imaginary parts of the dielectric constant.

$$\boldsymbol{J_{cv} = J_{cv1} + J_{cv2} = \frac{m_o{}^2 4\pi^2}{e^2 h^2} \frac{(hv)^2}{2} (\varepsilon_1 + i\varepsilon_2)} \quad \text{..... (2.34)}$$

where m_o is an electron's mass, e is its charge, and h is the Plank's constant. According to Loughin *et al.* (1996), the real part interband transition J_{cv1} and the imaginary part interband transition J_{cv2} are proportional to the dielectric transition strength. Pre multiplier $\frac{m_o{}^2 4\pi^2}{e^2 h^2}$ is used as 8.289 x 10^{-6} $gcm^{-3}(eV)^{-2}$ for convenience computation. The surface energy loss function (*SELF*) and volume energy loss function (*VELF)* express the energy transmitted to and from the topmost atom layer of a compound semiconductor due to electron excitation in the surface and bulk. Equations 2.35 and 2.36 analyzed *SELF* and *VELF* losses, respectively (Al-Mudhaffer *et al.* 2012).

$$S_{elf} = \left\{-\frac{1}{\varepsilon}\right\} = \frac{\epsilon_2}{(1+\epsilon_1)^2+\epsilon_2^2} \quad \text{..... (2.35)}$$

$$V_{el} = \left\{-\frac{1}{1+\varepsilon}\right\} = \frac{\epsilon_2}{\epsilon_1^2+\epsilon_2^2} \quad \text{..... (2.36)}$$

2.7 Fourier Transform Infrared Spectroscopy

The quality, vibration, and rotation of the molecular groups in the material, as well as any impurities present in the deposited thin films, may all be determined from the FTIR spectra. The FTIR spectrometer tests *IR* transmission at room temperature in the wave number range of 4000 to 400 cm^{-1}.

The Michelson interferometer, which is used to control light, is the brains behind contemporary FT-IR spectrometers. The Michelson interferometer works on the basis of splitting incoming light from a broadband light source using a beam splitter into a transmitted and reflected beam. A stationary and moving mirror reflect beams, causing interference at different locations. The Fast Fourier Transform (FFT) algorithm (equation 2.37) uses digitized interferogram data to create a frequency spectrum plotting signal intensity against wavenumber (Peter & James, 2007).

$$S(\nu) = \int_{-\infty}^{+\infty} I(x) e^{-i2\pi\nu x}\, dx \quad \text{..... (2.37)}$$

where I(x) is the interferogram as a function of optical path difference (x) and S(ν) is the spectrum as a function of frequency ν.

2.8 Surface Charge Distribution and Electron Transport Mechanism

2.8.1 Surface Charge Density

Scanning Kelvin Probe Microscopy (SKPM), an electric force microscopy, according to Margliano *et al*., (2013), detects the contact potential difference (V_{CPD}) between the conductive tip and the sample tip. Equation 2.38 defines the V_{CPD} (Maragliano *et al*., 2014):

$$V_{CPD} = \frac{\Delta\Phi}{q} = \frac{\Phi_{tip} - \Phi_{sample}}{q} \quad \text{..... (2.38)}$$

where, q represents the electric charge, Φ_{sample} denotes the sample's work function, and Φ_{tip} denotes the tip's work function. The primary foundation of the SKPM physical principle is contact potentials. Simon & Jun, (2012) reported that the distribution of local work function is correlated with the lateral distribution of *CPD* from the electrostatic tip – surface force. Information about surface charge is provided via the surface potential differential (SPD), which is the contact potential difference (Simon & Jun, 2012). A surface method for determining the concentration of charge carriers on a material's surface is designated as SKPM. Both the tip and the back contact are grounded while scanning the sample in tapping mode. The surface charges flow towards the electric ground when a closed circuit is used, causing the surface to discharge

2.8.2 The Hall Effect

According to Hall, E 1879 an electric potential difference proportional to the magnetic field and the current occurs across the material in a direction perpendicular to both current and potential when a magnetic field is applied transverse to the direction of an electrical current in a conductor (see figure 2.5). The magnetic force (F_B) equals the

electric force (F_E) at equilibrium, and equation 2.39 gives the generated Hall Voltage (V_H) for a conductor of width w;

$$V_H = E_H w = V_x B_z w \quad \text{..... (2.39)}$$

where B_y is the y-directional magnetic field, V_x is the average charge carrier velocity, V_H is the Hall voltage and E_H is the measured Hall electric field.

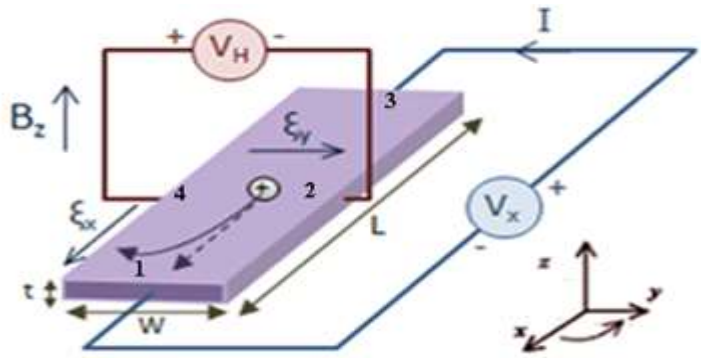

Figure 2.5: Principle of Hall Voltage Measurements using Hall Effect (Hall, E. 1879)

When an applied magnetic field orthogonal to the current and an electric current in the conductor creates a voltage differential (the hall voltage) across a semiconductor, the Hall Effect occurs. Delivering a dc current, I into contact 1 and out of contact 2 (I_{12}) and measuring the voltage (V_{43}) from contact 4 to contact 3, as illustrated a vertical resistance R_A is achieved as shown in figure 2.5. For horizontal resistance R_B, current ((I_{23}) was applied into 2 then out of 3 while measuring voltage (V_{14}) from contact 1 to contact 4. To compute R_A and R_B equation 2.40 is applied.

$$R_A = \frac{V_{43}}{I_{12}} \quad and \; R_B = \frac{V_{12}}{I_{23}} \quad \text{..... (2.40)}$$

The Van Der Pauw technique was used to calculate sheet resistance *Rs* of the sample by equation 2.41 (Van der Pauw, 1958);

$$\exp\left(\frac{-\pi R_A}{R_S}\right) + \exp\left(\frac{-\pi R_B}{Rs}\right) = 1 \quad \text{..... (2.41)}$$

Hall (1879) proposed equations 2.42, 2.43, and 2.44 to determine charge concentration (n_s), mobility (μ), and conductivity (σ).

$$n_s = \frac{IB}{q|V_H|} \quad \text{(2.42)}$$

where *I* is the current, q is the electron charge, V_H is the hall voltage, and B is the magnetic field.

$$\mu_S = \frac{|V_H|}{R_S IB} = \frac{1}{qn_S R_S} \quad \text{(2.43)}$$

$$\sigma = \frac{1}{\rho} = qn_S\mu_S \quad \text{(2.44)}$$

2.9 The SCOUT Software

To determine the optical parameters of thin layers, a theoretical analysis of experimental (such as transmittance and reflectance) data was simulated in the scout software using a variety of dielectric models, specifically the O'Leary-Johnson-Lim (OJL) and Drude models. The OJL model uses a fitting algorithm in the SCOUT software to match experimental optical spectra in order to obtain optical properties from a material's dielectric function. To determine optical absorption, it makes use of variables such as the decay constant, valence band tail state exponent, and band gap energy. SCOUT uses the downhill simplex approach to modify these parameters in order to minimize the discrepancies between the measured and simulated spectra. This allows properties of materials such as refractive index and band gap to be extracted.

The SCOUT software's Drude model minimizes differences between measured and computed data through an iterative fitting procedure to retrieve optical properties. In order to derive material properties, it modifies parameters until the computed response conforms with experimental data. Constants such as the refractive index *n*, extinction coefficient *k*, and absorption coefficient α are determined by the application of the Drude model for optical constant analysis.

2. 10 Evaluating a Solar Cell

The power conversion efficiency (*PCE* or η) of the solar cells is determined using the *J-V* curve data from photoelectric current measurements. To compare the *PCE* of the solar cells manufactured in different laboratories, the J-V curves should be evaluated under standard conditions, such as the standard solar spectrum (AM 1.5 G with a power density of 1000 W m^{-2}) and the recommended cell temperature (25 °C) (Smestad *et al.*, 2008; Hagfeldt *et al.*, 2010). At a potential of 0 V, the photocurrent per unit active area of the device is expressed as *Jsc*. The incident irradiance on the cell surface, dye loading, dye molecular structure, and the electrochemical properties of the mesoporous electrode layer affects a DSSC's *Jsc* (Jose *et al.*, 2009). The subsequent equation 2.45 yields the dark current density (J_{dark}) (Maluta, 2010).

$$J_{dark} = J_o\left(exp\left(\frac{qV}{k_B T_{emp}}\right)\right) \quad \text{(2.45)}$$

where q is elementary charge, V is the voltage between the terminals, k_B is Boltzmann's constant, and T_{emp} is temperature, J_{dark} is the reverse bias saturation current density.

When the circuit's terminals are connected together and no voltage is provided across the device, the current drawn is referred to as the short circuit current density (*JSC*). In order to calculate the net current density (J), deduct the dark current density (J_{dark}) from the short circuit current density (*JSC*).

$$J = J_{SC} - J_{dark} = J_{SC} - J_o\left(exp\left(\frac{qV}{k_B T_{emp}}\right) - 1\right) \quad \text{(2.46)}$$

With increasing light intensity, (J_{SC}) rises linearly. Along with the electrochemical or electrokinetic characteristics of the red-ox pair in the electrolyte, J_{SC} also depends on the quantity of dye chemisorbed onto the semiconductor.

The difference between the redox couple's electrochemical potential and the metal oxide's Fermi level mostly determines the *Voc*.

$$V_{oc} = E_F - \Delta V_{redox} \quad \text{(2.47)}$$

In the meantime, the sensitizer adsorption behavior and the recombination rate are also important factors (De Angelis *et al.*, 2007). The open circuit voltage (V_{OC}) is

determined by the equation that follows when the circuit is open, with $J_{dark} = J_{SC}$ (Maluta, 2010). V_{OC} rises logarithmically with short circuit density (J_{SC}) and to the reciprocal of the reverse saturation current (J_0), as demonstrated by equation 2.48.

$$V_{oc} = \frac{k_B T_{emp}}{q} ln\left(\frac{J_{sc}}{J_o} + 1\right) \quad \text{..... (2.48)}$$

The IV-curve's squareness is the definition of the fill factor (*FF*). The *FF* determines the ideality of solar cells, which is the ratio of maximum power output (P_{max}) to the product of J_{sc} and V_{OC}. The photocurrent density (J_{mp}) and voltage (V_{mp}) that correspond to the P_{mp} point can be computed using the following equation 2.49.

$$FF = \frac{Maximum\ power\ (P_{mp})}{J_{SC} \times V_{OC}} = \frac{J_{mp} \times V_{mp}}{J_{SC} \times V_{OC}} \quad \text{..... (2.49)}$$

The low fill factor can be attributed to the charge recombination mechanisms operating within the DSSC. The series resistance in the DSSC must be as low as feasible while the parallel shunt resistance must be as high as possible to produce a high *FF*. In theory, the best solar cell will have a perfectly square I-V curve with *FF = 1*. A cell of this type will provide the same current regardless of voltage. However, no such level of squareness has been reached in practice.

The ratio of P_{mp} to the incident irradiance (*Pin*) on the device surface is generally referred to as the *PCE* (equation 2.50). *PCE* can rise with increasing *Jsc*, *Voc*, and *FF*. Photoanode performance tuning is a useful tactic to raise the DSSC performance because all of these photovoltaic parameters are directly impacted by the mesoporous semiconductor network's characteristics.

$$\eta(\%) = \frac{Power\ output \times 100\%}{Incident\ power} = \frac{J_{SC} V_{OC} FF(mW) \times 100\%}{Area\ (cm)^2 \times Pin(mW/cm^2)} = \frac{J_{SC} V_{OC} FF}{Pin} \quad \text{..... (2.50)}$$

2.11 Research Gap

Solar cells are widely used for electricity and charging devices, but their initial cost has hindered their widespread adoption. Dye-sensitized solar cells, costing one-third of silicon-based cells and has exceeded 10% efficiency, are commercially feasible. TiO_2 is gaining attention in solar energy conversion applications. The electron diffusion coefficient of the nanocrystalline TiO_2 film (~ 5×10^{-5} cm^2 s^{-1}) is more than

two orders of magnitude less than that of the bulk material because of the many grain boundaries that hamper electron transport (Zhu *et al*., 2012). Charge transport in semiconductor-based metal oxide electrode films is slower than dye regeneration and electron injection, making electron transport a limiting step in charge transfer processes (Listorti *et al*., 2011). Although DSSC technology has achieved above 12% conversion efficiency in lab settings, additional advancements in cell performance and stability are still required to guarantee at least 6% PCE from DSSC commercial products with a 20-year lifespan (Wang *et al.*, 2010). Despite its benefits, TiO_2's wide 3.2 eV band gap restricts its range of light absorption to the ultraviolet. Therefore, it is necessary to extend the light absorption ranges toward the visible region to achieve effective solar energy conversion with TiO_2. This can be accomplished by coupling visible responsive materials like graphene with TiO_2, which can enhance the electron generation effect. The main challenges for the commercialization of nanocrystalline DSSC is improving photo anode crystallinity, ensuring efficient electron transport, and optimizing dye loading for improved PCE. This project's primary goal is to increase photogeneration and electron transport in the anode films by designing and synthesizing TiO_2 on graphene nanocomposite and optimizing the material's porosity, dispersion energy, and energy losses for DSSC performance improvement.

CHAPTER THREE

MATERIALS AND METHODS

3.1 Background

The experimental methodologies, characterization using various analytical facilities, and various film application measurements used in this study are all covered in this chapter. The components and chemicals employed, film formation of TiO_2 coated on conducting glass (Fluorine Tin oxide (FTO) and graphene), and on glass substrate are all part of the experimental procedure. The surface modification, film porosity and dispersion energy for enhancement of electron transport of films received special attention. Furthermore, the sorts of characterization methods used to analyze surface morphology and cross-sectional morphology are described. The photocatalytic experiments on TiO_2 - FTO and TiO_2-Graphene are also reported, as the application experiments to Dye Sensitized Solar Cells.

3.2 Chemicals and Materials

Titanium nanoxide T/SP (18 % wt, 15-20 nm, Solaronix, Switzerland), titanium (IV) chloride (99 %), acetic acid (99.8 %), and ethanol (anhydrous) were sourced from Sigma-Aldrich. Ethanol (99.8 %), n-butanol (99 %), and hydrochloric acid (37 %) were obtained from JKUAT University Laboratory. Dye sensitizer [RuL_2 (NCS) 2:2TBA], also known as N719, and the liquid iodide electrolyte (Iodolyte AN-50) was sourced from Solaronix. Charm Graphene CO., LTD, South Korea supplied graphene monolayer. Graphene was deposited to a glass substrate using Roll-to-roll (*R2R*) chemical vapor deposition (*CVD*) and wet transfer synthesis methods. Deionized (DI) water (18.2 M) and *FTO* coated glass substrate (7-8 Ωsq^{-1}), (sourced from Xinyan Technology Co. Limited, China), were used for the experiments.

3.3 Fabrication of Working and Counter Electrodes

3.3.1 Cleaning of Conducting Glasses

Cleaning the FTO and graphene on glass is a critical stage. If any contamination from the cleaning process remains on the conductive glass or any external dust particles, it causes a slew of issues such as decreased efficiency of the solar cell. As a result, it is critical that the cleaning process for the glasses be prioritized. The FTO and graphene on glasses were first cleaned with a detergent in an ultrasonic bath for 15 minutes, followed by a rinse with Deionized (DI) water and another 15-minute ultrasonic bath. It was then rinsed with water and then with ethanol. After washing, the glass was placed in a sterile desiccator to avoid contamination and was handled with care using new gloves.

3.3.2 Preparation of Photo Anode

For the DSSCs, the SnO_2: F and graphene glass substrates were cut into 2 x 1.5 cm. The cleaned conducting glass was submerged in a 40 mM $TiCl_4$ solution at 70 °C for 30 minutes before being washed with *DI* water and ethanol. Tracing a 1 x 1 cm^2 window on scotch magic tape and placed on the conductive side (determined through continuity testing with a multitimeter) of the glass substrates. The titanium nanoxide paste was then placed in front of a tapered blade at a set distance from the substrate, and then moved in-line with the substrate, generating a thin film (Frederichi *et al*., 2021) as illustrated in figure 3.1.

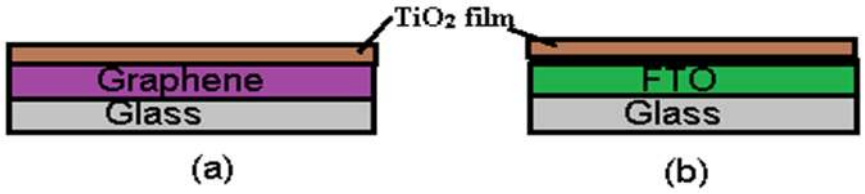

Figure 3.1: Schematic Diagram of TiO_2 Deposited on FTO and Graphene

After about 3 minutes of air relaxation, the films were dried by blowing hot air at 125 °C for 10 minutes.

3.3.3 Calcination of Deposited Films

Figure 3.2 shows Nabertherm muffle furnace (30-3000 °C) used to anneal films with thermal processes realized by customized system solutions. Nabertherm muffle furnace supporting tubes equipped with heating elements to provide free heat radiation and a longer lifespan. The oven's working area's high-performance forced air circulation ensures the highest level of temperature homogeneity. To protect the load and furnace, it has an adjustable cutout temperature and an over-temperature limiter. The entrance and chimney with fan both provide an adjustable air inlet.

Figure 3.2: Nabertherm Muffle Equipment Setup for Thermal Annealing Available at JKUAT Food Science Laboratory

In order to eliminate impurities from the furnace, the temperature was gradually increased from 25 ^{o}C to 450 ^{o}C at a rate of 5 ^{o}C per minute. After that, the films were cooled by gradually reducing the temperature at the same rate of 5 ^{o}C per minute (Ngei, 2016). Additionally, manufactured TiO_2 thin film samples were annealed at varying annealing rates of 1 ^{o}C per minute and 2 ^{o}C per minute in order to improve their roughness and crystallinity. The films were then sintered for 30 minutes at 450 ^{o}C. More films were exposed to a one-step annealing process that raised the temperature from 25 ^{o}C to 450 ^{o}C.

3.3.4 Ruthenium N719 Dye Preparation and TiO_2 Dye Sensitization

The cis-diisothiocyanato-bis (2,2'-bipyridyl-4,4'-dicarboxylato) ruthenium (II) bis(tetrabutylammonium) dye, which has a molar mass of 1188.6 g/mol, was prepared by dissolving 200 mg of N719 dye, acquired from Solaronix, Switzerland, in 100 mL of ethanol (99.5 wt - %) in a conical flask to create N719 ruthenium dye. The molar equation (3.1) was used to compute the dye's concentration.

$$C = \frac{m}{V}\frac{1}{MW} \quad \text{..... (3.1)}$$

where m stands for mass of dye in grams, *V* for formula weight, and MW for relative formula mass of the dye, *C* indicates molar concentration in mol/L. To make sure every particle dissolved, aluminum foil was placed over the flask and stirred well using a magnetic stirrer. To create 0.5 mM of N719 dye solution, 236.53 mL of ethanol was added and swirled using a micropipette and measuring cylinder. After that, the established solution was stored in a dark sample vial, covered with aluminum foil, ready for use. The produced photoanode was sensitized by gently submerging it in a dye bath solution contained in staining boxes. The staining boxes were filled with dye, and the working electrodes carefully submerged. Each staining box held a single film to guarantee there was no contact-related damages on the TiO_2 film. To avoid the films coming into contact with the staining boxes' walls, they were positioned with their TiO_2 coated side facing up. For the highest amount of dye loading, the electrodes were left in the staining boxes for 24 hours. A UV-Vis-NIR spectrophotometer was used to quantitatively analyse the dye loading in each sample.

3.3.5 Preparation of a Platinized Counter Electrode for Use as a Cathode

While the reference counter electrode (CE) was based on the widely used platinum (Pt) – film on glass substrate, several other CEs based on coating Pt on the FTO and graphene substrate were prepared. Schematic designs for the Scotch tapes cutting into 1 x 1 cm^2 windows were positioned on the conductive sides of the FTO and graphene glass substrates. For the reference module, a doctor-blade method was used to coat a platinum layer with a platisol T/SP pore size of 15-20 nm (Solaronix, Switzerland)

onto the window of the conductive side of the bare glass/FTO and glass graphene substrate. CE modules are displayed in Figure 3.3.

Figure 3.3: Schematic Diagrams of the CE Modules Prepared, Showing (a) Glass/Gr/Pt (b) Glass/FTO/Pt

Uniform pressure was applied at the pasting zone to ensure a uniform film thickness. The platinized FTO and graphene modules were placed in a dry, clean petri dish and covered with aluminum foil for 20 minutes before the scotch tape was gently removed. This was done to increase uniformity by eliminating any trapped air and reducing surface roughness. After heat-treating the modules in a furnace at a rate of 1 ^{o}C/min to 170 ^{o}C and then 5 ^{o}C/min to 400 ^{o}C, they were sintered for 30 minutes and then left to cool to room temperature.

3.3.6 Electrolyte Solution

The electrolyte solution was made with Grätzel paper, and all solutions were listed in molarity. In the initial solution, 0.6 M (1.6g) BMII (1 Butyl-3-methylimidazolium iodide), 0.03M (0.07g) I2, 0.1M(0.12 g) guanidinium thiocynate, and 0.5M(0.68g) 4-tert-butylpride [2] was added. The initial solution mixture contains (1.5 ml) valeronitrile and (8.5 ml) acetronitrile in that order. To avoid deterioration of the liquid, the solution must be kept in a closed opaque container. A pre-drilled pinhole in the counter electrode allowed the liquid iodide electrolyte to be injected into the device's interior; the other pinhole allowed air to escape from the sealed compartment. A small cover slip and a piece of parafilm were used to seal both pinholes after the injection.

3.4 Assembly of the Solar Cell

To form a sandwich arrangement, the dye-sensitized TiO_2 photoelectrode was placed over a platinum coated counter electrode. The cell's edges were sealed by hot pressing the two electrodes together and sandwiching a 25-µm thick hot-melt Surlyn monomer gasket between them. Two tiny (0.5mm) holes were drilled on the counter electrode (*CE*) to allow the iodine/tri-iodide red-ox couple electrolyte to be placed inside the sandwich configuration. Consequently, the holes in *CE* were sealed with a small piece of microscope covering plastic, as shown in figures 3.4.

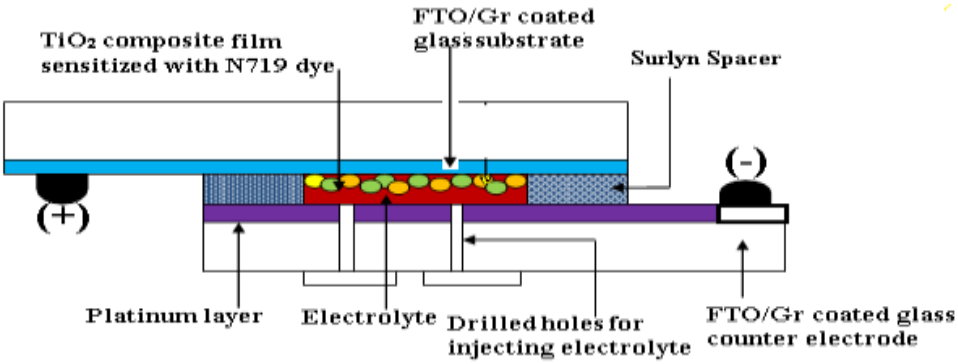

Figure 3.4: Schematic Diagram of an Assembled Dye-Sensitized Solar Cell with a TiO_2/Gr/FTO Composite Electrode Film

DSSCs were fabricated and labeled **C1** (FTO/TiO_2 – Pt/FTO); **C2** (Gr/TiO_2 – Pt/FTO); **C3** (FTO/TiO_2 – Pt/Gr) and **C4** (Gr/TiO_2 – Pt/Gr).

3.5 Optical Characterization

3.5.1 UV-Vis Spectroscopy

The TiO_2 on graphene/FTO composite thin films were optically characterized using a Shimadzu-DUV spectrophotometer. Prior to the measurement, a baseline was recorded on the spectrophotometer to calibrate the instrument. The thin films' spectroscopic transmission was measured at normal incidence and at wavelengths ranging from 200 nm to 1100 nm. The light beam divides into two paths, one of which passes through the sample cuvette and the other for comparison through the set reference cuvette.

Spectra can be automatically recorded owing to the monochromator. The operational structure of the UV-Vis spectrophotometer is schematically represented in figure 3.5.

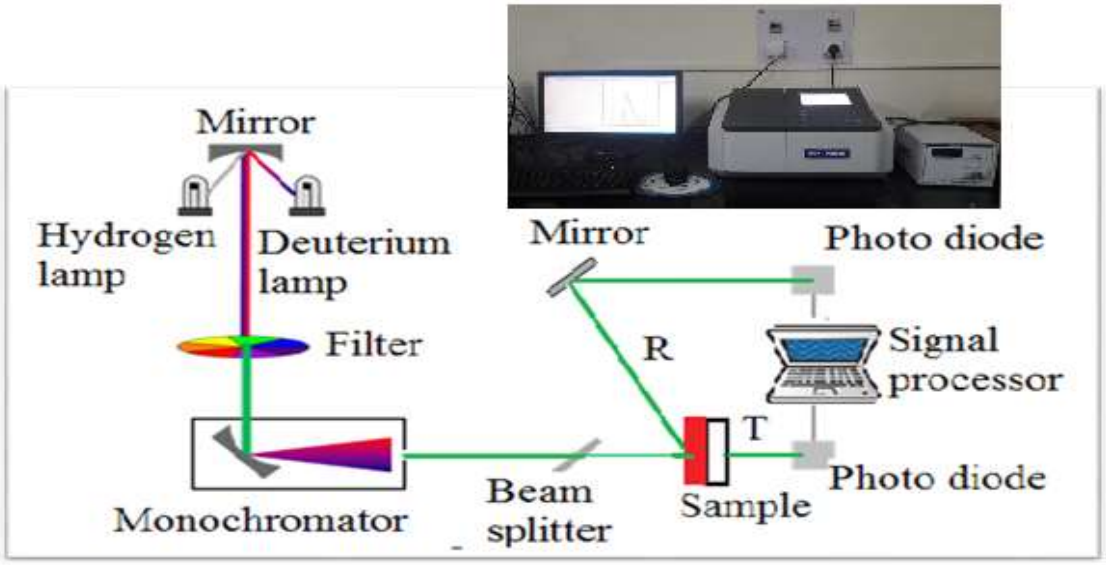

Figure 3.5: Schematic Representation of the UV-Vis Spectrophotometer's Operational Structure. Inset is a Shimadzu UV-1800 Spectrophotometer

The chopper switch between the samples, blank, and shutter manipulates the source beam path. While the mirror reflects the radiation back to the blank, the transparent window allows the radiation to reach the sample. Using the chopper rotation speed to continuously adjust its transmittance, the signal processor resolves the beam reaching the detector into the transmission of the blank, *IO*, and the sample, *IT*. Optical band gap energy, (E_g) was obtained using Tauc relation (equation 2.21) whereas the following optical parameters such as, refractive index (n), was obtained using OJL model in Scout software (section 2.9). Drude model in Scout software extracted the extinction coefficient ($_k$) dielectric constant (ε), and absorption coefficient (α). Obtained reflective indices determined porosity (P) and dispersion energy (E_d) as discussed in chapter 2.

3.5.2 FTIR Analysis

By employing Fourier Transform Infrared Spectroscopy (FT-IR), the effects of minute amounts of tin and carbon dopants on the composition of TiO_2/FTO and TIO_2/graphene were investigated. As deposited and annealed samples were used in FTIR imaging. Using a high reflectivity mirror as a reference and a specular reflectance stage with an incidence angle of 15° off normal, all FT-IR measurements were performed with a Varian 7000e FT-IR. In order to minimize LO-TO splitting, the lowest limit of the specular reflectance mounting, which was 15°, offered the closest incidence to normal. The correct setup of the source, detectors, and beam splitters was used to measure the spectra in the dry air range of 400–4000 cm^{-1}. The measured interferogram signal cannot be directly interpreted therefore the analyst needs a frequency spectrum (a plot of the intensity at each individual frequency) in order to make an identification. One needs a way to "decode" each of the individual frequencies. The Fourier transformation, a well-known mathematical method (equation 2.37), can be used to achieve this. The computer performs this transformation and then displays the required spectral information for analysis to the user as illustrated in figure 3.6.

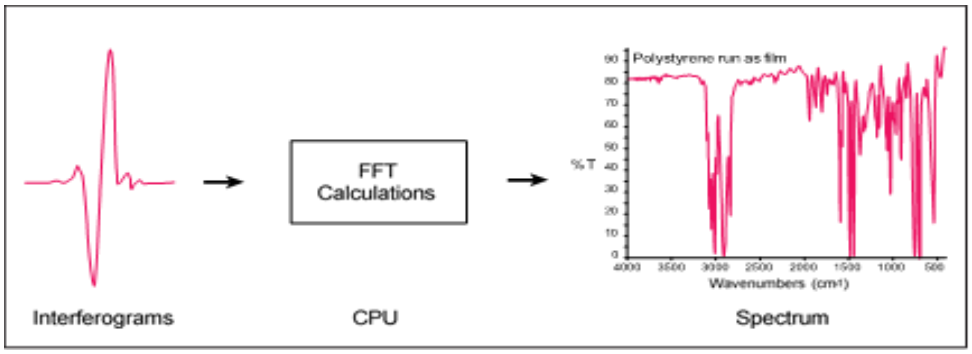

Figure 3.6: An Illustration of the Processes Involved in Interferogram Fourier Transformation and the Plotting of Intensity at Each Individual Frequency

3.6 Electrical Characterization

Electrical and surface charge characterization of the films were examined using Hall Effect equipment and the Kelvin Probe System (KP- Technologies Kelvin Probe System). A photoelectrode's electrical properties indicate the suitability of a film for

facilitating electron injection into and transport through the photoelectrode. The application of the Hall effect and four-point probe techniques is described in detail below.

3.6.1 Surface Potential Mapping and Charge Transport Characterization

Contact potential difference (V_{CPD}) between conductive tip and sample tip were measured using Scanning Kelvin Probe Microscopy (*SKPM*), which is an electric force microscopy (Maragliano *et al*., 2013). The V_{CPD} is defined by equation 2.37. Variations in contact potential V_{cpd} were measured in line, point, and area scans using a SKPM with a gold tip of $\phi = 5.2\ eV$ (5200 mV). The SKPM measurements were performed in noncontact mode using a cantilever with a gold-coated tip. The SKPM physical principle is mainly based on contact potentials (Simon & Jun, 2012). The applied bias to the tip had alternating and direct current components that were far less than the mechanical resonance frequency (ω_r) 170 kHz of the cantilever. The samples were set up on a moveable stage inside the Kelvin Probe system, and as seen in figure 3.7, a *PC* interfaced with the KP- Technologies Kelvin Probe System allowed the gold tip to scan over the surface charge distribution, observing surface potential V_{cpd} data.

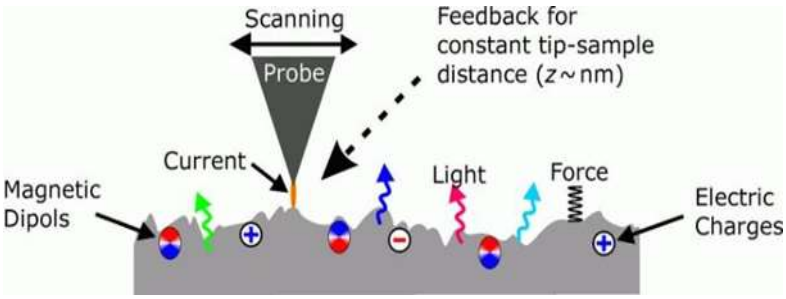

Figure 3.7: Representation of the Scanning Probe Microscope Probe and the Sample Surface, as well as Qualitative Force Behavior between Tip and Sample as a Function of Tip-Sample Distance

This work uses the KP-Technologies Kelvin Probe System to extract the frequency component (ω) of the gold tip deflection. $F_{\omega,}$ the electrostatic force, is proportional to the frequency component extracted. The lateral distribution of V_{CPD} from the electrostatic tip – surface force corresponds to the distribution of local work function (Simon & Jun, 2012). The contact potential difference is the surface potential

difference (*SPD*) and gives information about surface charge distribution (Simon & Jun, 2012; Zeweck *et al*., 2005).

From Hall coefficient (*RH*) data, the type of charge carriers, concentration (n_H), Hall mobility (μ_H), drift velocity (V_d), lifetime, mean free path (l) of charge carriers and conductivity were calculated. The configuration depicted in figure 3.8 measured the Hall voltage perpendicular to both the direction of an electric current flowing through the semiconductor and the magnetic field. Figure 3.8 illustrates the digital flux/gauss meter to measure the uniform magnetic field intensity. Every sample was put separately onto a printed circuit, clamped, and fastened to a stand that was positioned in the space between two electromagnetic poles. At room temperature (25 °C), the Hall voltage and current values were measured and recorded for a magnetic field of 3G (=0.0003 T).

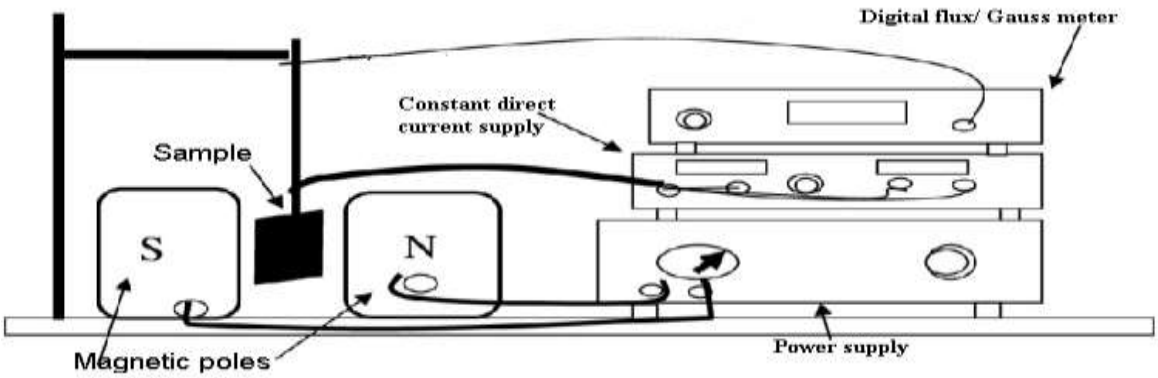

Figure 3.8: Diagrammatic Representation of the Hall Effect Measurement Accessible at Chuka University Laboratory

3.7 Photocurrent Density-Voltage (J-V) Characteristics

An electrochemical analyzer (Keithley 2420 SourceMeter) was used to measure the *J-V* characteristics of DSSCs with different electrodes under simulated sunlight (ABET Technologies Sun 2000 Solar Simulator, 100 mW cm^{-2}, *AM* 1.5 spectrum). A solar simulator was used to provide the simulated light. It uses light from a xenon ultra-high-pressure lamp passed through a variety of filters to closely mimic solar radiation. Using a Keithley meter and computer, the currents and voltages produced by the solar cell for various load resistances were measured under a set of standard test conditions

for solar cells (Jose *et al*., 2009). International standards, such as the ASTM E927-05 documents, describe these test conditions, as the temperature of 25°C, the power density of the light illuminating the cell equivalent to 100 mW cm^{-2}, and the radiation condition must be *AM* 1.5 global for terrestrial applications. The short-circuit current density (J_{SC}), open-circuit voltage (V_{OC}), fill-factor (*FF*), and energy conversion efficiency (η) were determined using the I-V curves and recorded.

CHAPTER FOUR

RESULTS AND DISCUSSIONS

4.1 Background

This chapter presents the experimental results and discussion of UV VIS optical spectrophotometry, Fourier Transform Infrared (*FTIR*) spectroscopy, Hall Effect measurements and *SKPM* measurements and their analysis. Additionally, models are developed and discussed that relate to the optical properties; Porosity, Dispersion parameters, Dielectric energy losses; surface morphology, contact potential difference (V_{CPD}), and electron transport of the TiO_2 on FTO and on graphene films were studied. This study analyses data acquired in the visible light spectrum, specifically at a wavelength of 550 nm, which corresponds to a photon energy of 2.26 eV. The report additionally includes data from specific peaks (fig 4.18) on the spectrum. Consequently, the I–V characteristics for TiO_2 on FTO and TiO_2 on graphene, as well as the working and counter electrodes of the fabricated DSSCs, were analyzed and discussed.

4.2 Optical Spectroscopy of TiO_2 on FTO

4.2.1 Reflectance

Figure 4.1 shows the reflectance versus wavelength spectra of as-deposited and differently annealed TiO_2 on FTO films. Reflectance drops from 50% to around 20% at visible wavelengths (400 nm - 700 nm). TiO_2 on FTO thin films, both as deposited and annealed, reflectance ranges from 20 to 30% at 550 nm, indicating that TiO_2 films can be employed as antireflection coatings for photovoltaics. The film with the lowest reflectivity is the one with the lowest annealing rate (1 °C/min), whereas the film with 1 step annealing rate, has the highest reflectance. This is due to variance in film thickness with the 1 step being more thicker leading to increased light absorption. Absorption edge was found between 400 nm to 540 nm while plateau was noticed from 660 nm to 900 nm demonstrating constant refractive index. Reflectance at 550 nm was observed to vary with annealing rates, 1 ^{o}C/min exhibiting the least reflectance

attributed to improved crystallinity associated with reduction in lattice defects and enhanced homogeneity from annealing.

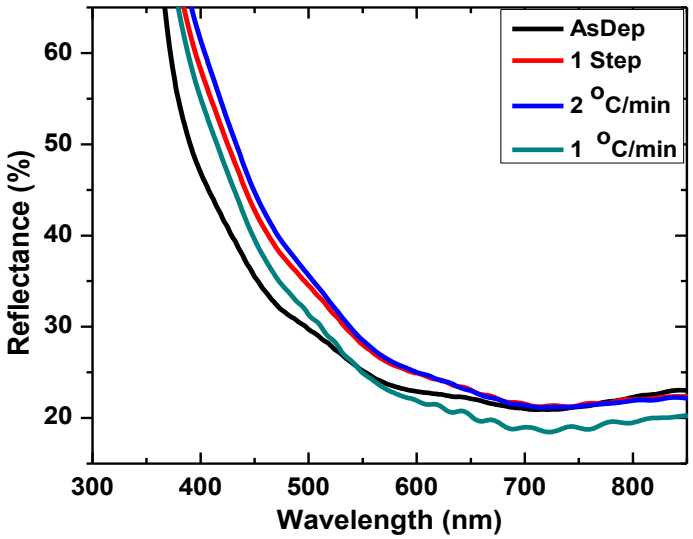

Figure 4.1: A Graph of Reflectance versus Wavelength for as Deposited, 2 ºC/min, 1 ºC/min and 1 Step Films

According to Ayieko *et al*., (2003), a decrease in crystallite sizes causes an increase in reflectance at higher annealing temperatures, increasing the particle's surface area and ability to scatter light. The lower reflectance has been associated with a higher crystallinity and a higher thermal conductivity (Xinmi *et al*., 2017).

4.2.2 Refractive Index

As exhibited in figure 4.2, the refractive index of annealed TiO_2 on FTO films ranging from 300 nm to 900 nm fluctuated with wavelength, λ. The refractive index spectra were found to diminish and exhibit notable variations toward low photon energy, a characteristic of normal dispersion behavior. Refractive index increased towards low annealing rate suggesting that 1 ºC/min film having the highest value becomes less optically dense. The refractive index reduced significantly in the UV region and moderately in the visible region due to the reduction in absorption coefficient with wavelength, confirming normal dispersion behavior.

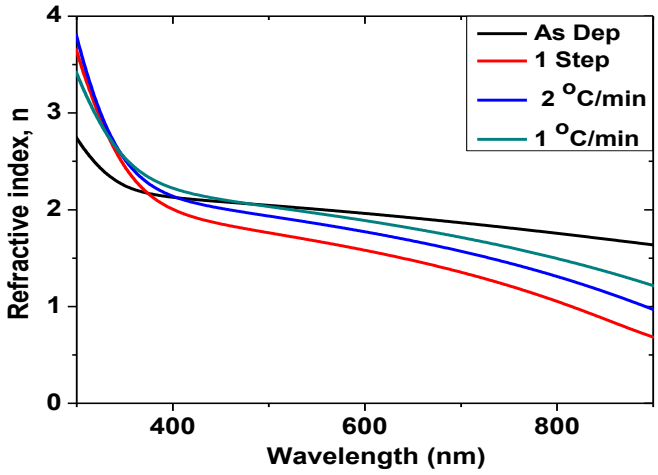

Figure 4.2: A Graph of Refractive Index versus Wavelength of as Deposited and Annealed TiO_2 on SnO_2: F (FTO)

The average visible range refractive index as a function of annealing rates is shown in figure 4.3. In the visible range (400–700 nm), the average refractive indices were 1.95, 1.56, 1.75, and 1.87 for as deposited, 1 step, 2 °C/min, and 1 °C/min, respectively.

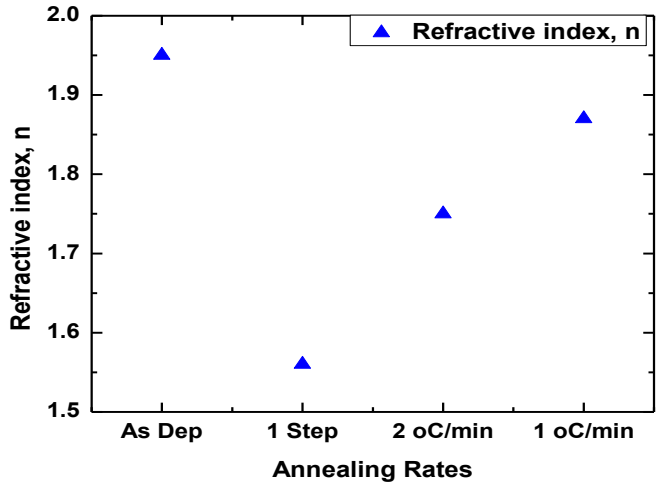

Figure 4.3: A Graph of Refractive Index for TiO_2 on FTO versus Annealing Rate

1 ^oC/min annealing rates has the highest refractive index value associated with a decrease of the band gap of the films. The resonance effect at higher wavelengths was associated to a reduction in refractive index. Due to the equivalence of the input photon

and plasma frequencies, this effect happens between electronic polarization and incident light photons on the sample (Hassanien & Akl, 2018). Refractive index is highest at 1 ^{o}C/min annealing rates which is associated with the enhancement of crystallinity and increased packing density of the film (Hassanien & Akl, 2018).

4.2.3 Porosity and Relative Density of Annealed TiO_2 on FTO Films

The porosity and relative density of the film were calculated using equations 2.19 and 2.20. Figure 4.4 shows how the porosity and relative density vary with annealing rate.1 step annealing rate reveals, the highest porosity (73 %) of the films while their relative density was lowest (27%).

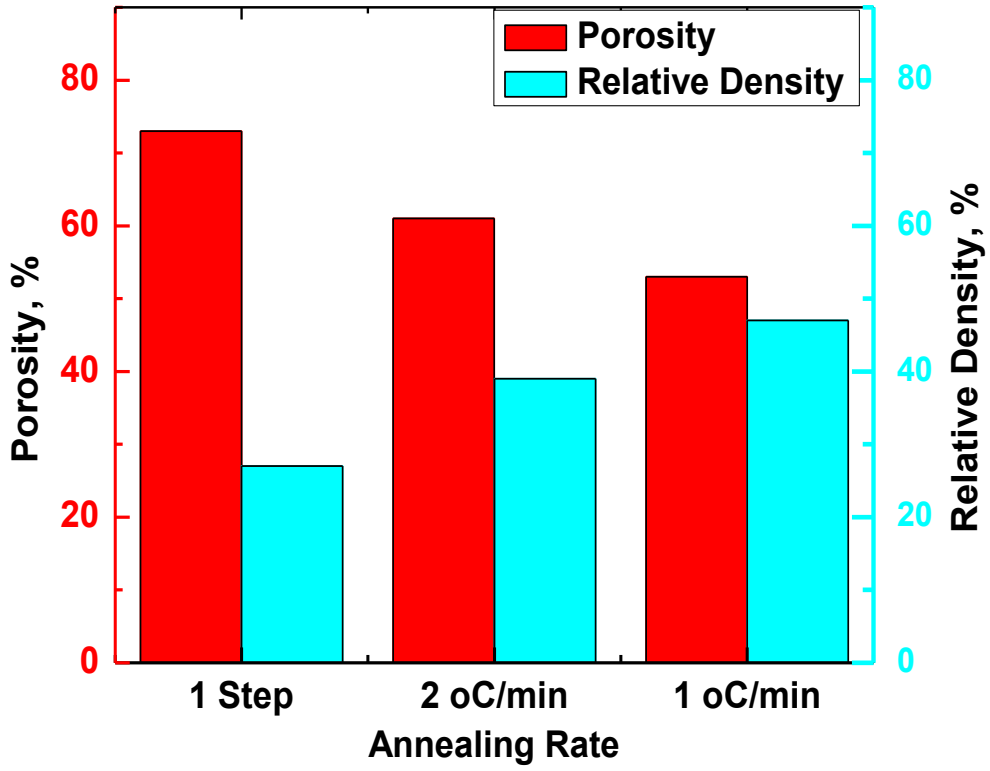

Figure 4.4: Variation of Porosity and Relative Density with Decreasing Annealing Rates

TiO_2 films collapses some pores when annealed at lower annealing rate (1 ^{o}C/min) due to increasing particle sizes attributed to the decrease in porosity. Film pore filling and film densification cause decrease in porosity. The increase in relative density caused by annealing indicates that the quality of film crystallization continually increases The

XRD patterns of as-deposited and annealed TiO_2 films at different temperatures were investigated by Hasan *et al.* (2010). The annealed films' crystallization partially increased. The following sections describe the correlation between the porosity and the dispersion energy.

4.2.4 Refractive Index Dispersion Parameters

Equation 2.26, which indicates a single oscillator model based on the Wemple-DiDomenico model, was used to calculate the functional relationship for refractive index dispersion. Figure 4.5 shows the $(n^2-1)^{-1}$ spectra against $(h\nu)^2$ for TiO_2 films before and after annealing.

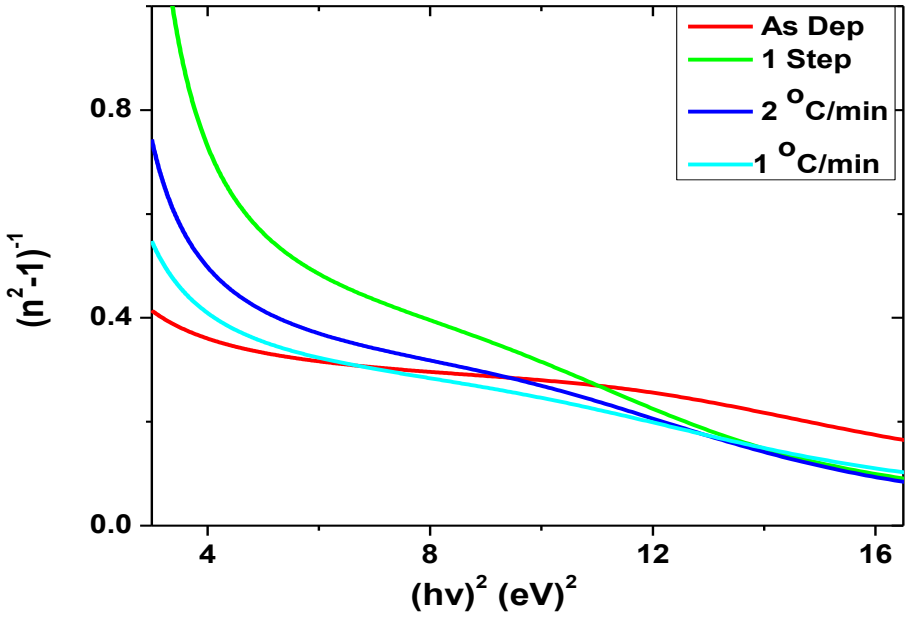

Figure 4.5: Plots of $(n^2-1)^{-1}$versus $(hv)^2$ of as Deposited and Annealed TiO_2 Coatings on FTO

As photon energy increases, the values of $(n^2-1)^{-1}$ decrease in all films due to lattice absorption. Figure 4.6 shows the oscillator energy, E_o, and dispersion energy, E_d, calculated by fitting a straight line to the spectra of $(n^2-1)^{-1}$ vs $(h\nu)^2$ from 6.6 to 8.4 $(eV)^2$ within the visible range.

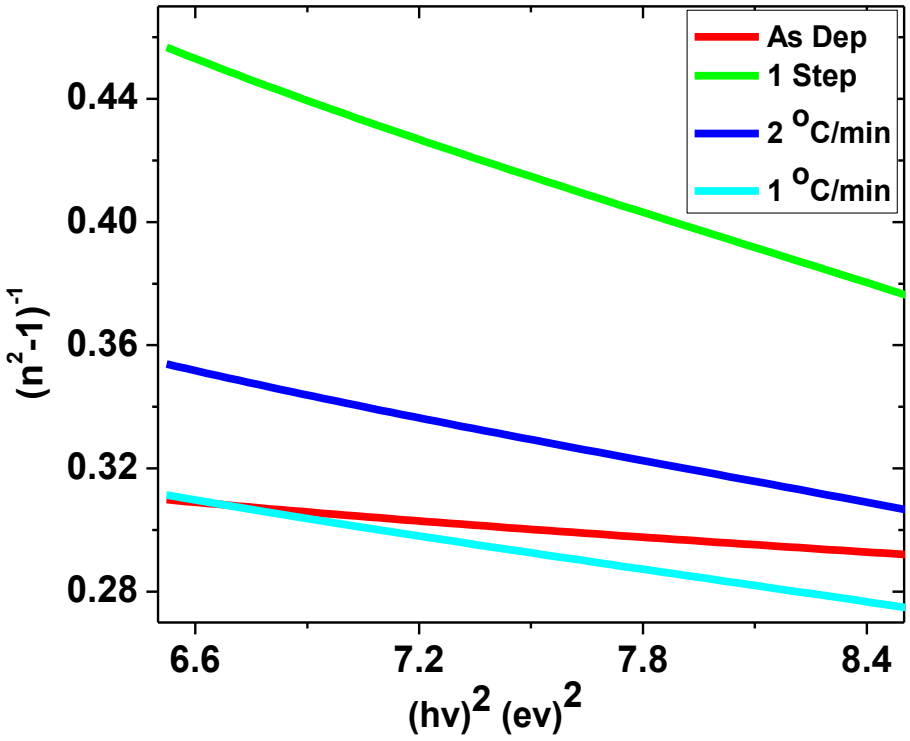

Figure 4.6: Linear Fit of $(n^2-1)^{-1}$ versus $(hv)^2$ of as Deposited and Annealed TiO_2 Coatings

E_o/E_d is the estimated value of the linear fit for normal dispersion behavior intercepting $(n^2-1)^{-1}$ (vertical axis), with a slope equal to $(E_oE_d)^{-1}$. The oscillator energy E_o and dispersion energy E_d for film annealed at 1 °C/min were 4.85 eV and 11.30 eV, respectively. The coupling strength of a material excitation with an electromagnetic field is determined by oscillator strength using equation 2.25. 1 °C/min had the highest oscillator strength associated with high probability of an electric dipole transition as electrons in the valence band are excited to the conduction band. Table 4.1 contains the results for refractive index, relative density, porosity, dispersion and average excitation energy, moment of the optical transitions and oscillator strength at 550 nm wavelength (2.26 eV). Ionic or covalent materials' crystalline structure and ionicity are related to the oscillator energy and dispersion energy values.

Table 4.1: Optical Parameters and Dispersions of TiO_2 Thin Films at Various Annealing Rates

Samples	Refractive index, n	Relative density (%)	Porosity (%)	E_d	E_0	M_{-1}	M_{-3}	$f = \frac{E_d}{E_0}$
As- Dep	1.95	52	48	17.46	6.41	2.72	0.42	111.9
1 Step	1.56	27	73	5.90	4.23	1.39	0.33	24.96
2°C/min	1.75	39	61	9.15	4.64	1.97	0.42	42.46
1°C/min	1.87	47	53	11.30	4.85	2.33	0.48	54.81

The moment of the optical transitions M^{-1} and M^{-3}, calculated using equation 2.26 and the values in table 4.1, is determined by E_o and E_d. As the annealing rate reduced, M^{-1} and M^{-3} increased, with 1 ^oC/min producing the highest values. Previous research has linked the influence of lattice absorption and an increase in scattering centers to an increase in E_o and E_d as a result of an increase in annealing temperature (Wemple & DiDominico, 1971). The surface energy loss and volume energy loss covered in the next section have been correlated with porosity and dispersion energy.

4.2.5 Dielectric Characterizations of TiO_2/FTO

The real part (ε_1) and imaginary part (ε_2) of the dielectric function were obtained using scout software as in equation 2.31 and 2.32 from transmittance data. The ε_1 and ε_2 represent the amount of energy stored in dielectrics as polarization and loss energy respectively. The power loss factor (tan δ) associated with the electric behavior of the film is described by equation 2.33. Equations 2.35 and 2.36, respectively, determine the inelastic scattering of electrons in solid film caused by energy loss functions, commonly referred to as volume loss function and surface loss function. The variation of tan δ vs photon energy for the annealed TiO_2 films is depicted in figure 4.7(a). In the lower light energy (or low frequency) area (up to 2.0 eV), the films' tan δ gradually drops as annealing rates diminish. For photon energies more than 2.5 eV (i.e particularly in the high frequency range), the loss tangent increases significantly with photon energy. The variances in the loss tangent indicate that annealing has a significant impact. Tan δ exhibits a similar pattern, with the film's loss tangent being less than 1, indicating negligible energy loss. This shows that annealed films have good optical properties due to decreased energy losses and incoming radiation scattering

(Yang *et al.*, 2008). Figure 4.7 (b) and (c) illustrate the surface energy loss, *SELF*, and volume energy loss, *VELF* functions of TiO_2 films after annealing at different rates.

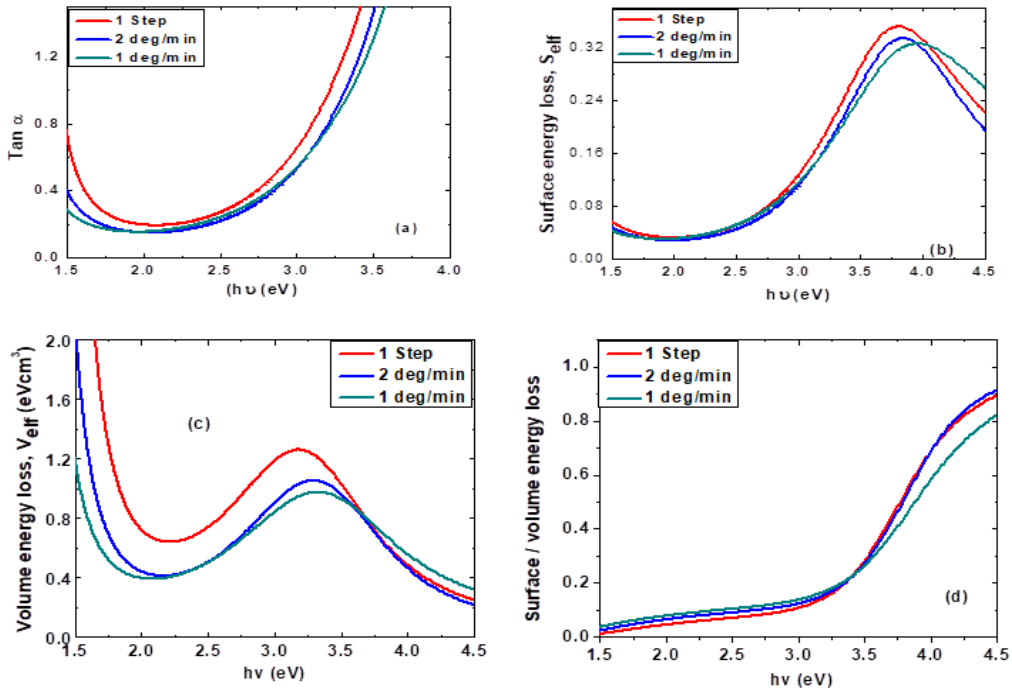

Figure 4.7: (a) Loss Tangent, (b) Surface Energy Loss, (c) Volume Energy Loss, and (d) Surface / Volume Energy Loss as a Function of Photon Energy (hν)

Surface energy loss values obtained from the spectra peaks for 1 step, 2 °C/min, and 1 °C/min, were 0.351, 0.333, and 0.326 $eVcm^2$ respectively. On the other hand, volume energy loss obtained from the peaks were 1.262, 1.06, and 0.962 $eVcm^2$ for 1 step, 2 ^oC/min and 1 ^oC/min annealing rates in that order. For all incident photon energies and annealing conditions, the volume energy (*VELF*) function is substantially higher than the surface energy functions (*SELF*). According to previous research, the loss of energy of a free charge traveling through the surface of a film is less than that of a free charge traveling through the volume (Yang *et al.*, 2008; Yakuphanogu *et al.*, 2004; and Sarkar *et al.*, 2014).

According to Sarkar *et al.*, (2014), energy loss occurs when a fast-moving electron passes through a medium as a result of stimulating conducting electron plasma oscillations. Regular grain boundaries lead to negligible energy dissipation, therefore

films annealed at 1°C/min lose the least amount of energy. Figure 4.7(d) depicts the surface energy loss to volume energy loss ratio in comparison to photonic energy. Up to 3.5 eV, the ratio of surface to volume energy loss increases as the annealing rate lowers, albeit with little fluctuation. For photon energy greater than 3.5 eV 1 ^{o}C/min has the least *SELF*. It is noted that surface energy loss fails to reflect the inelastic scattering with finite momentum transferred at the surface and is insensitive to surface structure at low photon energy (El-Nahass *et al*., 2016). The TiO_2 film annealed at 1 ^{o}C/min is associated with enhanced electron transition attributed to the significant contribution of virtual electronic, which results in a significant shift in optical properties.

Figure 4.8 depicts the relationship between surface to volume energy loss and porosity. The film with the largest porosity is the one annealed at the highest rate (1 Step). However, it was noted that porosity with 1 ^{o}C/min annealing rate attained the least. The low porosity at 1 ^{o}C/min is attributed to film pore filling and film densification due to crystal enhancement of the films with annealing. Surface/volume energy losses vary with 1 ^{o}C/min revealing high value as shown in figure 4.8.

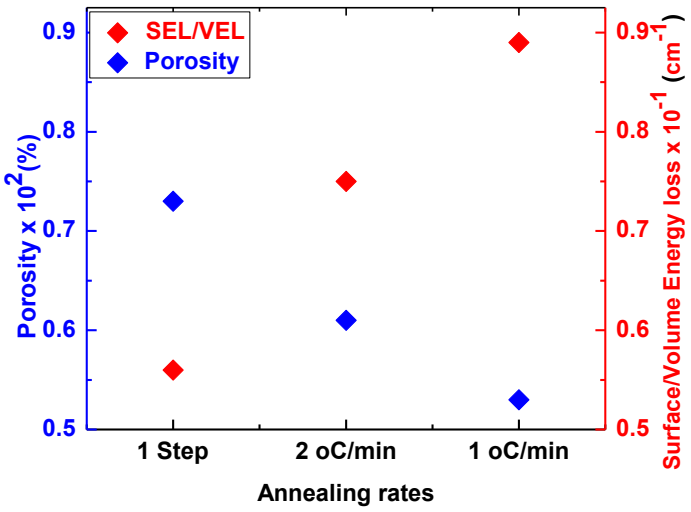

Figure 4.8: Plots of Porosity and Surface/Volume Energy Loss of Annealed TiO_2 on FTO Films

It has been reported that annealing temperature and annealing time has an effect on surface quality porosity and aggregate of the films (Al-Jufairi, 2006). The surface of TiO_2 showed clustered particles through SEM and the shrinkage rate increased as result of heat treatment (Al-Jufairi, 2006). Decrease in *SELF* and *VELF* values of 2 ^oC/min annealing rate to 1 ^oC/min is associated with the crystalline structure and ionicity of ionic or covalent materials (Wemple and DiDominico, 1971). This basically means that the single oscillator model can be effectively used to ascertain the structural characteristics of these films in addition to their optical characterizations. According to earlier reports, increasing the film's crystallinity can raise the free-electron density while lowering the degree of electron transitions. The frequency dependence of the complex electronic dielectric constant was used to deduce the thin film's fundamental electron excitation spectrum (Fournier *et al.*, 2008; Zhiwen *et al.,* 2015). Therefore, we associate the increase in *SELF/VELF* to improvement in crystalline quality of the TiO_2 films. The surface-to-volume ratio follows the same trend as dispersion energy. The optical characterization of TiO_2 layers on graphene is described in the following section.

4.3 Optical Characterization of TiO_2 on Graphene Thin Films

4.3.1 Transmittance

The transmittance spectra of the TiO_2 on graphene composite and annealed graphene samples are displayed in figure 4.9, covering the wavelength range of 300 to 800 nm. Variations were displayed in the optical transmittance spectra of the thermally treated films. A substantial drop in transmittance at the absorption edge, or UV area was noted.

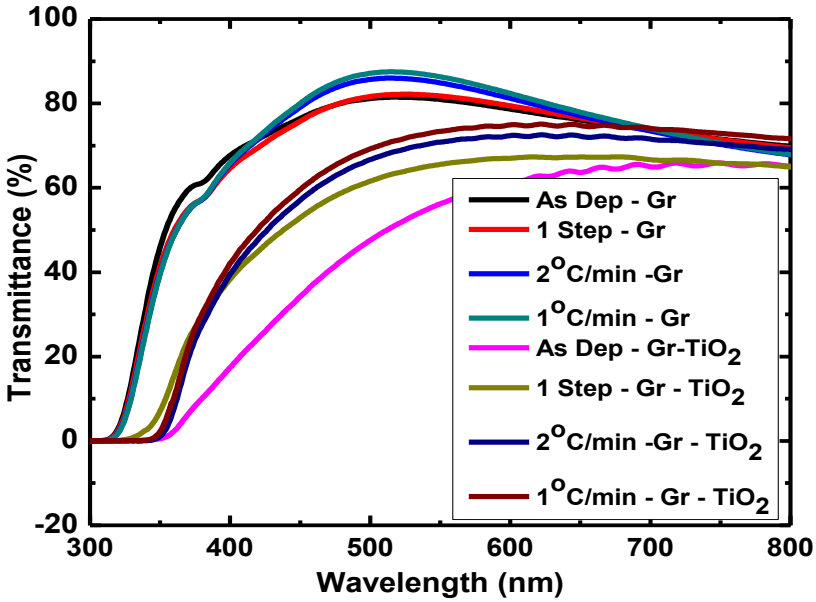

Figure 4.9: A Graph of Transmittance versus Wavelength of Graphene and TiO_2 on Graphene Thin Films for Different Annealing Rates

As seen in figure 4.9, maximum transmittance of 86.57% and 74.07% for graphene and TiO_2 on graphene, respectively, at a wavelength of 550 nm was observed at an annealing rate of 1 ^oC per minute. TiO_2 on graphene was discovered to be at a wavelength of 713.5 nm for as-deposited and annealed films, whereas graphene films exhibit peaks at 500 nm. Every film had a high visible spectrum transmittance. The transmittance of graphene and TiO_2 on graphene films exhibited a discernible blue shift in the direction of 1 ^oC/min annealing rate. Annealing modifies the optoelectronic characteristics of graphene monolayer despite it having zero band gap. We report variations on graphene's transmittance at different annealing rates due to polymer residue, elimination of hydrocarbons and modification of graphene coatings as a result of intrinsic free-standing graphene, substrate or environmental effects. Increased surface roughness or the elimination of oxygen defects are the two possible causes of the slight transmittance drop seen with increasing annealing rates for both graphene and TiO_2 on graphene films (Gupta & ManSingh, 1996). Oxygen vacancies arise because of oxygen being released into the environment during lower annealing rates for TiO_2. Table 4.2 shows record of peaks for transmittance values obtained from figure 4.9 within the transparent zone corresponding to λ=550 nm.

4.3.2 Refractive Index Parameters of TiO_2 on Graphene Thin Films

The refractive index values of graphene and TiO_2 on graphene films were calculated using equation 2.18. Plots of graphene and TiO_2 on the refractive index (n) of graphene films as a function of wavelength for both as-deposited and annealed films at varying annealing rates are displayed in figure 4.10.

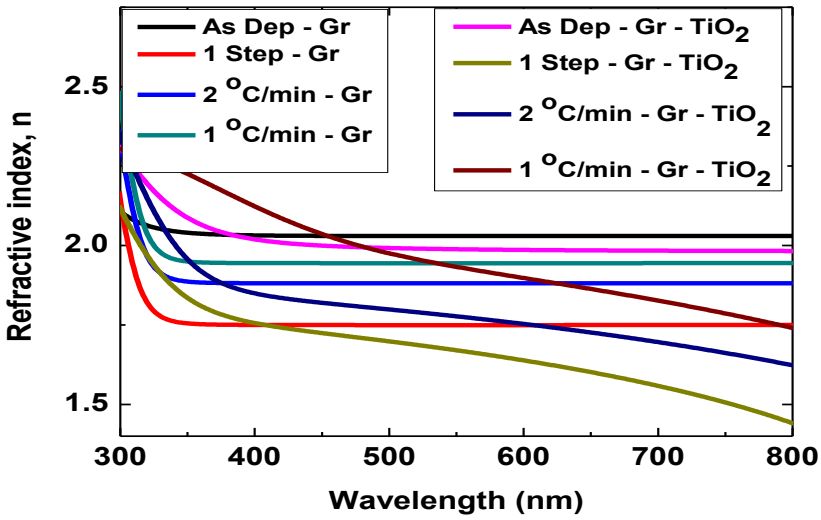

Figure 4.10: A Graph of Refractive Index versus Wavelength of Graphene and TiO_2 on Graphene for as Deposited Films and Films Annealed at Different Rates

As wavelength increases, the refractive index spectra decrease, displaying a typical dispersion characteristic. Refractive index, however, changes as annealing rates vary due to the modification of compactness, internal stress release, crystallization and densification of the films. Refractive index spectra for graphene and TiO_2 on graphene films rise towards low annealing rate, which is associated to improved crystallinity and increased packing density (Hassanien and Akl, 2018). The decrease in refractive index with wavelength can be related to the resonant effect, which occurs between irradiation photons and electronic polarization because of the equality between irradiated photons and plasma frequency (Hassanien & Akl, 2018). The refractive index of TiO_2 on graphene at λ=550 nm is shown in Table 4.2. In TiO_2 films, the refractive index of the film affects porosity, which is the number of pores per volume. The equation 2.19 estimates porosity expressed as a percentage. Refractive index at

λ=550 nm within the transparent zone, determined porosity. The phenomena of low porosity of 1 ^{o}C/min annealing rate are attributed to a decrease in pore size because of compaction and densification of the film. Lowest porosity was therefore associated with a high refractive index. 1 ^{o}C/min film exhibited the lowest porosity, (46%). Porosity decreased with 1 ^{o}C/min annealing rate having the least value) due to a massive rise in the overlap of TiO_2 densely packed particles. At low porosity, particle overlap causes the material's interior surface area to rise. TiO_2's coordination number (*CN*) rose with decreasing porosity. Porosity for maximally *CN* = 6 densely packed particles was determined to be 0.41 (41%) (Liu *et al*., 2002; Saito *et al.*, 2004).

Table 4.2: Transmittance and Optical Parameters of TiO_2 on Graphene Thin Films at Various Annealing Rates

Samples	Transmittance (%)	Refractive index, n	Relative density (%)	Porosity (%)
As-Dep	55.71	1.99	55.82	44.18
1 Step	65.47	1.67	30.68	69.32
2°C/min	70.55	1.78	42.81	57.19
1°C/min	74.07	1.90	53.88	46.12

The relative density values of the films were calculated using equation 2.20 (Ohyama *et al*., 1997). A graph of relative density against photon energy is shown in figure 4.11. The relative density of the annealed sheets was found to rise with photon energy.

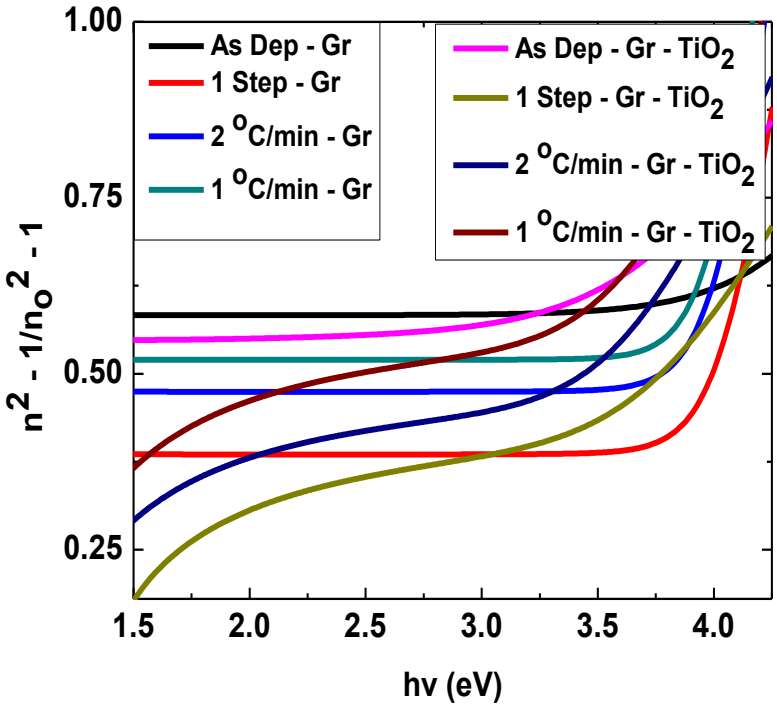

Figure 4.11: A Graph of Relative Density versus Photon Energy (hν) for as Deposited and Annealed Graphene and TiO_2 on Graphene Films

The steady improvement of film quality, densification, and crystallization is associated with the increase in relative density implying that 1 ^oC/min annealing rate is denser and more crystalline than the other films. In a solid-state lattice site, charge transport is a phenomenon that resembles hopping and causes electron recombination. Because of improved light absorption, pore filing, and charge compensation brought about by a decrease in porosity, compact and dense TiO_2 electron transmission improves (Smestad *et al*., 2003).

4.3.3 Dispersion Parameters of TiO_2 on Graphene Thin Films

Wemple DiDominico (WDD) single oscillator model investigates the refractive index dispersion in the low absorption location (Wemple & DiDomenico, 1969; Wemple & DiDomenico, 1971). Equation 2.24 was used to calculate the bandgap of the single oscillator Eg ^{WDD}, the average excitation energy (E_o), and the dispersion energy (E_d). Figure 4.12 depicts the spectra of $(n^2\text{-}1)^{-1}$ as a function of $(h\nu)^2$ for graphene and TiO_2

on graphene films, both deposited and annealed. As photon energy increases, $(n^2-1)^{-1}$ decreases.

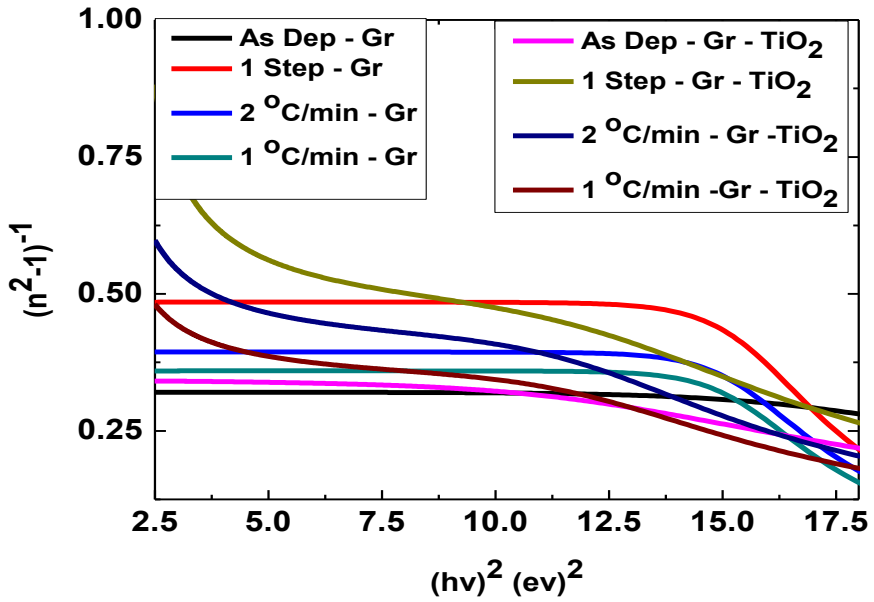

Figure 4.12: Plot of $(n^2-1)^{-1}$versus $(hv)^2$ of as Deposited and Annealed Graphene and TiO_2 on Graphene Coatings

Because of impurities and structural defects in the intercrystallites boundaries, which result in increased scattering centers in the films, $(n^2-1)^{-1}$ disperses at lower energies and clusters together as we approach higher photon energy for all of the films (Wemple & DiDomenico, 1971).

Straight lines fitted between 3.5 and 6.5 $(eV)^2$, selected from the observed curvature of TiO_2 on graphene samples, are displayed in figure 4.13 as a result of fitting linear in figure 4.11. According to Wemple & DiDomenico (1971), lattice vibrations negatively affect the refractive index, which explains why a positive curvature deviation is seen linearly at long wavelengths. Graphene did not produce significant values at this range since graphene spectra were horizontal.

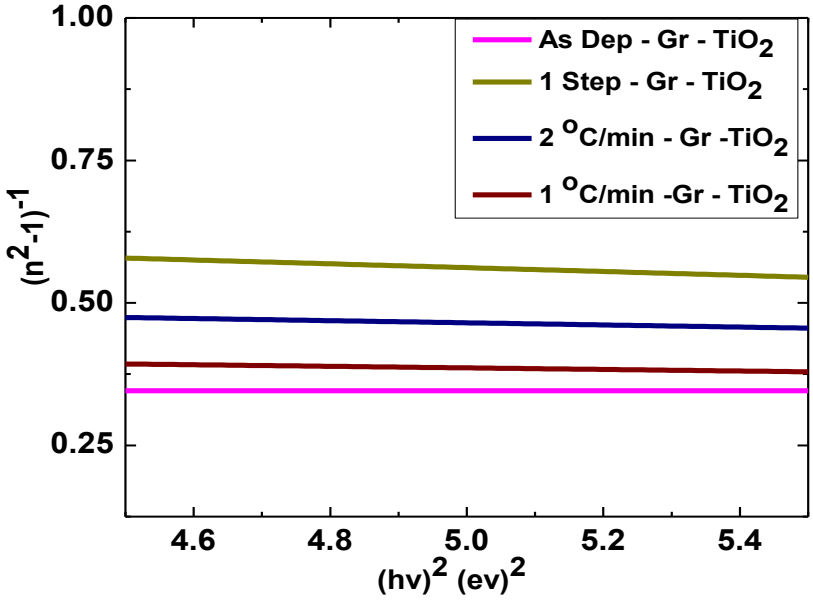

Figure 4.13: Linear Fit of $(n^2-1)^{-1}$ versus $(hv)^2$ of as Deposited and Annealed TiO_2 on Graphene Coatings

Equation 2.24 for normal dispersion behavior showed that the slope created $(E_oE_d)^{-1}$, whilst the vertical intercepts produced E_o/E_d, enabling the oscillator energy (E_o) and the dispersion energy (E_d) to be determined. The E_o and E_d values were calculated for both as deposited and annealed films. According to table 4.3, dispersion energy and oscillator energy rise, with 1 °C/min exhibiting the greatest value. This is because the film is anticipated to have greater strength in interband optical transition and higher excitation energy for electronic transition. Graphene monolayers with a high specific surface area and numerous chemical flaws have a high dispersion (Skrypnychuk *et al.*, 2020). When graphene scaffolder TiO_2, it results in high dispersion and may improve dye adsorption for DSSC applications. Dispersion energy, E_d, can be related to the coordination number (CN) using the equation 2.28 (Tan *et al.*, 2006; Marquez *et al.*, 1995). TiO_2 has a formal valence of anion Za of 2 and an effective number of valence electrons per anion N_e of 8. Particle coordination numbers computed using equation 2.28 found in section 2.6.3 are listed table 4.3. These values CN values increase with a film annealed at 1 °C/min resulting in a larger particle coordination number, which is related to improvements in percolation routes. A greater particle coordination

number for an electron sitting on a certain particle indicates that it has enough feasible avenues to percolate in a three-dimensional lattice to another particle.

According to Wagner *et al*. (2007), Miller rule computed the linear optical susceptibility χ^1 and the nonlinear polarizability parameter, also known as nonlinear optical susceptibility χ^3, which is highly convenient for visible and near infra-red wavelengths. Figure 4.14 depicts the photon energy-dependent nonlinear optical susceptibility of annealed TiO_2 on graphene.

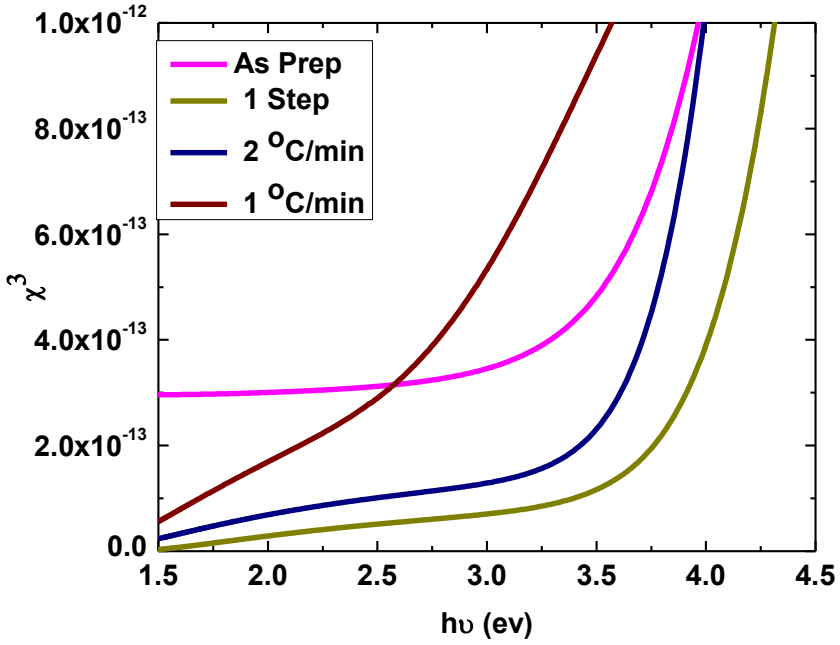

Figure 4.14: A Graph of Nonlinear Optical Susceptibility(χ^3), against Photon Energy (hv) for as Deposited and Annealed TiO_2 on Graphene

It is evident that as photon energy increases, so does the χ^3 spectrums for all samples. The quantum confinement effect was responsible for the enhancement of both linear and nonlinear optical susceptibility with a drop in annealing (Zeng *et al.*, 2003). Equation 2.29 was employed to calculate the appropriate χ^1 and χ^3 values at a corresponding hv = 2.26 eV. Table 4.3 presents the recorded values. Due to the probable presence of C-O-Ti bonds associated to effective charge separation, the film annealed at a rate of 1 ^oC/min exhibited a significantly higher nonlinear optical

susceptibility, which is related to increased crystallinity of TiO_2 on graphene (Hassaniena *et al.*, 2020).

4.3.4 Complex Dielectric Analysis of TiO_2 on Graphene Thin Films

4.3.4.1 Real and Imaginary Dielectric Parameters of TiO_2 on Graphene

The dielectric function,$\varepsilon = \varepsilon_1 + \varepsilon_2$, generates both the real $\mathcal{E}_1$ and imaginary $\mathcal{E}_2$ components of the dielectric constant, which are apparent in equations 2.31 and 2.32. Figure 4.15 presents the fluctuation of real and imaginary parts as a function of wavelength for all graphene on TiO_2 films (as deposited and annealed). $\mathcal{E}_1$ is significantly greater than $\mathcal{E}_2$, where $\mathcal{E}_1$ represents the slowing of light in the medium and $\mathcal{E}_2$ indicates an interaction of matter with an electric field vector, culminating in light absorption.

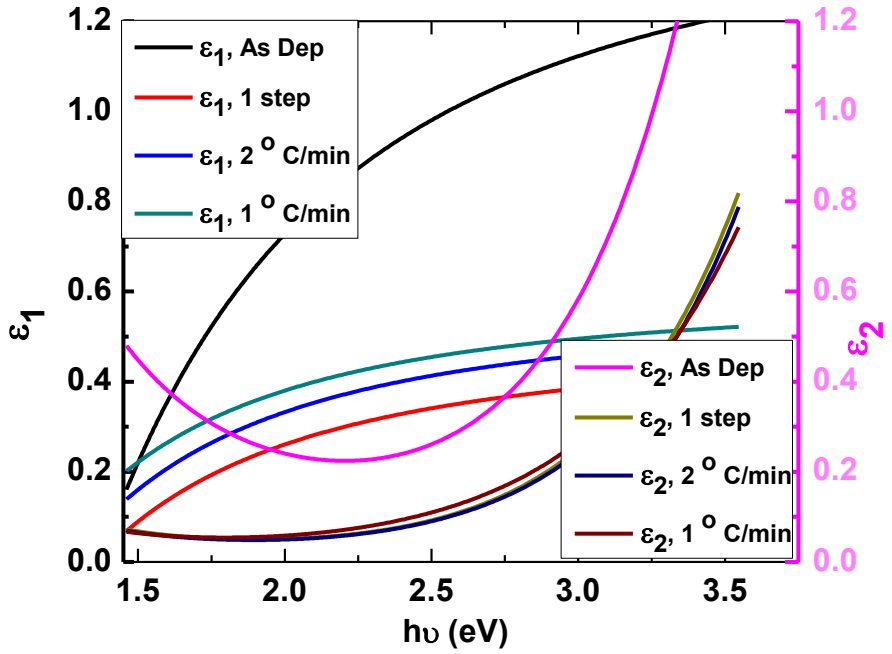

Figure 4.15: A Variation of Real (ε_1) and Imaginary (ε_2) Parts of Complex Dielectric Constant for as Deposited and Annealed TiO_2 on Graphene

$\mathcal{E}_1$ and $\mathcal{E}_2$ rise as photon energy increases. As annealing rates dropped from 2 ^oC/min to 1 ^oC/min, the real and imaginary components of the dielectric constant improved, which is explained by the crystalline enhancement of the TiO_2 films. Table 4.3 shows

the values for $\mathcal{E}_1$ and $\mathcal{E}_2$ obtained at hυ equal to 2.26 eV. According to Chander & Dhaka (2016), variation seen in the real and imaginary parts suggests some interaction between photons and electrons produced in that region.

The ratio of the real to imaginary parts of the dielectric constant is exceeding one, indicating that TiO_2 on graphene films responds to incident radiation on their surface in a distinct and identifiable manner. According to Astinchap *et al*., (2017), the relation 2.33 gives the loss tangent, which provides information about the loss factor. Tan δ values in table 4.3 are less than one for all films, indicating that the films dissipation energy is quite low. The lower the loss tangent of the films, the better the optical properties due to low scattering of irradiation photons (Yang *et al*., 2008).

Table 4.3: Dispersions and Dielectric Parameters of TiO_2 on Graphene Thin Films at Various Annealing Rates

Samples	E_d	E_0	Nc	$\chi^3 \times 10^{-13}$	$\chi^1 \times 10^{-1}$	ε_1	ε_2	Tan δ
As-Dep	45.6	15.8	7.70	30.50	2,35	0.62	0.26	0.41
1 Step	6.38	4.66	1.08	4.12	1.42	0.28	0.03	0.10
2°C/min	9.77	5.46	1.65	8.70	1.72	0.36	0.13	0.38
1°C/min	12.7	5.76	2.15	22.50	2.18	0.48	0.32	0.68

4.3.4.2 Real and Imaginary Interband Transition of TiO_2 on Graphene

In equation 2.34, the real and imaginary components of the dielectric constant were combined to create a complex interband. The intensity of the dielectric transition is proportional to the part real interband transition J_{cv1} and the imaginary part interband transition J_{cv2} (Loughin *et al.*, 1996). Figure 4.16 (a) depicts the photon energy dependence of J_{cv1} and J_{cv2}. The strength of the interband transition increases with photon energy.

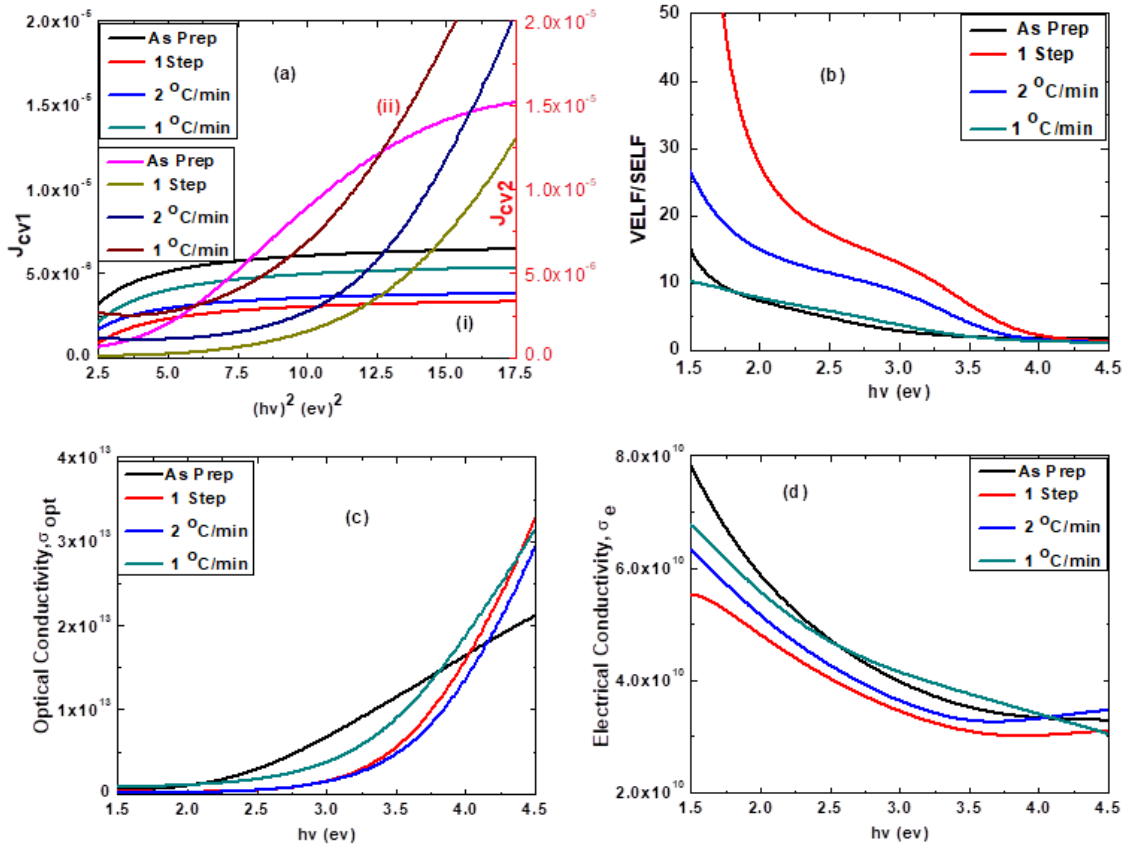

Figure 4.16: (a). Interband Transition (J_{cv}) versus (hν)^2, (b) VELF/SELF , (c) Optical Conductivity, and (d) Electrical Conductivity as a Function of Photon Energy (hν)

Jcv improves as annealing rates fall, which is associated with a rise in electronic transition probability. *Jcv* increases significantly when $(h\nu)^2 > 5.0\ (eV)^2$, implying that high absorption elevates electron excitation. This enables electrons to pass from the valence band to the conduction band. A higher *Jcv* ratio of 1 °C/min demonstrates low dielectric loss of TiO_2 on graphene annealed at the lowest annealing rate, attributed to an increase in electron density coupled with less charge recombination.

The surface energy loss function (*SELF*) and volume energy loss function (*VELF*), derived using equations 2.35 and 2.36 respectively, represent the energy transferred to and from the topmost atom layer of a compound semiconductor as a result of electron excitation in the surface and bulk. The effective *VELF/SELF* ratio dependent on photon energy in the visible and ultraviolet regions of TiO_2 on graphene

for as deposited and annealed films are presented in figure 4.16 (b). It was found that when photon energy rose, the effective *VELF/SELF* decreased. Table 4.4 displays the *SELF* and *VELF* values for as deposited, 1 Step, 1 ^{o}C/min, and 2 ^{o}C/min at hv = 2.26 eV. It is found that volume energy losses transcend surface energy losses, indicating that electrons lose more energy moving through the bulk than the surface. When annealing rates decrease, *SELF* and *VELF* both decrease and exhibit roughly the same behavior as free charge carriers pass through the bulk and surface. In comparison, 1 ^{o}C/min exhibited the lowest *VELF/SELF*, indicating that the films' crystallinity had improved due to higher ad atom surface mobility on the glass substrate and a favorable TiO_2 anchor on graphene. Previous research indicates that the stimulation of the electron's plasma oscillation results in a greater loss of energy when a fast-moving electron travels through bulk rather than the medium's surface (Yang *et al.,* 2008; Yakuphanoglu *et al.,* 2004; Sarkar *et al.,* 2014).

Equations 2.22 and 2.23 in that order relate optical conductivity (σ_{opt}), electrical conductivity (σ_e), and absorption coefficient (Astinchap *et al*., 2017). The variation in σ opt for as deposited and annealed TiO_2 on graphene films as a function of photon energy is shown in figure 4.16 (c). Since the photon energy stimulates the electrons, the figure indicates that σ opt increases with photon energy. 1 ^{o}C/min annealing rate revealed highest optical conductivity. This phenomenon can be explained by a TiO_{1-x} oxygen deficit acting as donor defects because of titanium interstitial states and oxygen vacancies (Nowotny *et al.,* 2005). Maximum optical conductivity is observed for films annealed at 1 ^{o}C/min, due to the effect of oxygen vacancies on the carrier density of the film (Yakuphanoglu *et al*., 2004). Figure 4.16 (d) depicts the relationship between electrical conductivity, σ_e and photon energy. It is worth noting that σ_e decreases dramatically as photon energy increases due to electron entrapment at defect centers hence conducting the electrons to graphene. Electrical conductivity for 1 ^{o}C/min annealing rate was the highest, which can be attributed to enhanced crystallinity and lattice absorption.

4.3.4.3 Absorption Spectra Analysis of TiO_2 on Graphene

The absorption coefficient (α) of a material is largely influenced by scattering energy losses and basic absorption. Absorption coefficient values were obtained using Drude Model in scout software as illustrated in section 2.9. The absorption coefficient of TiO_2 on graphene decreased as the wavelength increased. Given that low photon energy is insufficient to transfer an electron from the valence band to the conduction band of a semiconductor, a low absorption coefficient at high wavelength implies a limited likelihood of electron transition. Since photon, energy is sufficient at shorter wavelengths, the potential of electron transition increases. The probability of an electron transition increases as the value of α increase over 10^4 cm^{-1}. At 10^4 cm^{-1}, the electron transition is indirect; therefore, the phonon maintains the electron momentum (Crane & Hassan, 1989). Table 4.4 shows the values for α at λ = 550 nm within the transparent zone. α increased with lowest annealing rate, 1 ^oC/min indicating the maximum α, implying that there is a higher possibility of electron transfer due to closeness in the topmost points of a valence band and the bottom most points of a conduction band.

Table 4.4: Electron Transition and Transport Parameters of TiO_2 on Graphene Thin Films at Various Annealing Rates

Samples	J_{cv1} x 10^{-6}	J_{cv2} x 10^{-6}	Self	Velf	Velf/Self	α x 10^3	σ_{opt} x 10^{13}	σ_e x 10^{10}
As-Dep	5.13	2.13	0.10	0.57	5.98	36.55	17.34	4.57
1 Step	2.33	0.23	0.02	0.35	20.64	5.92	2.51	3.89
2°C/min	2.95	1.11	0.07	0.93	12.85	6.99	2.79	4.13
1°C/min	4.04	2.73	0.14	0.95	6.75	28.58	13.20	4.60

Figure 4.17 illustrates the relationship between porosity and nonlinear susceptibility. Nonlinear susceptibility increased with 1 ^oC/min annealing rates displaying the highest values.

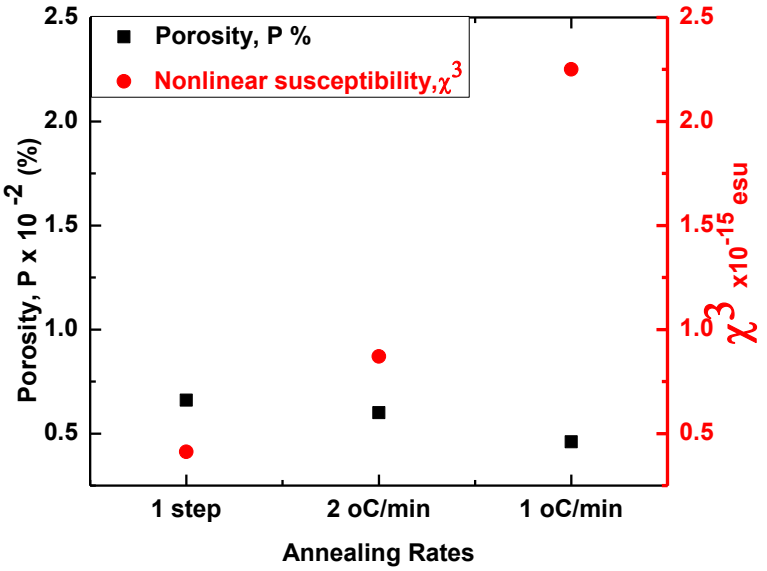

Figure 4.17: A Plot of Porosity and Nonlinear Susceptibility (χ^3) of Annealed TiO_2 on Graphene Films for Different Annealing Rates

Additionally, it was observed that porosity decreased towards low annealing rates. This was ascribed to a progressive improvement in film crystallization, film pore filing, and densification as a result of local matter migration spurred on by particle diffusive sintering. Mugambi *et al*., (2021) found higher porosity values for TiO_2 films anchored on FTO than we observe for TiO_2 on graphene due to the vast surface area of graphene that provides a scaffold anchor for TiO_2. Small pores and voids at the FTO/TiO_2 interface result in increased porosity due to the uneven microstructure of FTO glass.

According to Al-Jufairi (2012), annealing duration and temperature have an effect on porosity aggregate and film quality. The immense nonlinear susceptibility of graphene TiO_2 sheets of order 10^{-14} esu is related to a significant amplification of the local field. Nonlinear optical susceptibility enhanced with 1 ^oC/min showing the highest value, owing to lattice vibration and dispersion effects caused by grain size growth as the film transitioned from amorphous to crystalline. The increased SEL/VEL is due to the enhanced crystalline quality of TiO_2 sheets. The surface-to-volume ratio has the same pattern as dispersion energy. As a consequence, the effect of TiO_2 anchoring on graphene and the annealing temperature was satisfactorily assessed. The films

annealed at 1 ^{o}C/min showed enhanced diffusion rate, longer electron lifespan due to lower recombination rate, and improved crystallinity, which promoted electron transport.

4.4 FTIR, Optical Spectroscopy and Electrical Characterization of TiO_2 on FTO and on Graphene

4.4.1 Five Zone Fourier Transform Infrared Analysis

A significant tool for analyzing the structure, bonding, and reactive materials is FTIR spectroscopy. Vibration spectra were used to study the interaction between graphene and TiO_2 nanoparticles in the 400–4000 cm^{-1} region. Figure 4.18 illustrates the FTIR spectra of TiO_2 on graphene films for as-deposited condition as well as TiO_2 on graphene annealed at 1 step, 2 ^{o}C/min, and 1 ^{o}C/min rates. High absorption corresponds to low infrared transmission at high wavenumber. The absence of a certain bond and, thus, the absence of photon absorption are indicated by a particular frequency that has no peaks. The infrared spectra were examined using Real - Hardinger's Five Zone analysis (Hardinger, 2008).

Zone 1 exhibits absorption peaks in the range of 3700 to 3200 cm^{-1}, followed by Zones 2 from 3200 to 2800 cm^{-1}, zone 3 from 2800 to 2100 cm^{-1}, zone 4 from 800 cm^{-1}, and zone 5 from 800 and 400 cm^{-1}, correspondingly. According to Maiara *et al.* (2001), the stretching vibration modes of hydroxyl groups are associated with the bandwidth between 3200 and 2800 cm^{-1}. OH, groups are highly advantageous for increasing photocatalytic activity because they can receive photo-induced holes, form OH radicals, and act as electron donors for generated H^{+}.

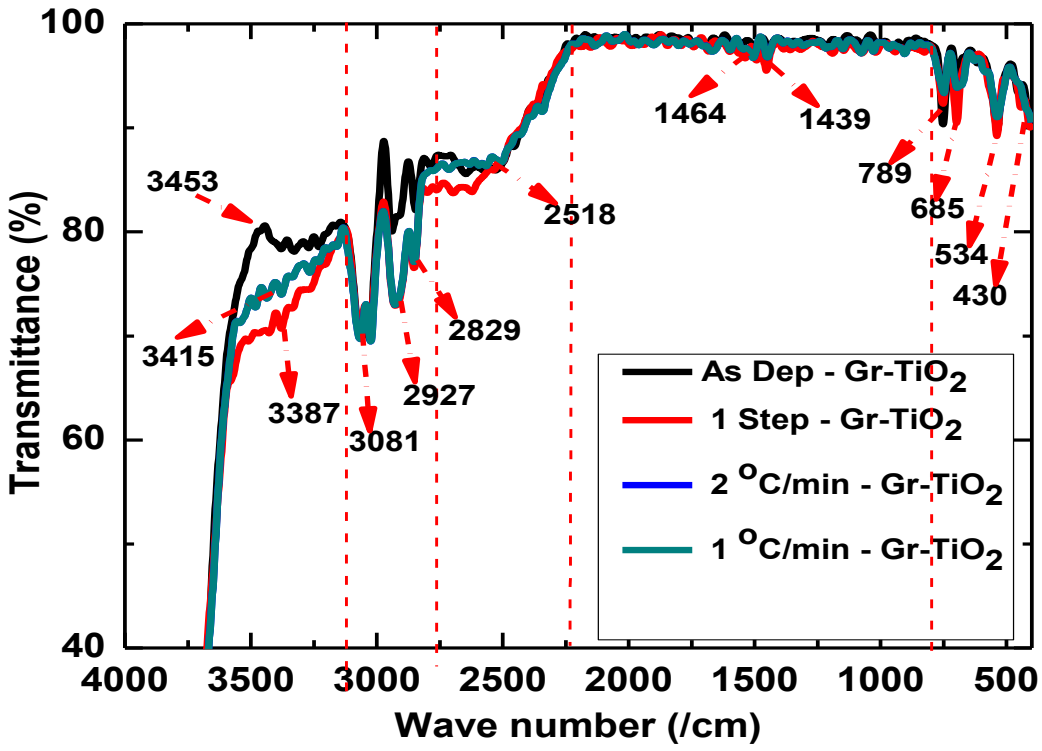

Figure 4.18: A Graph of FTIR Transmittance for as Deposited and Annealed TiO_2 on Graphene versus Wavenumber

The absorption peaks at 2927, 2829, 3016, and 3081 cm^{-1} are considered to be generated by the stretching mode of aliphatic C-H groups (Kumar *et al.*, 2015). A significant surface IR absorption enhancement in spectrum intensity in C-H groups was observed when TiO_2 molecules were adsorbed on the graphene film surface via the n electron of the O atom of the titanium ring. Borodko *et al*. (2006) also found that PVP molecules had higher intensities in these bands when Pt Nps was present. The C=O vibration and the bending vibration of the H-O-H bond on TiO_2 are linked to absorption peaks at 1650 cm^{-1} (Yuan *et al.*, 2010). The stretching vibration of C-O and the C = C aliphatic vibration is associated with the peaks at 1249 and 1097 cm^{-1}, respectively. The carboxylic group attached to Ti as a bidentate ligand (Nolan *et al.*, 2009) exhibited symmetric and asymmetric stretching vibrations as a result of the doublet at 1520 and 1448 cm^{-1}. Furthermore, a minor red shift at the C = O stretching vibration from 1464 to 1439 cm^{-1} (approximately 5 cm^{-1}) suggests that TiO_2 molecules adsorb on the graphene surface via the O atom of the C = O (Behera & Ram, 2012). The findings also supported the presence of a prominent feature centered at 430 cm^{-1}

during annealing, which is typical of anatase TiO_2. The FTIR spectra of the as-deposited TiO_2 film, annealed TiO_2 on graphene, TiO_2 on FTO, and Graphene, FTO, and TiO_2 films in the 400–4000 cm^{-1} spectrum at a rate of 1 ^oC/min are shown in figure 4.19. Exciting new insights into the structural dynamics of this complex can be garnered by comparing the IR depletion spectra at 1 ^oC/min annealing a rate.

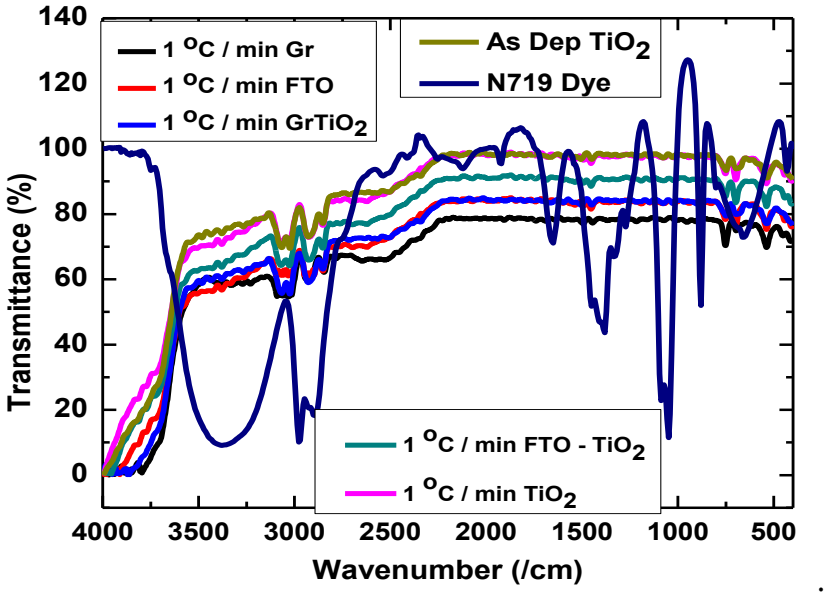

Figure 4.19: A Graph of FTIR Transmittance Spectrum of N719 Dye, Graphene, FTO, TiO_2, TiO_2 on FTO and on Graphene against Wavenumber

The vibration of Ti-O-Ti and C-O-Ti was attributed to the substantial absorption at low frequency (below 798 cm-1), which aided the formation of the TiO_2 and C-O-Ti bonds in graphene TiO_2 heterojunction. Low annealing rate (1 ^oC/min) result in higher C-O stretching, C-O-Ti bonds, and C=O carbonyl stretching, all of which have the potential to increase graphene TiO_2 electrical conductivity and improve photo-induced charge transfer. The vibration bonds at 430, 685, and 789 cm^{-1} correspond to the bonds Ti-O-Ti, Ti-O-O, and Ti-O, respectively, whereas the LO mode of amorphous TiO_2 is 874 cm^{-1}. According to Yuan et al. (2010), metal oxides such as Ti-O, Sn-O-Ti, and C-O-Ti can be observed in the vibration spectrum below 700 cm^{-1}. The 534 cm^{-1} peak is extremely weak for samples annealed at annealing rates other than 1 ^oC/min, suggesting that the film annealed at 1 ^oC/min is well-crystallized. The following

section discusses the optical and electrical characterization of TiO_2 on FTO and graphene following FTIR confirmation of carbon bonds in the TiO_2 on graphene films.

4.4.2 Optical Spectroscopy of TiO_2 on Graphene Films

The optical band gap of TiO_2 on graphene sheets was calculated using the curve of $(\alpha h\upsilon)^2$ against $h\upsilon$ shown in figure 4.20. Tauc bandgap was obtained from equation 2.21 discussed in section 2.6.1. $(\alpha h\upsilon)^2$ were found to rise as photon energy increased. Bandgap (E_g) was acquired by fitting linear in the spectra within the UV region and reading the abscissa intersection. As the annealing rate lowered, consequently decreased the bandgap. Bandgap measurements for TiO_2 on graphene 1 step 3.33 eV, 2 ^oC/min 3.22 eV, and 1 ^oC/min 3.04 eV were remarkably close to the bandgap of anatase TiO_2, which is roughly 3.2 eV, owing to the minimal effect of graphene being a semimetal with zero band gap. The tauc bandgap of TiO_2 on FTO was found to be 3.49 eV for as deposited and ranged from 3.35 to 3.54 eV for annealed films. The wide tin band gap is related to the broadened bandgap of TiO_2 on FTO. It is clear that altering annealing rates to 1 ^oC/min triggers a red shift in the fundamental absorption edge of TiO_2 on graphene. The wide bandgap of TiO_2 on FTO indicates that incorporating TiO_2 into graphene improves DSSC performance by increasing light absorption intensity.

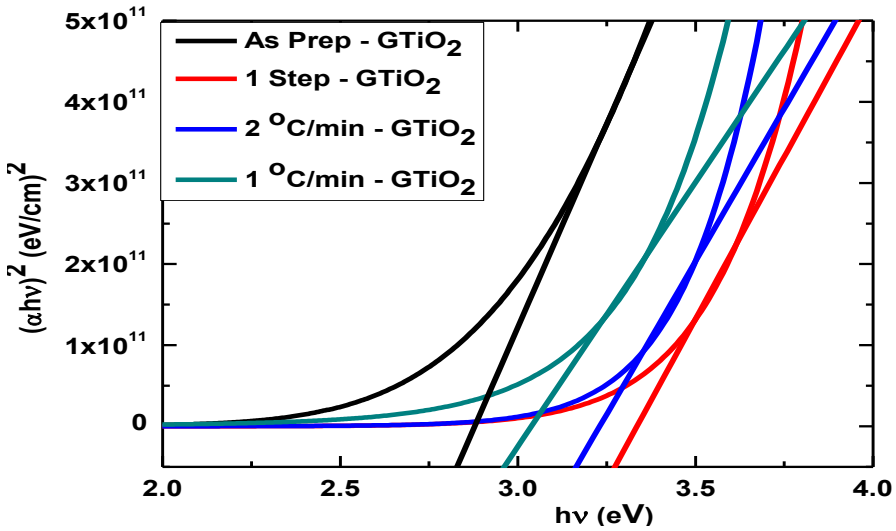

Figure 4.20: A Graph $(\alpha h\upsilon)^2$ Spectrum versus $H\upsilon$ for TiO_2 on Graphene

The Tauc bandgap values recorded near the absorption edge are consistent with the Wemple Didominico (WDD) band gap values observed in the transparent zone. The WDD bandgap was calculated using equation 2.27 (Wemple & DiDomenico, 1969; Wemple & DiDomenico, 1971).

TiO_2 graphene's WDD bandgap values were found to be 4.89 eV for as deposited and 2.33 eV, 2.73 eV, and 2.88 eV at, respectively, one step, 2 ^oC/min, and 1 ^oC/min annealing rates. Figure 4.21 exhibit a correlation model of porosity, Tauc band gap, and WDD bandgap. It turned out that porosity decreased towards the low annealing rate (1 ^oC/min). The gradual improvement of the films' crystallinity as a result of local matter migration brought on by particle diffusion sintering contributes to this reduction. The bandgap is lowered as a result of oxygen vacancies and Ti^{3+} states that are created in the bandgap when TiO_2 is annealed on graphene. In addition, integrating TiO_2 on graphene results in the formation of a C-Ti bond, which improves electron transfer from TiO_2 to graphene by preventing recombination, extending the duration of separated carriers, lowering the bandgap, and achieving photocatalytic response in the visible region.

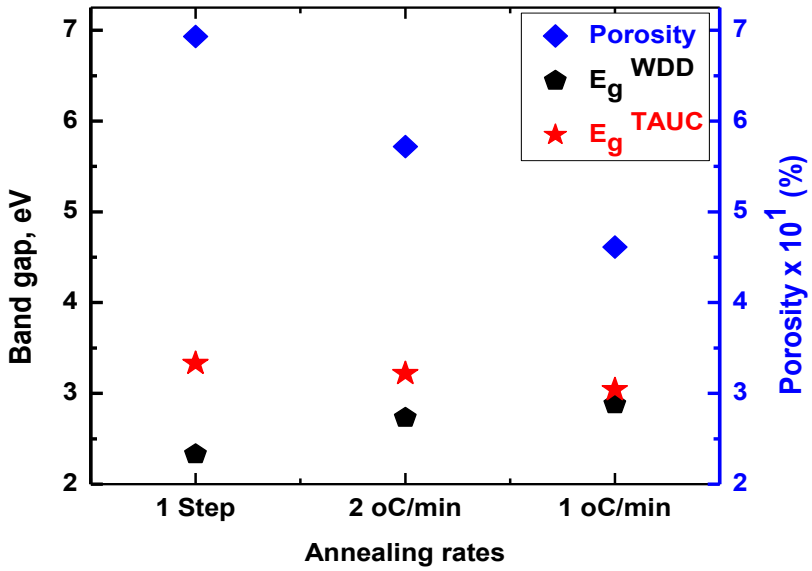

Figure 4.21: A Plot of Porosity and Band Gap of TiO_2 on Graphene Films against Various Annealing Rates

The lowest porosity of 1 ^oC/min annealing rate was associated to film contraction owing to local matter migration. The band gap of TiO_2 on graphene is within the TiO_2 range given that the graphene Dirac point resonates with the TiO_2 conduction band. Band gap opening occurring at 1-step annealing rate is due to the distortion of graphene Dirac cones around the K Point of the Brillouin zone caused by a sharp increase in temperature (thermal fluctuation) (Yakovkin, 2016).

4.4.3 Hall Effect Measurements of TiO_2 on Graphene Films

An applied magnetic field perpendicular to the current, coupled with an electric current in the conductor, generated a voltage difference (the hall voltage) across TiO_2 on graphene, resulting in the Hall Effect. Equation 2.39 was used to compute the vertical resistance (*RA*) and horizontal resistance (*RB*). The Van Der Pauw approach was used to calculate the sample's sheet resistance Rs using equation 2.40. Hall (1879) introduced equations 2.41, 2.42, and 2.43 to calculate charge concentration (n_s), charge mobility (μ_s), and conductivity (σ). Table 4.5 shows Hall Effect measurements.

Table 4.5: Hall Effect Measurements of as Deposited and Annealed TiO_2 on Graphene Films

Samples	V_H (mV)	R_s x 10^3 (Ω/cm)	n_s x 10^{15} (cm^{-2})	μ_s x10^1 $(vs)^{-1}$	σ x10^{-3} $(\Omega cm)^{-1}$
As-Dep	1.943	10.44	4.366	1.370	9.582
1 Step	1.875	9.641	4.524	1.431	10.37
2°C/min	1.798	8.443	4.718	1.567	11.84
1°C/min	1.734	6.690	4.892	1.907	14.95

Hall carrier concentration and mobility were shown to rise as annealing rates decreased, which was associated with improved crystallinity and crystallite size growth. Conductivity increased with 1 ^oC/min annealing rate exhibiting the least value. Figure 4.22 shows a relationship between porosity and conductivity in annealed graphene TiO_2 sheets.

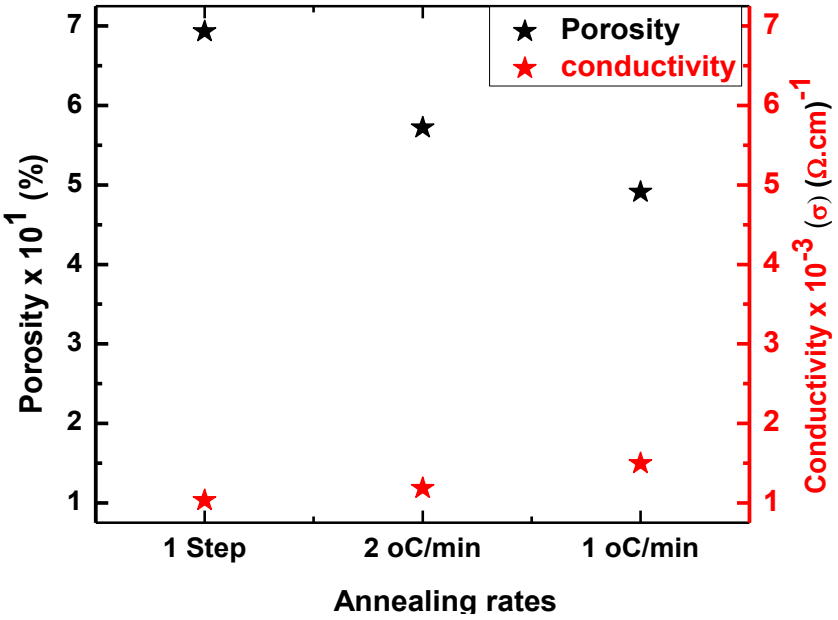

Figure 4.22: A Plot of Porosity and Conductivity of Annealed TiO_2 on Graphene at Different Annealing Rates

The microstructure of the film improved when annealed at low rate (1 ^oC/min), resulting in reduced potential barriers and wells (larger grain size) at grain boundaries and less TiO_2 agglomeration on graphene, resulting in enhanced charge percolation and hence excellent conductivity. Porosity was observed to decline, 1 ^oC/min, having

the lowest value attributed to local matter migration caused by film compacting and contraction. Similarly, conductivity rose as porosity decreased. This is because as the pore size decreases, the electronic interaction between TiO_2 particles improved. TiO_2 on graphene annealed at 1 ^oC/min had a porosity of 0.4612 (46.12 %), which was found to be close to the optimal porosity of 0.41 (41 %) that Saito *et al.*, (2004) reported as providing an excellent anchor site for dye molecules, hence elevating photocurrent generation in DSSCs. The film's comparatively high conductivity also qualifies it for use in solar cell applications.

4.4.4 Comparison of Energy Losses, Porosity and Dispersion Energy of TiO_2 on FTO and TiO_2 on Graphene Deposited Films

The oscillator energy, E_o, and dispersion energy for 1 ^oC/min TiO_2 on FTO and graphene were determined by graphing $(n^2-1)^{-1}$ versus $(h\nu)^2$, as seen in figure 4.23 (a). The $(n^2-1)^{-1}$ spectrum decreases as $(h\nu)^2$ rises. The high specific BET area of graphene allows for an extensive dispersion of films in the visible range. E_o and E_d values were determined by fitting linearly on the $(h\nu)^2$ axis between 2.7 $(eV)^2$ and 8.7 $(eV)^2$. The average excitation energy for TiO_2 on graphene films was found to be higher than that of TiO_2 on FTO, as shown in sections 4.2.4 and 4.3.3, meaning that TiO_2 on graphene films has a higher possibility of an electron interband transition than TiO_2 on FTO. Porosity vs photon energy plots of TiO_2 on FTO and TiO_2 on graphene annealed at a rate of 1 ^oC/min are shown in Figure 4.23 (b). As $h\upsilon$ rose, porosity was found to decrease. In the visible spectrum, porosity values were determined at photon energies of 2.26 eV. The porosity of TiO_2 on graphene at the given energy was significantly lower than that of TiO_2 on FTO, as seen in figure 4.23 (b), suggesting that the latter progressively enhanced the film crystallization quality over the former. This additionally is associated to local matter migration spurred on by densification and the film pole filing, leading to film contraction (Yager *et al.*, 2006).

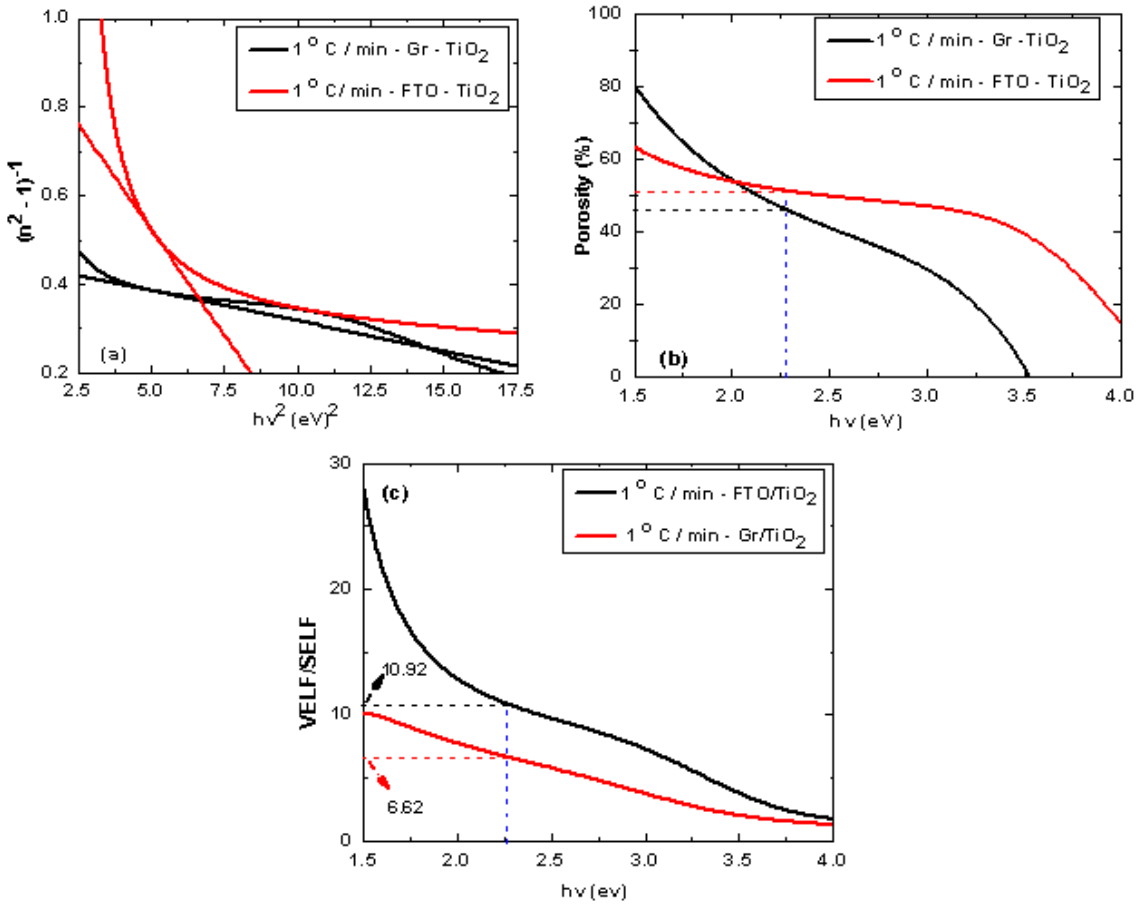

Figure 4.23: A Comparison of FTO/TiO_2 and Graphene/TiO_2 of 1ºC/min Deposited Films, Involving (a) Dispersion and Excitation Energy, (b) Porosity, and (c) Energy Losses Parameters in Variance with Photon Energy (hv)

The energy transferred to and from a compound semiconductor's topmost atom layer as a result of electron excitation in the bulk and surface is expressed by the volume energy loss function (*VELF*) and surface energy loss function (*SELF*). In the visible and ultraviolet regions of TiO2 on graphene and TiO_2 on FTO films annealed at a rate of 1 ºC/min, figure 4.23 (c) illustrates that effective *VELF/SELF* reduces as photon energy increases. According to reports, the *SELF/VELF* values of TiO_2 on graphene and TiO_2 on FTO were 6.62 and 10.92 for hv = 2.26 eV, respectively. TiO2 on graphene annealed at 1 ºC/min was found to have a lower *VELF/SELF* than TiO_2 on FTO, suggesting that the former crystallized more effectively than the latter because of a favorable anchor of TiO_2 on graphene and increased surface mobility of ad atoms on the glass substrate (Valluzzi *et al.*, 2018).

4.4.5 Light Absorption Coefficient and the Electron Diffusion Coefficient in TiO_2 on Graphene Films

Nanoporous TiO2's porosity (*P*) affects light absorption coefficient (α) and electron diffusion coefficient (*D*) (Ferber & Luther, 2001). For densely packed particles, porosity, *P*, with a maximum coordination number CN = 6 was found to be 0.41 (41 %) (Saito *et al*., 2004). Equation 2.13 was used for determining the light absorption coefficient, α. The electrode porosity can influence electron transport that depends on particles interaction. Equation 2.14 expresses the effect of porosity on the electron diffusion coefficient, D (Lee *et al.,* 2004). Table 4.6 shows α and *D* for as-deposited and annealed TiO_2 on FTO and TiO_2 on graphene. It became apparent that both α and *D* for TiO_2 on FTO and TiO_2 on graphene increased, with the maximum values occurring at the lowest annealing rate (1 ^oC/min).

Table 4.6: Light Absorption Coefficient α, and Electron Diffusion Coefficient D for TiO_2 on FTO and TiO_2 on Graphene Films

	TiO_2 on FTO		TiO_2 on graphene	
Samples	**α x 10^3 (cm^{-1})**	**D x 10^{-4} (cm^2/s)**	**α x 10^3 (cm^{-1})**	**D x 10^{-4} (cm^2/s)**
As-Dep	4.448	1.379	4.776	1.564
1 Step	2.503	0.2206	2.823	0.4349
2°C/min	3.475	0.8266	3.806	1.016
1°C/min	4.221	1.251	4.637	1.485

Since TiO_2 is more crystalline on graphene than on FTO, our investigations showed that when TiO_2 was deposited on graphene, the light absorption coefficient and electron diffusion coefficient obtained were higher than those obtained when TiO_2 was embedded on FTO. This higher light absorption coefficient is ascribed to electron lattice/hole interaction related to phonon formation, photon propagation in the scattering volume, and the creation of excited electron hole states. We can attribute the enhanced film conductivity to the heightened probability of an electron diffusion coefficient. According to Benkstein *et al.* (2003), high deposition temperatures ($\geq$ 450 ^oC) greatly minimize bond dilatation in the grain boundaries, which in turn minimizes charge density fluctuation thus can also account for enhanced conductivity at the lowest annealing rates.

4.5 Work Function and Contact Potential Difference of TiO_2 on Graphene Films

Figure 4.24 shows two-dimensional (*2D*) plots of area scan profiles across four samples with varied annealing rates to investigate the surface contact potential on nanocomposite thin films.

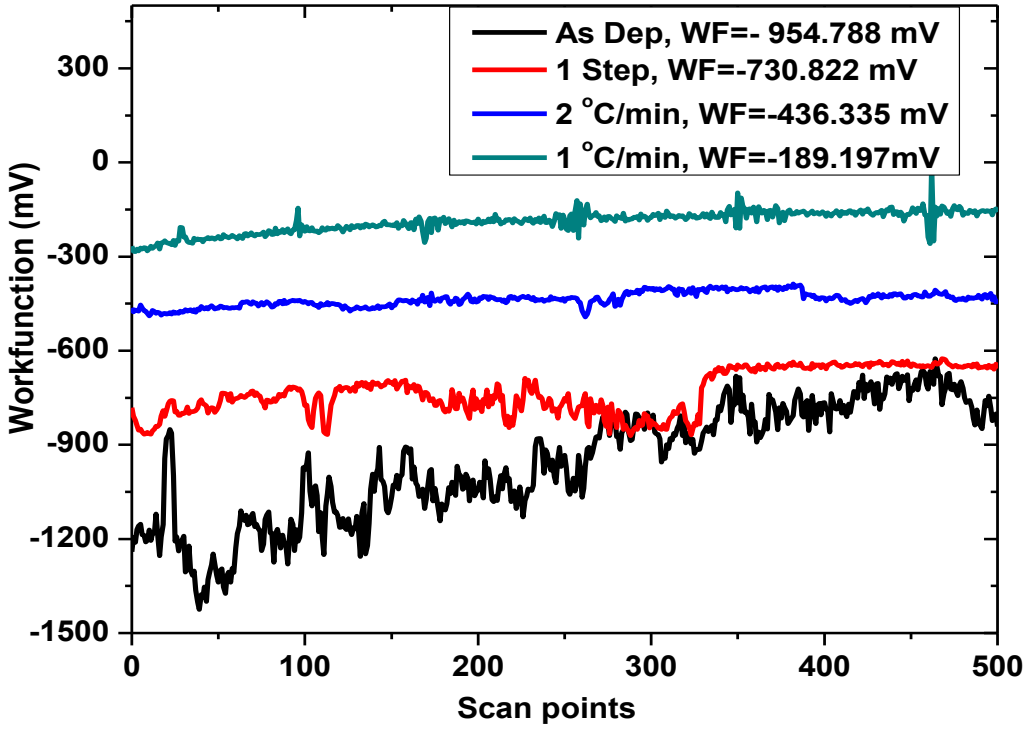

Figure 4.24: Work Function against Topographical Scan Maps of as Deposited TiO_2 on Graphene Thin Films and Films Annealed at 1-Step, 2 ^oC/Min, and 1 ^oC/Min

The average work function for as deposited, 1 step, 2 ^oC/min, and 1 ^oC/min were -954.788 mV, -730.822 mV, -436.335 mV, and -189.197 mV, respectively, as determined by SKPM. The measured effective work function is influenced by modifications to surface structure and is not monotone. In this work, it has been reported that the work function varied with respect to annealing rates. Annealing causes a decrease in work function, which is associated to TiO_2's improved crystallinity. Differences in surface atomic configurations can be significant, resulting in shifts in work function about an electron volt (Kahn, 2016). Because low annealing (1 ^oC/min) affects the resultant sol - gel particle organization, the cause of the distinct

contact potential difference has different surface orientation of the crystalline structures.

Figure 4.25 shows spectra of work function against topographical linear step profile points for as deposited and TiO_2 on graphene films annealed at different annealing rates. Profiles at different locations from *SKPM* of TiO_2, indicates that varying annealing can affect morphology and surface potential of the film hence can be used to control electronic structure of semiconductor/graphene interface (Duong *et al.,* 2019). The tip scans over a particle, causing an abrupt increase in height and a decrease in local V_{CPD}, thereby increasing the local work function. Thermal reduction is one method for modifying the electronic properties of oxides that are doped with oxygen vacancies (Grant, 1959). Work function is characteristic of reduced crystals with a high number of oxygen vacancies after annealing at lower annealing rates. Surface atomic arrangements differences can be quite significant and linked to shifts in work function (Duong *et al*., 2019). The distribution of charges at the surface and potential step can be attributed to crystallography orientation and atomic relation, as the extent of the charge separation depends on the average position of ions in the surface and sub – surface atomic planes (Kahn, 2016). The observed variation in the work function with annealing relates to a concomitant shift in the Fermi level of TiO_2 (Valluzzi *et al*., 2018).

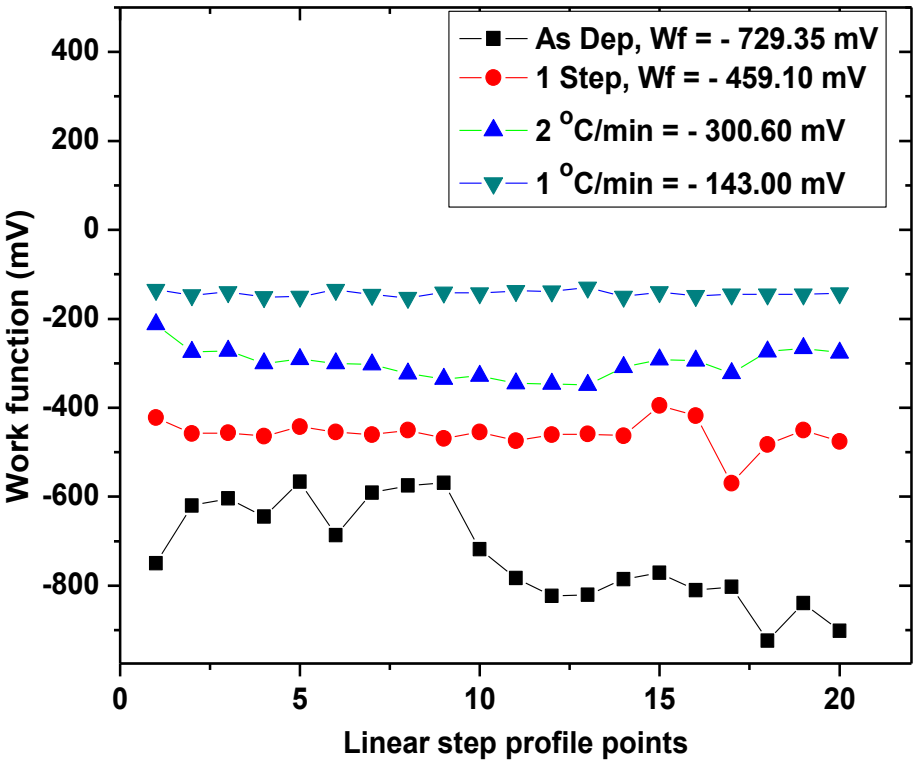

Figure 4.25: Work Function of as Deposited TiO_2 on Graphene Thin Films and Films Annealed at 1 °C/min, 2 °C/min, 1-Stepannealing Rates in Comparison with Topographical Linear Step Profile Points

The contact potential depends on the tip geometry, tip sample distance and environment conditions such as the presence of ad sorbates, surface charges, and oxide layers on the sample surface (Valluzzi *et al.*, 2018). The cause of distinct contact potential difference is due to different surface orientation of the crystalline structures as reported by Strayer *et al.*, (1973), since slow annealing affects resultant sol – gel particles organization (Rabani *et al.*, 2003). Thermal reduction is one way of manipulating the electronic properties of oxides that end up to doping with oxygen vacancies (Grant, 1959). Titanium dioxide crystal lattice release oxygen under reduction conditions leaving behind d – electrons and oxygen vacancies (Sheppard *et al.*, 2006). Work function is characteristic after annealing at higher temperatures for reduced crystals having a large amount of oxygen vacancies (Sasahara & Tomitori, 2013).

4.6 Photovoltaic Characterization of DSSCs

Mesoporous TiO_2 films treated at low annealing rate (1 ^oC/min) exhibited the best photocatalytic characteristics thus viable candidates for use as working and counter electrodes in DSSCs, according to the reported optical spectroscopy, SKPM and Hall Effect measurements in this work. The ideal dye-sensitized TiO_2 that is annealed at 1 ^oC/min demonstrates optimum porosity, highest multiple light scattering and absorption capabilities, better electron transport coefficient, and increased sheet conductivity. **C1** (FTO/TiO_2 - Pt/FTO), **C2** (Gr/TiO_2 - Pt/FTO), **C3** (FTO/TiO_2 - Pt/Gr), and **C4** (Gr/TiO_2 - Pt/Gr) DSSCs were fabricated and labeled. Figure 4.25 depicts their I - V characteristics measured at 100mW/cm^2 (AM 1.5) illumination.

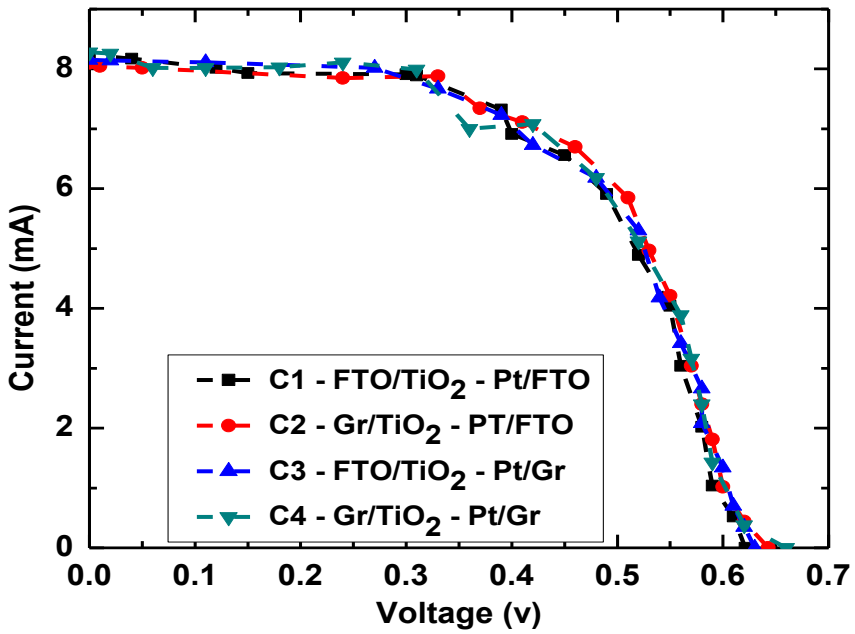

Figure 4.26: *J-V* Characteristics of DSSCs Evaluated under 100 mW/cm^2 (AM 1.5) Illumination Using CE1, CE2, CE3, and CE4 as Reference Points

Table 4.7 contains the DSSC's open circuit voltage (V_{oc}) and short circuit current (I_{sc}). It was found that the average values for I_{sc} and V_{oc} were 8.1925 mA and 0.6375 V, respectively. The variation in I_{sc} is determined by the efficiency of charge collection and electron injection from the N719 dye to the TiO_2 *CB*, whereas the variation in V_{oc} of DSSCs and the potential of the redox couple are determined by the TiO_2 quasi-

Fermi level (Allegrucci *et al.,* 2009). Due to its near-optimal porosity of TiO_2 on graphene, high light absorption coefficient, and high electron diffusion coefficient, C4 exhibited the highest *PCE* (%) = 2.973. Numerous studies have been conducted on the mechanisms and rates of charge transfer via electrode surfaces under different modifications (Hauch & Geog, 2001; Yang *et al.,* 2015). Tiny voids and gaps at the FTO/TiO_2 interface are induced by the high porosity of TiO_2 and the uneven microstructure of FTO glass. These voids and gaps accelerate up the recombination process and disrupt conduction of charges. These gaps are filled by the remarkable mobility and flexibility of the graphene layer, and when TiO_2 is compacted to it, it can improve the passivation of the interface by lowering the charge transfer resistance.

Table 4.7: DSSC Characteristics of TiO_2 on FTO and TiO_2 on Graphene WE Annealed at 1 ºC/Min

	C1	**C2**	**C3**	**C4**
I-V Parameters	**FTO/TiO_2 – Pt/FTO**	**Gr/TiO_2 – Pt/FTO**	**FTO/TiO_2 – Pt/Gr**	**Gr/TiO_2 – Pt/Gr**
V_{oc} (V)	0.62	0.64	0.63	0.66
I_{sc} (mA)	8.24	8.10	8.15	8.28
J_{sc} (mA/cm^2)	8.24	8.10	8.15	8.28
I_{max} (mA)	6.38	6.85	6.35	6.76
V_{max} (v)	0.45	0.43	0.46	0.44
P in (W/cm^2)	0.1	0.1	0.1	0.1
FF	0.562	0.568	0.569	0.544
η (%)	**2.871**	**2.944**	**2.922**	**2.973**

When the sub-band gap becomes deeply embedded in the tail of the density of states in annealed TiO_2 on graphene composite material, oxygen vacancies and Ti^{3+} defects form, accelerating the interband transition and narrowing the band gap. Due to its higher work function and positive fermi level in comparison to TiO_2 conduction band, these defects act as electron trapping centers, tunneling electrons to graphene. TiO_2 and graphene interact strongly to form Ti - O - C and Ti - C interfaces, which not only serve as a conduit for fast electron transfer but also generate energy levels within the TiO_2 bandgap, which can increase visible light absorption. Graphene possesses excellent electrical conductivity, homogenous structure; bridging layer minimizes

resistance to the photo generated electrons suppressing the recombination and back reaction processes (Eshaghi & Aghaei, 2015; Fan *et al.*, 2012).

4.7. Principles of Diminution of the Fabricated DSSC Efficiency

The stability of DSSCs, fundamental fabrication procedures and materials, and the operation of the cells are all contributing reasons to the low efficiency of developed solar cells. Failure to reduce an oxidized dye to its original ground state following electron injection during the regeneration process has a significant impact on maximum photo voltage; hence, the redox couple's potential should be near to the dye's ground state. Difficulty in attaining TiO_2 nanoparticles having the ideal porosity at Working Electrode, required for maximal photoelectron production led to the low efficiency. Creation of the dark current by coating the conduction glass plate with a thin layer of unevenly size TiO_2 reducing both the open-circuit voltage and the fill factor. Trapping generated electrons within nanoporous TiO_2 nanoparticles or in an electrolyte solution. If the sensitizer is not applied uniformly across the entire surface of the nanoporous TiO_2 electrode, naked domains can collect electrons, limiting efficiency.

CHAPTER FIVE

CONCLUSION AND RECOMMENDATIONS

5.1 Conclusion

This study successfully designed, synthesized, characterized, and employed novel TiO_2 nanocomposites and nanostructures as efficient photoanode materials to enhance the anode films' scattering effect, dye loading, and electron transport property, thereby improving the performance of dye-sensitized solar cells (DSSCs). Fundamentals of DSSC operation, device setup, and assessment techniques were discussed in detail, along with the latest developments in TiO_2-based photoanode optimization. By tracing a 1 x 1 cm^2 window using scotch magic tape placed on the conductive side of the glass substrates, TiO_2/FTO and TiO_2/graphene composite electrode thin films were successfully deposited using the Doctor Blade technique. FTIR data was collected in the range 400 cm^{-1} – 4000cm^{-1} whereas UV VIS obtained in the range 300 – 800nm. FTIR revealed that TiO_2 on Fluorine Tin Oxide and TiO_2 on graphene films annealed at 1 ^oC/min had the lowest transmittance implying that the films required to absorb more radiation to cause the same bond vibration with other films. TiO_2 on graphene heterojunctions showed notable FTIR absorption at low frequencies (below 798 cm^{-1}), confirming the formation of Ti-O and C-O-Ti bonds. At 438 cm^{-1}, the significant anatase TiO_2 feature was detected. The local energy density and bond critical point of the electron density distributions shown bond interactions and the stronger covalent character of its bonds anticipated to improve electron transport.

The experimental results demonstrate that TiO_2 on graphene and TiO_2 on FTO films annealed at 1 ^oC/min are ideal for optoelectronic applications because of their optimal porosity, VELF/SELF ratio, and high light absorption coefficient, electron diffusion coefficient, and conductivity. **C1** (FTO/TiO_2 - Pt/FTO), **C2** (Gr/TiO_2 - Pt/FTO), **C3** (FTO/TiO_2 - Pt/Gr), and **C4** (Gr/TiO_2 - Pt/Gr) DSSCs were fabricated and labeled. I_{sc} and V_{oc} average values were found to be 8.1925 mA and 0.6375 V, respectively. As a result, we were able to successfully assess the effect of anchoring TiO_2 on graphene and annealing temperature. **C4** had the highest PCE (%) = 2.973 (3.4 % increment on C1), which can be attributed to its high light absorption coefficient, high electron

diffusion coefficient, longer electron lifetime due to low recombination rate, improved crystallinity by epitaxial graphene anchor, and positive fermi level.

Graphene main contribution to this research project is that it effectively improved the PCE of DSSCs by acting as a 2D electron transport enhancer in the photoanode. Graphene's exceptional electrical properties and high specific surface area make it a useful support material for dye loading boosting electron ejection from excited dye and electron bridge that improve electron transport in photoanodes. According to the study's findings, TiO_2 – graphene composites with optimized porous TiO_2 nanoparticles have higher PCE. This is because of the combined effects of fast electron transport in graphene nanosheets with compact TiO_2 particles act as a barrier to electron leakage and the high specific surface area created by the ultra-small TiO_2-formed porous structure. To improve electron transport efficiency, the low pore size TiO_2-graphene nanosheets collapse tightly onto one another and make closer contact when annealed at low rate (1 ^oC/min). This can reduce resistance at the TiO_2-graphene interfaces.

5.2 Recommendations

Graphene has a lot of potential in improving efficiency in DSSC when used in both working and counter electrodes. However, our fabricated DSSC did not achieve high efficiency due to a number of setbacks. This study proposes the following further research to improve the output of DSSC:

- **i)** Inclusion of a scattering layer on TiO_2 - graphene to disperse light and utilize the higher thickness characteristic in order to absorb energy below UV region.
- **ii)** Large-scale DSSC manufacture is hampered by the possibility of sealant corrosion and cell leakage, which are both brought on by the liquid electrolyte utilized in typical DSSCs. Modification of the ionic liquids-based electrolyte is required in order to achieve the replacement of the liquid electrolyte without a large PCE loss.
- **iii)** Research on the replacement of platinum catalyst with inexpensive and optimized p-type photo electrode, including the insertion of high-conductive

nanomaterials as a charge transport enhancer to improve PCE and comprehend the DSSC energy harvesting mechanism.

REFERENCES

Ahmadi, S., Asim, N., Alghoul, M., Hammadi, F., Saeedfar, K., Ludin, N., Zaidi, S., and Sopian, K. (2014). "The role of physical techniques on the preparation of photoanodes for dye-sensitized solar cells. Hindawi", *International Journal of Photoenergy*, 198734, 1-19.

Al-Jufairi J. N. (2012). "Electric properties and surface structure of TiO_2 for solar cells", *Energy*, 39: 6.

Al-Jufairi, N. (2006), "Structure and Surface Properties of Anatase TiO_2 Thin Film by Sol-Gel Technique," *Materials Science Forum*, 517: 165–172.

Allegrucci, A., Lewcenko, N. A., Mozer, A. J., Dennany, L., Wagner, P., Officer, D. L., & Spiccia, L. (2009). "Improved performance of porphyrin-based dye sensitised solar cells by phosphinic acid surface treatment". *Energy & Environmental Science*, *2*(10), 1069-1073.

Al-Mudhaffer, M. F., Nattiq, M.A. & Jaber, M.A. (2012). "Linear optical properties and energy loss function of Novolac: Epoxy blend film," *Archive Applied Science Research*, 4 (4): 1731 – 1740.

Astinchap, B., Moradian, R., & Gholami, K. (2017). "Effect of sputtering power on optical properties of prepared TiO_2 thin films by thermal oxidation of sputtered Ti layers," *Materials Science in Semiconductor Processing*, 63: 169-175.

Ayieko C. O., Musembi R. J., Waita S. M., Aduda B. O. & Jain P. K. (2003). "Structural and Optical Characterization of Nitrogen-doped TiO_2 Thin Films Deposited by Spray Pyrolysis on Fluorine Doped Tin Oxide (FTO) Coated Glass Slides," *International Journal of Energy Engineering*, 2(3): 67-72.

Balandin, A.A., Ghosh, S., Bao, W.Z., Calizo, I., Teweldebrhan, D., Miao, F. & Lau, C.N. (2008). "Superior thermal conductivity of single-layer graphene". *Nano Letters*, 8(3):p. 902-907.

Baxter, J.B., (2012). “Commercialization of dye sensitized solar cells: Present status and future research needs to improve efficiency, stability, and manufacturing”. *Journal of Vacuum Science & Technology A*. 30(2).

Behera, M. & Ram, S. (2012), “Synthesis and characterization of core-shell gold nanoparticles with poly (vinyl pyrrolidone) from a new precursor salt”. *Applied Nanoscience*. 3: 83–87.

Benkstein; K. D., Kopidakis, N., Van de Lagemaat, J. & Frank, A. J. (2003), “Influence of the Percolation Network Geometry on Electron Transport in Dye-Sensitized Titanium Dioxide Solar Cells”. *Journal of Physics and Chemistry B*. 107 (31), 7759–7767.

Bisquert, J., Zaban, A. and Salvador, P. (2002). “Analysis of the mechanisms of electron recombination in nanoporous TiO_2 dye-sensitized solar cells. None equilibrium steady- state statistics and interfacial electron transfer via surface states”. *Journal of Physical Chemistry B*. 106(34): 8774-8782.

Bolotin, K.I., Sikes, K.J., Jiang, Z., Klima, M., Fudenberg, G., Hone, J., Kim, P. & Stormer, H.L. (2008). “Ultrahigh electron mobility in suspended graphene”, *Solid State Communications*, 146(9-10): 351-355.

Borodko, Y., Habas, S. E., Koebel, M., Yang, P., Frei, H. & Somorjai, G. A. (2006), “Probing the interaction of poly (vinyl pyrrolidone) with platinum nanocrystals by UVRaman and FTIR”. *Journal of Physical Chemistry B* 110, 23052–23059.

Boschloo, G., & Hagfeldt, A. (2009). “Characteristics of the iodide/triiodide red-ox mediator in dye-sensitized solar cells”. *Accounts of Chemical Research*, 42(11), 1819-1826.

Chander, S., & Dhaka, M. S. (2016). “Thermal evolution of physical properties of vacuum evaporated polycrystalline CdTe thin films for solar cells”, *Journal of material science: Material in electronics*, 27: 11961 – 11973.

Chong, M.N., Jin, B., Chow, C.W.K. & Saint, C. (2010). “Recent developments in photocatalytic water treatment technology”, *A review, Water Research* 44(10), 2997-3027.

Chopra, K.L., Paulson, P.D. & Dutta, V. (2004). “Thin-film solar cells: An overview”, *Progress in Photovoltaics*, 12(2-3): 69-92.

Choudhury, B. D., Lin, C., Shawon, S.M.A.Z., Soliz-Martinez, J., Huq, H., & Uddin., M. J. (2021). “A photoanode with hierarchical nanoforest TiO_2 structure and silver plasmonic nanoparticles for flexible dye sensitized solar cell”. *Scientific reports* 11, 7552.

Choy, K. (2003). “Chemical vapor deposition of coatings”, *Progress in Materials Science*, 48(2), 57–170.

Crane, M., & Hassan, Y. (1989). "Solar Cells", *Collage of Education, University of Mosul.*

Cruz, M., Gomez, C., Duran-Valle, C. J., Pastrana-Martínez, L. M., Faria, J. L., Silva, A. M. T., Faraldosa, M., & Bahamondea, A. (2017). “Bare TiO_2 and graphene oxide TiO_2 photocatalysts on the degradation of selected pesticides and influence of the water matrix”, *Applied Surface Science*, 416, 1013–1021.

Cui, Y., Du, H., & Wen, L. S. (2008). Doped-TiO_2 photocatalysts and synthesis methods to prepare TiO_2 films. *Journal of Materials Science & Technology*, 24(5), 675-689.

Cui, Z., Zhao, M., Que, X., Wang, J., Xu, Y., Ghazzal, M. N., ... & Wu, W. (2021).

Facile Vacuum Annealing-Induced Modification of TiO_2 with an Enhanced Photocatalytic Performance. *ACS omega*, *6*(41), 27121-27128.

De Angelis, F., Fantacci, S., A., Selloni, Gratzel, M. &. Nazeeruddin, M. K. (2007). “Influence of the sensitizer adsorption mode on the open-circuit potential of dye-sensitized solar cells”, *Nano Letters*, 7(10), 3189-3195.

DiDomenico, M. & Wemple, S. H. (1969). “Oxygen-Octahedra Ferroelectrics. II. Electro-optical and Nonlinear-Optical Device Applications”, *Journal of Applied Physics*, 40, 720–734.

Duong, B., Lohawet, K., Muangnapoh, T., Nakajima, H., Chanlek, N., Sharma, A., Lewis, A. D., & Kumnorkaew, P. (2019). “Low-Temperature Processed TiOx/$Zn_{1-x}Cd_xS$ Nanocomposite for Efficient $MAPbI_xCl_{1-x}$ Perovskite and PCDTBT: $PC_{70}BM$ Polymer Solar Cells”, *Polymers*, 11, 980.

Dozzi, M. V., & Selli, E. (2013). Doping TiO_2 with p-block elements: Effects on photocatalytic activity. *Journal of Photochemistry and Photobiology C: Photochemistry Reviews*, 14, 13-28.

El-Nahass, M. M., Soliman, H. S. & El-Denglawey, A. (2016), “Absorption edge shift, Optical conductivity and energy loss function of nano thermal-evaporated N-type anatase TiO2 films,” *Aplied physics A*, 122:775.

Eshaghi, A., & Aghaei, A. A. (2015). “Effect of TiO_2-graphene nanocomposite photoanode on dye-sensitized solar cell performance”, *Bulletin of Materials Science*, 38(5), 1177–1182.

Fan, J., Liu, S., & Yu, J. (2012). “Enhanced photovoltaic performance of dye-sensitized solar cells based on TiO_2 nanosheets/graphene composite films”, *Journal of Materials Chemistry*, 22(33), 17027-17036.

Ferber; J., & Luther, J. (2001). “Modeling of Photovoltage and Photocurrent in Dye-Sensitized Titanium Dioxide Solar Cells”, *Journal of Physics and chemistry B*, 105 (21), 4895–4903.

Folli, A., Pochard, I., Nonat, A., Jakobsen, U. H., Shepherd, A. M. & Macphee, D. E. (2010). "Engineering Photocatalytic Cements: Understanding TiO_2 Surface Chemistry to Control and Modulate Photocatalytic Performances", *Journal of the American Ceramic Society*, 93, 3360-3369.

Fournier, L. C., Bamiduro, O., Mustafa, H., Mundle, R., Konda, R. B., Williams, F. & Pradhan, A. K. (2008), "Effects of substrate temperature on the optical and electrical properties of Al:ZnO films", *Semiconductor Science and Technology*, 23: 085019.

Frederichi, D., Scaliante, M. H. N. O., & Bergamasco, R. (2021). "Structured photocatalytic systems: photocatalytic coatings on low-cost structures for treatment of water contaminated with micropollutants—a short review", *Environmental Science and Pollution Research*, 28(19), 23610-23633.

Fuentes, G. G., Elizalde, E., Yubero, F., & Sanz, J. M. (2002). "Electron inelastic mean free paths have been estimated for Ti, TiC, TiN and TiO_2 for energies between 250 and 2000 eV", *Surface and Interface Analysis*, 33, 230–237.

Geim, A. K. & Novoselov, K.S. (2007). "The rise of graphene", *Nature Materials*, 6(3), 183-191.

Goncalves, L. M., Bermudez, V. D., Ribeiro, H. A., & Mendes, A. M. (2008). "Dye-sensitized solar cells: A safe bet for the future", *Energy & Environmental Science*, 1(6): 655-667.

Gould, M., & Lamont, C. (2010). "Examination of the optical band gap of various semiconducting materials", *Reed College, Portland*, OR 97202.

Grant, F. A. (1959). "Properties of Rutile (Titanium Dioxide)", *Reviews of Modern Physics*, 31: 646.

Gratzel, M. (2005). "Solar energy conversion by dye-sensitized photovoltaic cells", *Journal of Inorganic Chemistry*, 44(20), 6841-6851.

Gupta, V. & A. Mansingh, A. (1996). “Influence of post deposition annealing on the structural and Optical Properties of sputtered Zinc Oxide Film”, *Journal of Applied Physics,* 80 (2) 1063-1073.

Hagfeldt, A., Boschloo, G., Sun, L., Kloo, L. and Pettersson, H. (2010). “Dye-Sensitized Solar Cells”, *Chemical Reviews*, 110, 6595-6663.

Hall, (1879). "On a New Action of the Magnet on Electrical Current," *American Journal of Mathematics,* 2: 287-292.

Haque, S. A., Tachibana, Y., Willis, R. L., Moser, J. E., Gratzel, M., Klug, D. R. & Durrant, J. R. (2000). “Parameters influencing charge recombination kinetics in dye-sensitized nanocrystalline titanium dioxide films”, *Journal of Physical Chemistry B.* 104(3): 538-547.

Hardinger, S. (2008). “Organic Molecular Structures and Interactions”, *University of California,* 47: 223-226.

Hasan, M. A., & Sumathy, K. (2010). “Photovoltaic thermal module concepts and their performance analysis: A review”, *Renewable & Sustainable Energy Reviews*. 14(7): 1845-1859.

Hassanien, A. S. & Akl, A. A. (2018). “Optical characteristics of iron oxide thin films prepared by spray pyrolysis technique at different substrate temperatures”, *Applied Physics,* 124:752.

Hassaniena, A. S., Sharma, I., & Akl, A. A. (2020). “Physical and optical properties of a-Ge-Sb-Se-Te bulk and film samples: Refractive index and its association with electronic polarizability of thermally evaporated a-Ge15-xSbxSe50Te35 thin-films”, *Journal of Non-Crystalline Solids*, 531: 119853.

Hauch, A., & Georg, A. (2001). “Diffusion in the electrolyte and charge-transfer reaction at the platinum electrode in dye-sensitized solar cells”, *Electrochimica Acta, 46*(22), 3457–3466.

Hu, G.; & Tang, B. (2013). Photocatalytic mechanism of graphene/titanate nanotubes photocatalyst under visible- light irradiation", *Materials Chemistry and Physics*, 138, 608–614.

Illican, S., Caglar, Y., & Caglar, M. (2008). "Preparation and characterization of ZnO thin films deposited by sol-gel spin coating method. *Journal of Optoelectronics and Advanced Materials*. 10(10), 2578-2583.

Jiang, J., Oberdorster, G. & Biswas, P. (2009). "Characterization of size, surface charge, and agglomeration state of nanoparticle dispersions for toxicological studies", *Journal of Nanoparticle Research: An InterdisciplinaryForum for Nanoscale Science and Technology*, 77.

Jose, R., Thavasi, V., & Ramakrishna, S. (2009). "Metal oxides for dye-sensitized solar cells", *Journal of the American Ceramic Society*, 92(2), 289-301.

Kahn, A. (2016). Fermi level, work function and vacuum level", *Materials horizons*, 3, 7 – 10.

Katoh, R. (2012). "Quantitative evaluation of electron injection efficiency in dye-sensitized TiO_2 films", *Ambio*, 41(2), 143-148.

Krishnan, P., Zhang, M.-H., Yu, L. & Feng, H. (2013). " Photocatalytic degradation of particulate pollutants and self-cleaning performance of TiO_2-containing silicate coating and mortar", *Construction and Building Materials*, 44, 309-316.

Kuang, D. B., Ito, S., Wenger, B., Klein, C., Moser, J. E., Humphry-Baker, R., Zakeeruddin, S. M., & Gratzel, M., (2006). "High molar extinction coefficient heteroleptic ruthenium complexes for thin film dye-sensitized solar cells", *Journal of the American Chemical Society*, 128 (12): 4146-4154.

Kumar, B., Smita, K., Cumbal, L., Debut, A., Camacho, J., Hernández-Gallegos, E., Chávez-López, M. G., Grijalva, M., Angulo, Y., Rosero, G. Y. A. & Gustavo, R. (2015). "Pomosynthesis and biological activity of silver nanoparticles

using Passiflora tripartitafruit extracts [J]", *Advanced Materials Letters*, 6(2): 127−132.

Lackhoff, M., Prieto, X., Nestle, N., Dehn, F. & Niessner, R. (2003). "Photocatalytic activity of semiconductor-modified cement—influence of semiconductor type and cement ageing", *Applied Catalysis B, Environmental,* 43, 205-216.

Leary, R. & Westwood, A. (2011). "Carbonaceous nanomaterials for the enhancement of TiO_2 photo catalysis", *Carbon* 49(3), 741-772.

Lee, C., Wei, X. D., Kysar, J. W. & Hone, J. (2008). "Measurement of the elastic properties and intrinsic strength of monolayer graphene", *Science*. 321(5887): 385-388.

Lee, J. J., Coia, G. M. & Lewis, N. S. (2004). "Current Density versus Potential Characteristics of Dye-Sensitized Nanostructured Semiconductor Photoelectrodes. 2. Simulations", *Journal of Physics and Chemistry B*. 108 (17), 5282–5293.

Li, D., Muller, M. B., Gilje, S., Kaner, R. B. & Wallace, G. G. (2008)." Processable aqueous dispersions of graphene nanosheets", *Nature Nanotechnology*. 3(2): 101-105.

Li, Z-Y., Akhtar, M., Kong, B-S., & Yang, O-B. (2012). "Graphene application as a counter electrode material for dye-sensitized solar cell", *Materials Letters,* 86, 96-99.

Listorti, A., O'Regan, B. & Durrant, J.R. (2011). "Electron Transfer Dynamics in Dye-Sensitized Solar Cells". *Chemistry of Materials*, 23(15): 3381-3399.

Liu X., Jin Z. & Bu S. (2005). "Influences of Solvent on Properties of TiO_2 Porous Films Prepared by a Sol-Gel Method from the System Containing PEG", *Journal of Sol-Gel Science and Technology*, 36 (1), 103–111.

Liu, J., Gan, D., Hu, C., Kiene, M., & Paul S. H. (2002). "Porosity effect on the

dielectric constant and thermomechanical properties of organosilicate films", *Applied Physics Letters*, 81 (22), 4180.

Liu, S., Sun, H., Liu, S., & Wang, S. (2013). "Graphene facilitated visible light photodegradation of methylene blue over titanium dioxide photo catalysts", *Chemical Engineering Journal*, 214, 298–303.

Long, R., English, N.J., Prezhdo, O.V. (2012). "Photo-induced charge separation across the graphene-TiO_2 interface is faster than energy losses: A time-domain abinitio analysis", *Journal of the American Chemical Society*, 134, 14238–14248.

Loughin, S., French, R. H., DeNoye,r L. K., Ching, W-Y., & Xu Y-N. (1996). "Critical point analysis of the interband transition strength of electrons," *Journal of Physics D: Applied Physics*, 29: 1740 – 1750.

Maira, A. J., Coronado, J. M., Augugliaro, V., Yeung, K. L., Conesa, J. C., & Soria, J. J. (2001). "Fourier Transform Infrared Study of the Performance of Nanostructured TiO_2 Particles for the Photocatalytic Oxidation of Gaseous Toluene", *Journal of Catalysis*, 202: 413-420.

Makhlouf, M. M., El-Denglawey, A., Zeyada, H. M., & El-Nahass, M. M. (2014). The structural and optical characterizations of tetraphenylporphyrin thin films. *Journal of Luminescence*, **147**, 202-208.

Maluta, E., (2010). "Simulations of dye-sensitized solar cells". *A PhD Thesis. University of Bath*.

Mathews, N. R., Morales, E. R., Cortés-Jacome, M. A., & Antonio, J. T. (2009). TiO_2 thin films–Influence of annealing temperature on structural, optical and photocatalytic properties. Solar Energy, 83(**9**), 1499-1508.

Maragliano, C., Heskes, D., Stefancich, M., Chiesa, M. & Souier, T. (2013). "Dynamic electrostatic force microscopy technique for the study of electrical properties with improved spatial resolution", *Nanotechnology*, 24, 225703.

Maragliano, C., Lilliu, S., Dahlem, M. S., Chiesa, M., Souier, T., & Stefancich, M., (2014). “Quantifying charge carrier concentration in ZnO thin films by Scanning Kelvin Probe Microscopy”, *Science reports*, 4: 4203.

Marquez, E., Bernal-Oliva, A. M., Gonzalez-Leal, J. M., Pricto-Alcon, R., Ledesma, A., Jimenez-Garay, R. & Martil, I. (1999). “Optical-constant calculation of non-uniform thickness thin films of the $Ge_{10}As_{15}Se_{75}$ chalcogenide glassy alloy in the sub-band-gap region (0.1–1.8 eV)”, *Materials Chemistry and Physics*, 60: 231-239.

Marquez, E., Ramirez-Malo, J. B., Villares, P., Jimenez-Garay, R., & Swanepoel, R. (1995). “Optical characterization of wedge-shaped thin film of amorphous arsenic trisulphide based only on their shrunk transmission spectra,” *Thin Solid Films*, 254 (1–2), 83-91.

Miyashita, M., K. Sunahara, T. Nishikawa, Y. Uemura, N. Koumura, K. Hara, A. Mori, Abe, T. Suzuki, E., & Mori, S. (2008). “Interfacial Electron-Transfer Kinetics in Metal-Free Organic Dye-Sensitized Solar Cells: Combined Effects of Molecular Structure of Dyes and Electrolytes”, *Journal of the American Chemical Society*, 130(52): 17874- 17881.

Mugambi, N., Ngaruiya, J. M., Mugo, S. W., Riungu, G. G. & John, G. M. (2021) “Influence of Post Annealing Rates on Porosity, Dispersion Energy and Associated Dielectric Energy Losses of TiO_2 Thin Films”, *Journal of Photonic Materials and Technology*, 7(1): 1-7.

Muthee, D. K., & Dejene, B. F. (2021). Effect of annealing temperature on structural, optical, and photocatalytic properties of titanium dioxide nanoparticles. Heliyon, 7(6), e07269.

Nakade, S., Kanzaki, T., Kubo, W., Kitamura, T., Wada, Y. & Yanagida, S. (2005). “Role of electrolytes on charge recombination in dye-sensitized TiO_2 solar cell (1): The case of solar cells using the $I^-/I^{3(-)}$ redox couple”, Journal *of Physical Chemistry B*. 109(8): 3480-3487.

Ngei (2016). “Characterization and Performance Evaluation of Graphene Films as Counter Electrodes for Dye Sensitized Solar Cells”, *Unpublished Thesis*, JKUAT, Nairobi Kenya.

Nolan, N. T., Seery, M. K., & Pillai, S. C., (2009). “Spectroscopic Investigation of the Anatase-to-Rutile Transformation of Sol−Gel-Synthesized TiO_2 Photo catalysts”, *The Journal of Physical Chemistry C*, 113: 16151–16157.

Novoselov, K.S., Jiang, D., Schedin, F., Booth, T. J., Khotkevich, V.V., Morozov, S.V., & Geim, A.K. (2005). “Two-dimensional atomic crystals”, *Proceedings of the National Academy of Sciences of the United States of America*, 102(30): 10451-10453.

Nowotny, J., Sorrell, C. C., Bak, T., & Sheppard, L. R., (2005). “Defect disorder, transport and photoelectrochemical properties of TiO_2”, *Materials for Energy Conversion Devices, Woodhead Publishing in Materials, Cambridge*, 84 – 119.

Nuraje, N. Asmatulu, R. & Kudaibergenov, S. (2012) "Metal Oxide-based Functional Materials for Solar Energy Conversion: A Review," *Current Inorganic Chemistry*, (2) 124-146.

Ohyama M., Kozuka H. & Yoko T. (1997). “Sol-gel preparation of ZnO films with extremely preferred orientation along (002) plane from zinc acetate solution”, *Thin Solid Films*, 306:78 - 85.

O'Regan, B. C., Walley, K., Juozapavicius, M., Anderson, A., Matar, F., Ghaddar, T., Zakeeruddin, S. M., Klein, C., & Durrant, J. R. (2009). “Structure/Function Relationships in Dyes for Solar Energy Conversion: A Two-Atom Change in Dye Structure and the Mechanism for Its Effect on Cell Voltage”, *Journal of the American Chemical Society*, 131 (10): 3541-3548. 201.

O’Regan, B. & Gratzel, M. (1991). “A low-cost, high-efficiency solar cell based on dye- sensitized colloidal TiO_2 films”, *Nature*, 353(6346), 737-740.

Padinger, F., Brabec, C., Fromherz, T., Hummelen, J. & Sariciftci, N., (2000). "Fabrication of large area photovoltaic devices containing various blends of polymer and fullerene derivatives by using the doctor blade technique", *Opto-Electronics Review*, 8(4), 280– 283.

Pastrana – Martinez, L. M., Morales-Torres, S., Likodimos, V., José, L., Figueiredo, J. L., Faria, J. L., Falaras, P., Silva, A. M. T. (2012). "Advanced nanostructured photo catalysts based on reduced graphene oxide-TiO_2 composites for degradation of diphenhydramine pharmaceutical and methyl orange dye", *Applied Catalysis B.* 123, 241–256.

Peter, L.M., (2007). "Characterization and modeling of dye-sensitized solar cells", *Journal of Physical Chemistry C*, 111(18): 6601-6612.

Peter, R. G., & James A. H. (2007). "Fourier Transform Infrared Spectrometry, Second edition", *John WIley and Sons, Hoboken, New Jersey*.

Press Release in 2011 by U.S. Energy Information Administration: International energy outlook 2011.

Qin, Y. & Peng, Q. (2011). "Ruthenium sensitizers and their applications in dye-sensitized solar cells", *International Journal of Photoenergy*, 291579, 1-21.

Rabani, E., Reichman, D. R., Geissler, P. L., & Brus, L. E. (2003), "Drying-mediated self-assembly of nanoparticles", *Nature*, 426: 271–274.

Ramirez, A. M., Demeestere, K., De Belie, N., Mäntylä, T. & Levänen, E. (2010). "Titanium dioxide coated cementitious materials for air purifying purposes: Preparation, characterization and toluene removal potential", *Building and Environment*, 45, 832-838.

Ricci, P. C., Casu, A., Salis, M., Corpino, R. & Anedda, A. (2010). "Optically controlled phase variation of TiO2 nanoparticles", *The Journal of Physical Chemistry C*, 114, 14441–14445

Saito, M. & Fujihara, S. (2008). “Large photocurrent generation in dye-sensitized ZnO solar cells”, *Energy and Environmental Science*, 1(2): 280-283.

Saito, Y., Kambe, S., Kitamura, T., Wada, Y. & Yanagida, S. (2004). “Morphology control of mesoporous TiO_2 nanocrystalline films for performance of dye-sensitized solar cells”. *Solar Energy Materials and Solar Cells*, 83 (1), 1-13.

Sanchez-Vergara, M., Alvarez-Bada, J., Perez-Baeza, C., Loza-Neri, E., Torres-Garcia, R., Rodrigueq-Gomez, A., & Alonso-Huitron, J. (2014). “Morphological and optical properties of dimetallo-phthalocyaninie-complex thin films”. *Advances in Materials Physics and Chemistry*, 4, 20-28.

Sarkar S., Das N. S. & Chattopadhyay K. K. (2014). “Electro-active phase formation in PVDF–BiVO4 flexible nanocomposite films for high energy density storage application”, *RSC Advances*, 33, 58–66.

Sasahara, A. & Tomitori, M. (2013). “XPS and STM Study of Nb-Doped TiO_2 (110) -(1 × 1) Surfaces”, *Journal of Physical Chemistry C*, 117 (34): 17680–17686.

Shalini, S., Balasundaraprabhu, R., Satish Kumar, T., Prabavathy, N., Senthilarasu, S., & Prasanna, S. (2016). “Status and outlook of sensitizers/dyes used in dye sensitized solar cells (DSSC): A review”, *International Journal of Energy Research*, 40(10): 1303–1320.

Sharma, D.; Mehra, R.; & Raj, B. (2021). “Comparative analysis of photovoltaic technologies for high efficiency solar cell design”, *Superlattices Microstruct*, 153, 106861.

Sheppard, L. R., Bak, T. & Nowotny, J. (2006). “Electrical properties of niobium-doped titanium dioxide. 1. Defect disorder”, *The Journal of Physical chemistry B.* 110(45): 22447-22454.

Shinen, M. H., AlSaati, S. A. A., & Razooqi, F. Z. (2018). “Preparation of high transmittance TiO_2 thin films by sol-gel technique as antireflection coating”, *In Journal of Physics: Conference Series, IOP Publishing*, 1032, (1), 012018.

Simon, M. & Jun, Y. (2012). “Influence of Surface Adsorption on Work Function Measurements on Gold-Platinum Interface Using Scanning Kelvin Probe Microscopy”, *Conference Series*, 371: 012030.

Skrypnychuk, V., Boulanger, N., Nordenström, A., & Talyzin, A. (2020). “Aqueous Activated Graphene Dispersions for Deposition of High-Surface Area Supercapacitor Electrodes”, *The Journal of Physical Chemistry Letters*, 11(8), 3032 – 3038.

Smestad, G. P., Spiekermann, S., Kowalik, J., Grant, C. D., Schwartzberg, A. M., Zhang, J., Tolbert, L. M., & Moons, E. (2003). "A technique to compare polythiophene solid state dye-sensitized $Ti0_2$ solar cells to liquid junction devices", *Solar Energy Materials and Solar Cells*, 76(1), 85 -105. 249.

Smestad, G., Krebs, F., Lambert, C., Granqvist, C., Chopra, K., Matthew, X., and Takakura, H. (2008). “Solar cell efficiencies in solar energy materials and solar cells”, *Solar Energy Materials and Solar Cells*, 92(4), 371-373.

Snaith, H. J. & Schmidt-Mende, L., (2007). “Advances in liquid-electrolyte and solid-state dye- sensitized solar cells”, *Advanced Materials*, 19(20): 3187-3200.

Sodergren, S., Hagfeldt, A., Olsson, J. & Lindquist, S. E. (1994). “Theoretical Models for the Action Spectrum and the Current-Voltage Characteristics of Microporous Semiconductor Films in Photoelectrochemical Cells”, *Journal of Physical Chemistry*. 98 (21), 5552–5556.

Stoller, M. D., Park, S. J., Zhu, Y.W., An, J. H. & Ruoff, R.S. (2008). “ Graphene-Based Ultracapacitors”, *Nano Letters*, 8(10): 3498-3502.

Strayer, R.W., Mackie, W., & Swanson, L.W. (1973). “Work function measurements by the field emission retarding potential method”, *Surface Science*, 2: 225-248.

Sun, S. R., Gao, L. & Liu, Y.Q. (2010). “Enhanced dye-sensitized solar cell using graphene- TiO_2 photoanode prepared by heterogeneous coagulation”, *Applied*

Physics Letters. 96(8).

Tan, W., Koughia, K., Singh, J., & Kasap, S. (2006). "Fundamental Optical Properties of Materials I. In J. Singh (Ed.), Optical Properties of Condensed Matter and Applications", *John Wiley & Sons*, 1-25.

Tang, B. Chen, H., Peng, H., Wang, Z & Huang, W. (2018). "Graphene Modified TiO_2 composite photocatalysts: Mechanics, progress and Perspective", *Nanomaterials*, (1-27).

Tang, S. J., Chang, T. R., Huang, C. C., Lee, C. Y., Cheng, C. M., Tsuei, K., Jeng, H. T. & Mou, C. Y. (2010). "Dispersive resonance bands within the space-charge layer of a metal-semiconductor junction", *Physical review B*. 81(**24**) 245406

Tauc, J., Grigorovici, R., & Vancu, A. (1966). "Optical properties and electronic structure of amorphous germanium", *Physica Status Solidi*, 15, 627-637.

Tepantlan, C., Gonzalez, A., & Arreola, I. (2008). "Structural, optical and electrical properties of CdS thin films obtained by spray pyrolysis", *Revista Mexicana De-Fisica*, 54(2), 112-117.

Thavasi, V., Renugopalakrishnan, V., Jose, R., & Ramakrishna, S. (2009). "Controlled electron injection and transport at materials interfaces in dye sensitized solar cells", *Materials Science and Engineering R: Reports*, 63(3), 81–99.

Valluzzi, M. G., Valluzzi, L. G., Meyer,M., Hernández-Fenollosa, M. A., and Damonte, L. C. (2018). "Optical and Electrical Properties of TiO_2/Co/TiO_2MultilayerFilms Grown by DC Magnetron Sputtering", *Advances in Condensed Matter Physics*. 1155:1257543.

Van de Lagemaat, J., Benkstein, K.D. & Frank, A. J. (2001). "Relation between Particle Coordination Number and Porosity in Nanoparticle Films: Implications to Dye-Sensitized Solar Cells", *Journal of Physical Chemistry B*, 105 (50), 12433–12436.

Van der Pauw, L. J. (1958). "A Method of Measuring the Resistivity and Hall Coefficient on Lamellae of Arbitrary Shape", *Philips Technical Review*. 20: 220-224.

Voss, B., Knobloch, T., & Goetzberger, A. (1998). “Crystalline silicon solar cells”, *Chichester: John Wiley & Sons Ltd*.

Wagner, S. J., Joachim Meier, A. S., Helmy, J., Stewart, A., Marc S., & David C. H. (2007) "Polarization-dependent nonlinear refraction and two-photon absorption in GaAs/AlAs superlattice waveguides below the half-bandgap", *Journal of the Optical Society of America B*, 24, 1557-1563.

Wang, C., Cao, M., Wang, P., Ao, Y., Hou, J., Qian, J. (2014). “Preparation of graphene-TiO_2 composites with enhanced photocatalytic activity for the removal of dye and Cr (VI)”, *Applied Catalysis A: General*. 473: 83–89.

Wang, L., Fang, X.M., & Zhang, Z.G. (2010). “Design methods for large scale dye-sensitized solar modules and the progress of stability research”, *Renewable & Sustainable Energy Reviews*, 14(9): 3178-3184.

Wemple S. H. & DiDomenico M. (1969). “Oxygen-Octahedra Ferroelectrics. II. Electro-optical and Nonlinear-Optical Device Applications,” *Journal of Applied Physics*, 40: 735.

Wemple S. H. & DiDomenico M. (1971). “Behavior of the Electronic Dielectric Constant in Covalent and Ionic Materials”, *Physical Review B*, 3: 1338–51. 288.

Wohrle, D. & Meissner, D. (1991).” Organic solar cells”, *Advanced Materials*, 3(3): 129-138.

Xiang, Q., Yu, J. & Jaroniec, M. (2012). “Graphene-based semiconductor photocatalysts”, *Chemical Society Reviews*, 41(2), 782-796.

Xinmi H., Xiao X., Zhang, Z., Yang, J., & Zhang J. (2017). “Influence of surface

topography, crystallinity, and thermal conductivity on reflectance and color of metallic-effect high-density polyethylene parts filled with aluminum pigments," *Polymer Engineering & Science*. 58. 10.1002/pen.24593.

Yager, K., Tanchak, O., Godbout, C., Fritzsche, H., Barrett, C. (2006). "Photomechanical Effects in Azo-Polymers Studied by Neutron Reflectometry", *Macromolecules*, 39, 9311-9319.

Yakovkin, I. N. (2016). "Dirac Cones in Graphene, Interlayer Interaction in Layered Materials, and the Band Gap in MoS_2", *Crystals*, 6(11), 1 – 13.

Yakuphanoglu F., Cukurovali A. & Yilmaz I. B, (2004). "Single-Oscillator Model and Determination of Optical Constants of Some Optical Thin Film Materials", *Physica B Condensed Matter*, 353, 210–216.

Yang C., Fan H., Xi Y., Chen J. & Li Z. (2008). "Effects of depositing temperatures on structure and optical properties of TiO_2 film deposited by ion beam assisted electron beam evaporation", *Applied Surface Science*, 254: 2685-2689.

Yang, Y., Qiang, Y. H., Song, J., Xing, Z., & Song, C. B. (2015). "Enhanced charge-transfer performance of photoelectrode based on interface modification in dye-sensitized solar cells", *International Journal of Electrochemical Science*, *10*(7), 5479-5487.

Yasuteru S., Shingo K., Takayuki K., Yuji W., and Shozo Y., (2004). "Morphology control of mesoporous TiO_2 nanocrystalline films for performance of dye-sensitized solar cells, Solar Energy Materials and Solar Cells, 83(1), 1-13.

Yuan, Y., Ding, J., Xu, J., Deng, J. & Guo, J. (2010). "TiO_2 Nanoparticles Co-Doped with Silver and Nitrogen for Antibacterial Application", *Journal of Nanoscience and Nanotechnology*, 10: 4868–4874.

Zeng, D.W., Xie, C.S., Zhu, B.L., Song, W.L. & Wang, A.H. (2003). "Synthesis and characteristics of Sb-doped ZnO nanoparticles", *Materials Science and*

Engineering: B, 104(1), 68 - 72

Zeweck, U., Loppacher, C., Otto, T., Grafström, S., & Eng, L. (2005). "Accuracy and resolution limits of Kelvin probe force microscopy", *Physical Review*, 71:125424.

Zhang, Q.F. & Cao, G.Z. (2011). "Nanostructured photoelectrodes for dye-sensitized solar cells", *Nano Today*, 6(1): 91-109.

Zhang, L.W.; Fu, H.B.; & Zhu, Y.F. (2008). "Efficient TiO_2 photocatalysts from surface hybridization of TiO_2 particles with graphite-like carbon", *Advanced Functional Materials*, 18: 2180–2189.

Zhao, B., Zhou, J., Chen, Y., & Peng, Y. (2011). "Effect of annealing temperature on the structure and optical properties of sputtered TiO_2 films. *Journal of Alloys and Compounds*, 509(**9**), 4060-4064.

Zhiwen Q., Haibo G., Xiaopeng Y., Zichao Z., Jun H., Bingqiang C., Daisuke N. & Tatsuo O. (2015). "Phosphorus Concentration Dependent Microstructure and Optical Property of ZnO Nanowires Grown by High-Pressure Pulsed Laser Deposition", *The Journal of Physical Chemistry, C*, 119 (8), 4371-4378.

Zhu, C.Z., Guo, S.J., Wang, P., Xing, L., Fang, Y.X., Zhai, Y.M. & Dong, S.J. (2010). "One-pot, water-phase approach to high-quality graphene/TiO_2 composite nanosheets", *Chemical Communications*, 46(38): 7148-7150.

Zhu, F., Wu, D.P., Li, Q., Dong, H., Li, J.M., Jiang, K., & Xu, D.S. (2012). "Hierarchical TiO_2 microspheres: synthesis, structural control and their applications in dye-sensitized solar cells". *Rsc Advances*, 2(31): 11629-11637.

APPENDICES

Appendix I: A photograph of (a) Varian 7000e FT-IR and (b) Optical Image of Scanning Kelvin Probe Microscope (SKPM) and Inset Data on the Screen

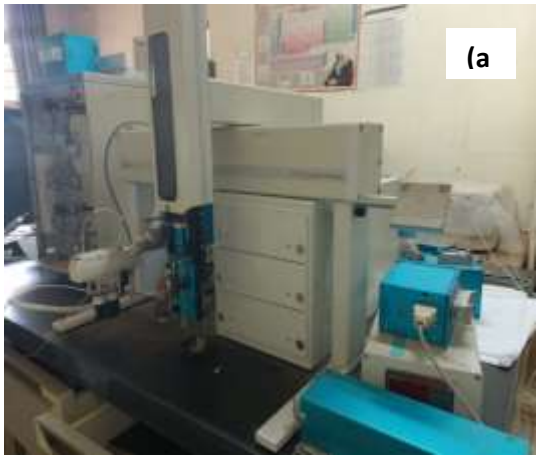

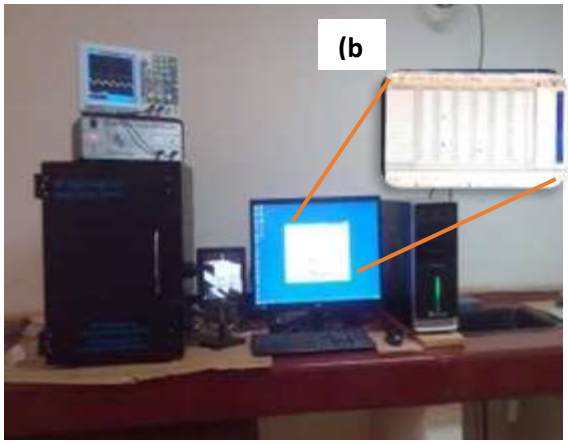

Appendix II: A Photograph of (a) Deposition of TiO_2 on FTO and Graphene on Glass Substrate and (b) Titanium Nanoxide, N719 Ruthenium Dye, Electrolyte and Platisol T/SP from Left to Right

Appendix III: A Photograph of Measurements of the Short Circuit, I_{SC} and Open Voltage, V_{OC} for the Assembled DSSC (Inset) in a Dark Room